ANALYSIS OF THE DYNAMIC STABILITY DERIVATIVES FOR HIGH ANGLE OF ATTACK AIRCRAFT

by

Joon Soo Ko

Dissertation submitted to the Faculty of the
Virginia Polytechnic Institute and State University
in partial fulfillment of the requirements for the degree of
DOCTOR OF PHILOSOPHY
in
Aerospace and Ocean Engineering

APPROVED:

Dr. F. H. Lutze, Chairman

Dr. E. M. Cliff

Dr. J. F. Marchman

Dr. M. Williams

Dr. W. L. Neu

April, 1985
Blacksburg, Virginia

ANALYSIS OF DYNAMIC STABILITY DERIVATIVES FOR AIRCRAFT AT HIGH ANGLES OF ATTACK

by

Joon Soo Ko

Committee Chairman: Dr. F. H. Lutze

Aerospace and Ocean Engineering

(ABSTRACT)

Modern, high performance aircraft are required to be able to fly and be controlled over a wide variety of flight conditions. In order to predict the aircraft behavior and control requirements over the entire flight regime it is necessary to have a proper aerodynamic model. Flight conditions at high angles of attack lead to separated flows making the aerodynamic model more difficult to obtain. In this research wind tunnel experiments are performed on an F-5 aircraft model at high angles of attack, with small oscillations about the body oriented roll axis. In addition the free stream environment can be configured in one of three ways: 1) straight uniform flow, 2) curved flow to simulated a horizontal turn, and 3) rolling flow to simulated a roll motion about the relative velocity vector.

A description of the wind tunnel velocity and the recently developed roll oscilatory rig is given. In addition new linearized equations of motion are developed for describing the small roll oscillation in the non-uniform flow environment. These equations are used to reduce the data obtained in the wind tunnel experiments in order to obtain the usual combined rotary and unsteady aerodynamic stability derivatives as well as new combinations of pure rotary derivatives obtainable only with the non-uniform flow conditions.

Lateral-directional force and moment stability derivative information is provided for ranges in angle of attack from 0 to 45 degrees. The effects of curvature, roll rate and sideslip angle on the various stability coefficients are displayed as well as the effects of the frequency and amplitude of roll oscillation. These same data are used to generated two aerodynamic models which are used in a linearized stability analysis throughout the range of angles of attack. Results of this analysis indicate that at high angles of attack the aerodynamic model which gives the best agreement with full-scale flight test results is an "unsteady" model which includes the pure rotary stability derivatives and unsteady aerodynamic stability derivatives individually.

Finally the sensitiveness of the stability characteristics of the aircraft with respect to changes in the basic lateral-directional stability parameters, as predicted by the linear analysis, is determined for the two aerodynamic models proposed. Considerable differences in the results are observed between the two models at the higher angles of attack.

ACKNOWLEDGEMENTS

The author wishes to thank Dr. F. H. Lutze who served as the Chairman of his Advisory Committee, for his valuable direction and encouragement in the development of the research and successful completion of study.

He is grateful to Dr. E. M. Cliff, Dr. J. F. Marchman , Dr. M. Williams and Dr. W. L. Neu for valuable technical and mathematical guidance on the thesis.

Special thanks are due to B. Z. Sung, S. H. Kwon, U . Shankar, G . Benton, F. Shelor, R. Frazier, G. Stafford, G. Bandy and K. Morris on their friendships.

DEDICATION

To my mother , father and other members of my family:

They supported me to obtain an excellent education with encouragement and inspiration.

TABLE OF CONTENTS

LIST OF TABLES

LIST OF FIGURES

NOMENCLATURE

Alphabetical

a_x, a_y, a_z	components of acceleration of vehicle mass center w.r.t. earth
b	wing span
C_{i_j}	$\partial(C_i)/\partial(j)$, stability derivatives, $C_i = C_x$, C_y, C_z, C_l, C_m, C_n (forces and moments coefficients in body axes system), j = α,β, $\hat{p}$, $\hat{q}$, $\hat{r}$, $\dot{\hat{\alpha}}$, $\dot{\hat{\beta}}$, $\dot{\hat{p}}$, $\dot{\hat{q}}$, $\dot{\hat{r}}$ (stability parameters)
$C_{i_{jk}}$	$\partial(C_i)/\partial(jk)$, mixed derivatives, $C_i = C_x$, C_y, C_z, C_l, C_m, C_n (forces and moments coefficients in body axes system), j & k = β, $\hat{p}$, $\hat{r}$
C_D	drag coefficient (drag/$q_\infty S$)
C_L	lift coefficient (lift/$q_\infty S$)
C_T	thrust coefficient (thrust-force/$q_\infty S$)
C_l	rolling moment coefficient (rolling-moment/$q_\infty Sb$)
C_m	pitching moment coefficient (pitching-moment/$q_\infty Sc$)
C_n	yawing moment coefficient (yawing-moment/$q_\infty Sb$)
C_x	axial force coefficient (axial-force/$q_\infty S$)

C_y	side force coefficient (side-force /$q_\infty S$)
C_z	normal force coefficient (normal-force/$q_\infty S$)
c	mean aerodynamic chord
diag.( )	diagonal matrix
d.o.f.	degree of freedom
E	strain-gage supply voltage
E_{in}	voltage in-phase with displacement
E_{out}	voltage out-of -phase with displacement
E_R	amplitude of resolver voltage
e	voltage proportional to rolling moment
f	frequency of oscillation
g	acceleration due to gravity
HP	Hewlett Packard
Hz.	Hertz (cycle/second)
h.p.	horse power
I_x, I_y, I_z	moments of inertia about the body axes x, y and z respectively
I_{xy}, I_{yz}, I_{zx}	products of inertia
in	inch
k_1, k_2	reduced frequency parameters $k_1 = \omega b/2V$, $k_2 = \omega c/2V$
k_x, k_y, k_z	balance calibration factors along x, y and z axis respectively

k_l, k_m, k_n	balance calibration factors around x, y and z axis respectively
L	rolling moment
M	pitching moment
m	mass of the vehicle or the model
N	yawing moment
n	number of period
P, Q, R	components of angular velocity w.r.t. atmosphere
p	rolling velocity w.r.t. earth
$\hat{p}$	pb/2V, non-dimensional form of rolling velocity
psf	lb/ft^2
q	pitching velocity w.r.t. earth
$\hat{q}$	qc/2V, non-dimnsional form of pitching vlocity
q_∞	free stream dynamic pressure
R	radius measured from tunnel centerline
R_o	local radius of curvature
r	yawing velocity w.r.t. earth
$\hat{r}$	rb/2V, non-dimnsional form of yawing velocity
r.p.m.	revolution per minute
S	wing area
T	period of oscillation
$[T]_{bh}$	horizontal to body axes transformation matrix

$[T]_{bs}$	stability to body axes transformation matrix
$[T]_{bw}$	wind to body axes transformation matrix
$[T]_{sb}$	body to stability axes transformation matrix
t	time
$t_{1/2}$	time to half amplitude
u, v, w	components of velocity along x, y and z axis respectively
V	velocity of vehicle mass center, or local velocity due to curved flow angularity
$\vec{V}$	velocity vector of vehicle mass center w.r.t. atmosphere
$\vec{V}^E$	velocity vector of vehicle mass center w.r.t. earth
V_x, V_y, V_z	components of velocity of vehicle mass center w.r.t. earth
V_x^h, V_y^h, V_z^h	components of velocity of vehicle mass center w.r.t. earth along x^h, y^h, z^h axis
V_∞	free stream velocity
V_T	transverse velocity due to roll rate and rolling flow angularity
$\vec{W}$	atmospheric velocity vector w.r.t. earth
W_x, W_y, W_z	components of atmospheric velocity w.r.t. earth along x, y and z axis

w_x^h, w_y^h, w_z^h	components of atmospheric velocity w.r.t. earth along x^h, y^h and z^h axis
X	axial force
$\vec{x}_1$, $\vec{x}_2$	vector form of state variables
x, y, z	body reference axes
x^h, y^h, z^h	horizontal reference axes
Y	side force
Z	normal force

Greek

α	angle of attack or angle
$\hat{\dot{\alpha}}$	$\dot{\alpha}c/2V$, non-dimensional form of angle of attack
α_r	reference angle of attack
β	angle of sideslip
$\hat{\dot{\beta}}$	$\dot{\beta}b/2V$, non-dimensional form of sideslip angle
β_r	reference sideslip angle
ε	thrust longitudinal offset angle
∂	partial derivative
δ_a	aileron deflection angle
δ_e	elevator deflection angle
δ_r	rudder deflection angle
θ	elevation or pitch angle
θ'	rotational angle about y-axis

λ	eigenvalue
ρ	atmospheric density
σ	thrust lateral offeset angle
ϕ	bank or roll angle
ϕ'	rotational angle about x-axis
ψ	azimuth or yaw angle
ψ_n	yaw angle at the nose
ψ'	rotational angle about z-axis
$\vec{\Omega}_V$	angular velocity vector of vehicle mass center w.r.t. atmosphere
$\vec{\Omega}_E$	angular velocity vector of vehicle mass center w.r.t. earth
$\vec{\Omega}_W$	atmospheric angular velocity vector w.r.t. earth
Ω_x, Ω_y, Ω_z	components of atmospheric angular velocity w.r.t. earth around x, y and z axis
Ω_x^h, Ω_y^h, Ω_z^h	components of atmospheric angular velocity w.r.t. earth around x^h , y^h and z^h axis
ω	angular velocity ($2\pi f$)

Subscript

A	aerodynamic quantities
a	tare condition
B	balance
in	in-phase quantities

max	maximum values
out	out-of-phase quantities
r	reference flight conditions
F	applied forces or torques
v	wind-off condition
w	wind-on condition

Superscript

$\bar{(\ )}$	absolute values
$\vec{(\ )}$	vector
$\hat{(\ )}$	non-dimensional quantities
$\dot{(\ )}$	differentiation w.r.t. time (velocity)
$\ddot{(\ )}$	second differentiation w.r.t. time (acceleration)
$(\ )^{b}$	body axes coordinate system
$(\ )^{h}$	horizontal axes coordinate system
$(\ )^{s}$	stability axes coordinate system
$(\ )^{o}$	degree

Bracket

[ ]	matrix
$[\ ]^{T}$	transpose of matrix
$[\ ]^{-1}$	inverse of matrix

Etc.

$\Delta(\ )$	small increments

Chapter I

INTRODUCTION

Modern high performance aircraft are required to be able to fly and be controlled over a wide variety of flight conditions. One regime of flight of particular interest is that which includes high angles of attack where it has been shown that a tactical advantage over the adversary could be obtained provided control of the aircraft could be maintained. In order to be able to predict the dynamic behavior as well as design a control system for an aircraft operating under these conditions, a properly documented and detailed knowledge of the aerodynamic characteristics of the vehicle at high angles of attack is required. In addition it would be useful to know how different maneuvers such as turning or rolling would affect various aerodynamic characteristics (Refs. 1-5).

Typically much of this information is obtained from various types of wind tunnel testing. Included in these tests are the so-called static tests where the model is positioned at different attitudes with respect to the uniform free stream vlocity and the forces and moments recorded. Consequently the changes in these force and moment components with angle of attack and sideslip angle can be determined.

The other type of wind tunnel test considered standard is that associated with oscillating the model about the aircraft roll, pitch, or yaw axis with the model at various attitudes with respect to the uniform free stream. This type of tests is called a dynamic tests and is intended to give additional information on force and moment variation with roll, pitch or yaw rate. Due to the oscillatory nature of this technique, unsteady aerodynamic phenomena also enter into the results (Refs. 6,7).

In recent years new and different techniques have been proposed to obtain additional information about the aerodynamic properties of aircraft operating in unusual flight conditions (spin) and at high angles of attack. Typical of these approaches is the rotary balance technique (Ref. 8). Here the unsteady aerodynamic effects are eliminated by rotating the model at constant rate in the uniform air stream. The mechanical mechanism required for this type of testing is very complex and setting up prescribed flight conditions, difficult.

Although many of these various facilities exist throughout the world, there are few facilities which can handle more than one type of testing. Consequently when results are compared between or among facilities, generally the condi-

tions of the tests, the model, and the test techniques are very different, reducing the credibility of any comparisons which might be made.

It is desirable therefore to be able to conduct the static and oscillatory tests with the same model in the same wind tunnel environment. In addition if pure rotating model capabilities were available additional insight into the unsteady aerodynamic effects could be obtained. The VPI&SU Stability Wind Tunnel (SWT) has these capabilities(Refs. 9 - 12). However instead of rolling or yawing the model, the SWT has the capability to curve or roll the flow while the model is fixed at some attitude. As a result, all possible attitudes can be examined in both a curved and rolling flow environment to obtain the steady state effects of roll rate or yaw rate on the forces and moments. These types of tests are carried out with no more difficulty than the unusual static wind tunnel tests.

As a part of the research presented here, a compact roll oscillatory rig was developed to use in the SWT. This recently added feature now permits the testing of a specific model in the static environment associated with the usual wind tunnel test, in the pure roll rate or yaw rate environment, and in an oscillatory environment which can be included in either of the first two test conditions. This combi-

nation of oscillatory motion in the presence of curved or rolling flow allow new and unique combinations of flow fields to be simulated in the wind tunnel (see Chapters II and III).

These capabilities have been applied to the wind tunnel testing of a model of an F-5 aircraft. The tests were carried out with and without small oscillations about the body oriented roll axis. In addition the free stream environment was configured in one of three ways: 1) straight uniform flow, 2) curved flow, simulating a horizontal turn, and 3) rolling flow, simulating a rolling motion about the relative velocity vector.

1.1 REVIEW OF DYNAMIC STABILITY PARAMETERS

In order to describe the motion of an aircraft, it is necessary to determine the force and moment equations which describe translational and angular motion of that aircraft. In general, analytical solutions for these non-linear equations can not be obtained. However, for a particular reference flight condition, linearized equations for the case of small disturbances in the neighborhood of that reference flight condition can be obtained which can be solved and analyzed for the purpose of describing vehicle motions.

Associated with these linearized equations of motions are linearized representations of the aerodynamic forces and moments. These reactions are usually represented by a Taylor series expansion to first order in the small disturbance variables. The derivatives of the aerodynamic forces and moments with respect to these variables, which appear in the Taylor series and are evaluated at the reference flight condition, are called stability derivatives. The variables, which are included in the aerodynamic representations are vehicle velocities, angular rates, control angles and possibly the time derivatives of these variables. As a consequence of the various types of variables which appear in the aerodynamic terms, the stability derivatives can be classified into two types. "Static Stability Derivative" refers to the derivative associated with the change in an aerodynamic reaction with respect to a change in a control or aerodynamic angle, and "Dynamic Stability Derivative" refers to the derivative associated with the change in an aerodynamic reaction with respect to a change in angular velocity or the time rate of change of the above angles.

In order to characterize the motions of an aircraft, it is necessary to determine the stability derivatives for the various reference flight conditions which might be encountered. As indicated previously, one method utilized to ob-

tain this information is wind tunnel testing. Typically, the static stability derivatives are determined by recording the forces and moments which act on a model immersed at various angles of attack and sideslip in a uniform wind tunnel flow. The techniques used to measure dynamic stability derivatives, on the other hand, are varied in nature. The objective is to move the flow or the model in such a way as to isolate the stability derivative of interest. Table 1 and 2 (Ref. 7) describe the dynamic stability derivatives and wind tunnel dynamic tests for obtaining these derivatives respectively.

Generally there are two approaches to obtaining the pure rotary dynamic derivatives. One approach is to rotate the model in a uniform stream, and the other approach is to shape the flow about the fixed model (Refs. 8-12). By mounting a model in different orientations and offset positions from the axes of rotation of a rotary balance, various rotary stability derivatives can be defined and obtained. One particular orientation provides the so-called coning motion and its associated derivatives (Refs. 8,13). However, Steidle (Ref. 14) has shown the relationship between these coning stability derivatives and pure rotary derivatives about the conventional body oriented axes.

The technique of holding the model stationary while shaping the flow about the model is not used very much. The VPI&SU SWT is one of the few facilities to have this capability. By using the curved flow test section one can obtained the pure yaw rate (r) and pitch rate (q) dynamic stability derivatives and by using the rolling flow test section, can obtain the pure roll rate (p) dynamic stability derivatives. It should be pointd out that these derivatives are with respect to stability axes (oriented with respect to the relative wind direction) and not the body oriented axes. However if a complete set of data is obtained, the transformation from one system to the other is possible.

Facilities to obtain pure rotary derivatives are rare. More often experimental facilities use the method of oscillating the model in a uniform stream to obtain the dynamic stability drivatives. In most cases an additional restriction is applied in that the oscillation is about some specified axis. As a result a combination of rotational motion with an unsteady aerodynamic motion is obtained (see Chapter II). The result is the determination of a combined aerodynamic stability derivative which includes the pure rotary derivative and an unsteady translational acceleration derivative. Without further information these two components cannot be separated. Finally it is of interest to mention

other techniques for obtaining these various stability data that either have been used or are still currently in use. These include translational oscillation techniques (Ref. 15) used to obtain pure translational acceleration derivatives (the so-called $\dot{\alpha}$, and $\dot{\beta}$ derivatives), the snaking motion or planar motion mechanism method (Refs. 16,17), used to obtain pure rotary stability derivatives (in an unsteady environment), and the model free techniques (Ref. 18) which are more useful for exploratory experiments rather than systematic stability testing.

1.2 FEATURES OF THIS RESEARCH

As indicated previously it is unusual to have a facility which can test a given model in the static, pure rotary, and oscillating environment. The development of a roll oscillatory rig which can be used in conjunction with both the curved and rolling flow test sections of the VPI&SU STW provides just such a facility. It is the purpose of this research to develop the oscillatory capability and to utilize it in the current wind tunnl configurations to obtain a full set of dynamic stability parameters for a specific aircraft model.

The research work can be divided into five parts; 1) Development of the roll oscillatory rig and data acquisition system, 2) Development of the kinematic and dynamic equations of motion necessary to reduce the data, 3) The actual wind tunnel testing, data acquisition and reduction, 4) Presentation of new data and comparison with existing data where possible, and 5) Comparison of the predicted dynamic characteristics of the vehicle based on new data and on old data with those obtained flight tests.

More specific information and its location in this work is summarized as follows.

(1) Derivation of constrained equations of motion for small harmonic motion in the presence of non-uniform flow and development of data acquisition program (Chapter II).

(2) Development of a roll oscillatory rig which can be operated in the curved and rolling flow wind tunnel test sections of the VPI&SU SWT (Chapter III).

(3) Evaluation and comparison of the determined stability information using the oscillatory facility in curved and rolling flow with existing information (Chapter V).

- Effect of curvature, roll rate, angle of attack and sideslip upon stability coefficients.

- Effect of frequency and amplitude of rolling oscillation on the dynamic derivatives.

- Comparisons of pure damping derivatives for the same aircraft model obtained by utilizing curved flow, rolling flow and current combined techniques.

(4) Application of the measured data to linearized equations of motion for the purpose of determining the stability characteristics and to estabilish how the predicted results change for two different aerodynamic models (Chapter V).

Chapter II

EQUATIONS OF MOTION AND REDUCTION FORMULATION

2.1 EQUATIONS OF MOTION FOR A VEHICLE WITH 6 D.O.F.

In order to make use of the stability characteristics which are obtained from various kinds of wind tunnel simulations, it is useful to reduce the general equations of motion of a free flight vehicle in the atmosphere to those which govern the constrained motion in the wind tunnel. This type of approach was used previously by the author in order to obtain the equations which govern various pure oscillatory motions in a conventional wind tunnel with uniform flow (Ref, 19). The following analysis generalizes these previous results to the case of oscillatory motion of a model subjected to a free stream velocity which is non-uniform due to a rolling or curved flow test section environment. The procedure here is similar to that in Reference 17. The general equations of motion are developed for the case of free flight in an atmosphere with a non-uniform velocity distribution and are reduced to the case of a model constrained to operate in a wind tunnel.

The aircraft is assumed to be rigid and of constant mass in flight over a flat earth. The equations of motion can be

written in a body fixed axis system with the origin located at the center of mass. Figure 1 illustrates the typical axis system and also shows the components of forces, moments, displacements and angular rates along or about the various axes. We can list the three assumptions:

(A1) Rigid aircraft

(A2) Constant mass aircraft

(A3) Flat earth

The velocity (angular velocity) of the vehicle mass center with respect to the earth, $\vec{V}^E$ ($\vec{\Omega}^E$), can be written as the sum of the velocity (angular velocity) of the vehicle mass center w.r.t. the atmosphere, $\vec{V}$ ($\vec{\Omega}_V$), and the atmospheric velocity (angular velocity) w.r.t. the earth, $\vec{W}$ ($\vec{\Omega}_W$).

$$\vec{V}^E = \vec{V} + \vec{W} \tag{1}$$

The scalar components, in body axis, of vectors in Equation (1) are

$$\begin{bmatrix} V_x \\ V_y \\ V_z \end{bmatrix}^b = \begin{bmatrix} u \\ v \\ w \end{bmatrix}^b + \begin{bmatrix} W_x \\ W_y \\ W_z \end{bmatrix}^b \tag{2}$$

Also,

$$\vec{\Omega}^E = \vec{\Omega}_V + \vec{\Omega}_W \tag{3}$$

The scalar components of the vectors in Equation (3) are

$$\begin{bmatrix} p \\ q \\ r \end{bmatrix}^b = \begin{bmatrix} P \\ Q \\ R \end{bmatrix}^b + \begin{bmatrix} \Omega_x \\ \Omega_y \\ \Omega_z \end{bmatrix}^b \tag{4}$$

By using a wind axis to body axis orthonormal transformation matrix, T_{bw} , the horizontal axis to body axis orthonormal transformation matrix, T_{bh} , and the matrix relating body axis rates to the Euler angle rates (see Fig. 2, Ref. 19), the above equations can be written in the following form:

$$u = V \cos\alpha\cos\beta \tag{5.1}$$

$$v = V \sin\beta \tag{5.2}$$

$$w = V \sin\alpha\cos\beta \tag{5.3}$$

$$W_x = W_x^h\cos\theta\cos\psi + W_y^h\cos\theta\sin\psi - W_z^h\sin\theta \tag{6.1}$$

$$W_y = W_x^h(\sin\phi\sin\theta\cos\psi - \cos\phi\sin\psi) + W_y^h(\sin\phi\sin\theta\sin\psi + \cos\phi\cos\psi) + W_z^h(\sin\phi\cos\theta) \tag{6.2}$$

$$W_z = W_x^h(\cos\phi\sin\theta\cos\psi + \sin\phi\sin\psi) + W_y^h(\cos\phi\sin\theta\sin\psi - \sin\phi\cos\psi) + W_z^h(\cos\phi\cos\theta) \tag{6.3}$$

$$V_x = V_x^h\cos\theta\cos\psi + V_y^h\cos\theta\sin\psi - V_z^h\sin\theta \tag{7.1}$$

$$V_y = V_x^h(\sin\phi\sin\theta\cos\psi - \cos\phi\sin\psi) + V_y^h(\sin\phi\sin\theta\sin\psi + \cos\phi\cos\psi) + V_z^h(\sin\phi\cos\theta) \quad (7.2)$$

$$V_z = V_x^h(\cos\phi\sin\theta\cos\psi + \sin\phi\sin\psi) + V_y^h(\cos\phi\sin\theta\sin\psi - \sin\phi\cos\psi) + V_z^h(\cos\phi\cos\theta) \quad (7.3)$$

$$\Omega_x = \Omega_x^h\cos\theta\cos\psi + \Omega_y^h\cos\theta\sin\psi - \Omega_z^h\sin\theta \quad (8.1)$$

$$\Omega_y = \Omega_x^h(\sin\phi\sin\theta\cos\psi - \cos\phi\sin\psi) + \Omega_y^h(\sin\phi\sin\theta\sin\psi + \cos\phi\cos\psi) + \Omega_z^h(\sin\phi\cos\theta) \quad (8.2)$$

$$\Omega_z = \Omega_x^h(\cos\phi\sin\theta\cos\psi + \sin\phi\sin\psi) + \Omega_y^h(\cos\phi\sin\theta\sin\psi - \sin\phi\cos\psi) + \Omega_z^h(\cos\phi\cos\theta) \quad (8.3)$$

$$p = \dot{\phi} - \dot{\psi}\sin\theta \quad (9.1)$$

$$q = \dot{\theta}\cos\phi + \dot{\psi}\sin\phi\cos\theta \quad (9.2)$$

$$r = -\dot{\theta}\sin\phi + \dot{\psi}\cos\phi\cos\theta \quad (9.3)$$

The following set of six equations of motion in the body axes system are derived from the well known Newton's laws for translation and rotation along and around each axis of the body fixed system (Refs. 20,21).

$$\Sigma X - mg\sin\theta = m(a_x + q\,V_z - r\,V_y) \quad (10.1)$$

$$\Sigma Y + mg\ \cos\theta\sin\phi = m(a_y + r\ V_x - p\ V_z) \tag{10.2}$$

$$\Sigma Z + mg\ \cos\theta\cos\phi = m(a_z + p\ V_y - q\ V_x) \tag{10.3}$$

$$\Sigma L = I_x p - I_{yz}(q^2-r^2) - I_{zx}(\dot{r} + pq) - I_{xy}(\dot{q} - rp) - (I_y-I_z)qr \tag{10.4}$$

$$\Sigma M = I_y q - I_{zx}(r^2-p^2) - I_{xy}(\dot{p} + qr) - I_{yz}(\dot{r} - pq) - (I_z-I_x)rp \tag{10.5}$$

$$\Sigma N = I_z r - I_{xy}(p^2-q^2) - I_{yz}(\dot{q} + rp) - I_{zx}(\dot{p} - qr) - (I_x-I_y)pq \tag{10.6}$$

Although, Equations (1) through (10) are sufficient to specify the motions of an aircraft in space, it is impossible to obtain general analytic solutions from these non-linear differential equations. By assuming that the aircraft motion is one of small motions in the neighborhood of some reference flight condition, the above set of equations can be simplified. Reference flight conditions are those where the quantities u, v, w, p, q, r, ϕ, θ, ψ are constants (Ref. 22).

We now assume the following sets of assumptions to obtain fully linearized equations of motion of a vehicle in a non-uniform flow environment.

(A4) Symmetry in x-z plane ($I_{xy} = I_{yz} = 0$)

(A5) Zero angular velocities in reference flight state ($p_r = q_r = r_r = 0$ and $\Omega_{x_r}^h = \Omega_{y_r}^h = \Omega_{z_r}^h = 0$)

(A6) Small perturbed motion

($u = u_r + \Delta u$, $\phi = \phi_r + \Delta\phi$ and etc.)

where, Δu, $\Delta\phi$ and etc. are small and subscript r means the value at the reference flight condition.

Equations (1) through (7) can be written in the perturbed form by substituting the above variables, neglecting higher order terms, and subtracting out the reference flight conditions.

The resulting perturbed equations of motion are

$$\Delta X - mg \cos\theta_r \Delta\theta = m(\Delta a_x + \Delta q\, V_{z_r} + \Delta r\, V_{y_r}) \tag{11.1}$$

$$\Delta Y + mg(\Delta\phi \cos\phi_r \cos\theta_r - \Delta\theta \sin\phi_r \sin\theta_r) = m(\Delta a_y + \Delta r\, V_{x_r} - \Delta p\, V_{z_r}) \tag{11.2}$$

$$\Delta Z - mg(\Delta\phi \sin\phi_r \cos\theta_r + \Delta\theta \cos\phi_r \sin\theta_r) = m(\Delta a_z + \Delta p\, V_{y_r} - \Delta q\, V_{x_r}) \tag{11.3}$$

$$\Delta L = I_x \dot{\Delta p} - I_{zx} \dot{\Delta r} \tag{11.4}$$

$$\Delta M = I_y \dot{\Delta q} \tag{11.5}$$

$$\Delta N = I_z \dot{\Delta r} - I_{zx} \dot{\Delta p} \qquad (11.6)$$

Here, the L.H.S. of Equation (11) consist of aerodynamic,propulsive, gravitational and possibly support reactions on the aircraft.

By making the additional assumption that :

(A7) The propulsive and possible support reactions are linear functions of first order perturbation variables and possibly their derivatives and aerodynamic reactions are linear functions only of vehicle motion variables.

we have,

$$\Delta F = \Delta F \left(\Delta u, \Delta v, \Delta w, \Delta P, \Delta Q, \Delta R, \Delta\delta_a, \Delta\delta_e, \Delta\delta_r, \dot{\Delta u}, \dot{\Delta v}, \dot{\Delta w}, \dot{\Delta P}, \dot{\Delta Q}, \dot{\Delta R} \right) \qquad (12)$$

The perturbed equations of motion (Eq. 11) with the perturbed kinematic equations become fully linear.

The linearized equations describe the force motion relationship for a vehicle moving through an atmosphere which is itself moving with respect to the ground. Alternatively, the same equations describe the force and moment relations for an aircraft or aircraft model mounted in a wind tunnel and

held fixed or forced to move in some prescribed manner in the presence of either a uniform free stream or a non-uniform disturbed flow condition. Consequently, these equations will be discussed in the following sections for special wind tunnel tests used to obtain various static and dynamic derivatives.

2.2 CONSTRAINED EQUATIONS OF MOTION OF A WIND TUNNEL MODEL

In the wind tunnel test where the vehicle model is set up at nominal aerodynamic angles α_r and β_r , we can develop the relations between vehicle velocities in the reference flight condition and the tunnel free stream velocity by using Assumption (A8) and Equation (1)

(A8) The horizontal axes system is set up so that the x^h axis points upstream in the wind tunnel and the tunnel free stream velocity is V_∞ ($\Delta V_\infty = 0$).

Applying (A8) to Equation (1), we get following facts :

$$\vec{V}_r^E = \vec{V}_r + \vec{W}_r = 0 \qquad (13.1)$$

or,

$$\vec{V}_r = -\vec{W}_r = \vec{V}_\infty \qquad (13.2)$$

or,

$$W_{x_r}^{h} = - V_\infty \quad , \quad W_{y_r}^{h} = W_{z_r}^{h} = 0 \tag{13.3}$$

Assuming a non-roll reference condition such that :

(A9) $\phi_r = 0$

and applying (A8), (A9) and Equations (5), (6), and (13) to Equation (2), we have

$$\vec{V}^{E} = \begin{bmatrix} V_{x_r} \\ V_{y_r} \\ V_{z_r} \end{bmatrix} = \begin{bmatrix} u_r + W_{x_r} \\ v_r + W_{y_r} \\ w_r + W_{z_r} \end{bmatrix} = V_\infty \begin{bmatrix} \cos\alpha_r \cos\beta_r - \cos\theta_r \cos\psi_r \\ \sin\beta_r + \sin\psi_r \\ \sin\alpha_r \cos\beta_r - \sin\theta_r \cos\psi_r \end{bmatrix} = 0 \tag{14.1}$$

or,

$$\theta_r = \alpha_r \quad , \quad \psi_r = - \beta_r \tag{14.2}$$

Now consider a model which performs oscillatory motions around and/or along an axis (body axis or horizontal axis) and assume angular and linear displacements are very small. Here, the small rotational angles around each body axis and horizontal axis, of the model are designated respectively by $\Delta\phi'$, $\Delta\theta'$, $\Delta\psi'$ and $\Delta\phi^h$, $\Delta\theta^h$, $\Delta\psi^h$, which generally differ from the perturbed Euler angles, $\Delta\phi$, $\Delta\theta$ and $\Delta\psi$. We can list the assumption:

(A10) $\Delta\phi, \Delta\theta, \Delta\psi \ll 1$

$\Delta\phi', \Delta\theta', \Delta\psi' \ll 1$

$$\Delta\phi^h,\ \Delta\theta^h,\ \Delta\psi^h \quad << 1$$

$$\Delta V_x,\ \Delta V_y,\ \Delta V_z \quad << 1$$

$$\Delta V_x^h,\ \Delta V_y^h,\ \Delta_z^h \quad << 1$$

By using (A8), i.e. , wind axes and horizontal axes system coincide in the wind tunnel, the relative velocity of the vehicle mass center, V, in Equation (1) can be written in the following form.

$$V = (V_x \cos\alpha\cos\beta + V_y \sin\beta + V_z \sin\alpha\cos\beta - W_x^h) \qquad (15)$$

Substituting Equation (15) into (5) and using Assumptions {(A5), (A6), (A9), (A10)} and facts {Eqns. (13) and (14)}, we get the following perturbed equations.

$$\Delta u = \Delta V_x \cos^2\alpha_r\cos^2\beta_r + \Delta V_y \cos\alpha_r\cos\beta_r\sin\beta_r \qquad (16.1)$$
$$+ \Delta V_z \cos\alpha_r\sin\alpha_r\cos^2\beta_r - V_\infty(\Delta\alpha \sin\alpha_r\cos\beta_r + \Delta\beta \cos\alpha_r\sin\beta_r)$$

$$\Delta v = \Delta V_x \cos\alpha_r\cos\beta_r\sin\beta_r + \Delta V_y \sin^2\beta_r \qquad (16.2)$$
$$+ \Delta V_z \sin\alpha_r\cos\beta_r\sin\beta_r + V_\infty\Delta\beta \cos\beta_r$$

$$\Delta w = \Delta V_x \cos\alpha_r\sin\alpha_r\cos^2\alpha_r + \Delta V_y \sin\alpha_r\cos\beta_r\sin\beta_r \qquad (16.3)$$
$$+ \Delta V_z \sin^2\alpha_r\cos^2\beta_r + V_\infty(\Delta\alpha \cos\alpha_r\cos\beta_r - \Delta\beta \sin\alpha_r\sin\beta_r)$$

In a similar manner Equations (6) to (9) can be written

$$\Delta W_x = V_\infty(\Delta\theta \sin\alpha_r\cos\beta_r - \Delta\psi \cos\alpha_r\sin\beta_r) \quad (17.1)$$

$$\Delta W_y = - V_\infty(\Delta\phi \sin\alpha_r\cos\beta_r - \Delta\psi \cos\beta_r) \quad (17.2)$$

$$\Delta W_z = - V_\infty(\Delta\phi \sin\beta_r + \Delta\theta \cos\alpha_r\cos\beta_r + \Delta\psi \sin\alpha_r\sin\beta_r) \quad (17.3)$$

$$\Delta V_x = \Delta u + \Delta W_x = \Delta V_x^h \cos\alpha_r\cos\beta_r + \Delta V_y^h \cos\alpha_r\sin\beta_r - \Delta V_z^h \sin\alpha_r \quad (18.1)$$

$$\Delta V_y = \Delta v + \Delta W_y = \Delta V_x^h \sin\beta_r + \Delta V_y^h \cos\beta_r \quad (18.2)$$

$$\Delta V_z = \Delta w + \Delta W_z = \Delta V_x^h \sin\alpha_r\cos\beta_r - \Delta V_y^h \sin\alpha_r\sin\beta_r + \Delta V_z^h \cos\alpha_r \quad (18.3)$$

$$\Delta\Omega_x = \Delta\Omega_x^h \cos\alpha_r\cos\beta_r + \Delta\Omega_y^h \cos\alpha_r\sin\beta_r - \Delta\Omega_z^h \sin\alpha_r \quad (19.1)$$

$$\Delta\Omega_y = \Delta\Omega_x^h \sin\beta_r + \Delta\Omega_y^h \cos\beta_r \quad (19.2)$$

$$\Delta\Omega_x = \Delta\Omega_x^h \sin\alpha_r\cos\beta_r - \Delta\Omega_y^h \sin\alpha_r\sin\beta_r - \Delta\Omega_z^h \cos\alpha_r \quad (19.3)$$

$$\Delta p = \Delta P + \Delta\Omega_x = \Delta\dot{\phi} - \Delta\dot{\psi} \sin\alpha_r = \Delta\dot{\phi}' \quad (20.1)$$
$$= \Delta\dot{\phi}^h \cos\alpha_r\cos\beta_r + \Delta\dot{\theta}^h \cos\alpha_r\sin\beta_r - \Delta\dot{\psi}^h \sin\alpha_r$$

$$\Delta q = \Delta Q + \Delta\Omega_y = \Delta\dot{\theta} = \Delta\dot{\theta}' = \Delta\dot{\phi}^h \sin\beta_r + \Delta\dot{\theta}^h \cos\beta_r \quad (20.2)$$

$$\Delta r = \Delta R + \Delta\Omega_z = \Delta\dot{\psi} \cos\alpha_r = \Delta\dot{\psi}' \quad (20.3)$$
$$= \Delta\dot{\phi}^h \sin\alpha_r\cos\beta_r - \Delta\dot{\theta}^h \sin\alpha_r\sin\beta_r + \Delta\dot{\psi}^h \cos\alpha_r$$

Applying Equation (17) to Equation (18), we have following perturbed velocity components due to angular rotation and/or linear motion about the body axes system.

$$\Delta u = \Delta V_x - \Delta W_x = \Delta V_x - V_\infty(\Delta\theta \sin\alpha_r\cos\beta_r - \Delta\psi \cos\alpha_r\sin\beta_r) \quad (21.1)$$

$$\Delta v = \Delta V_y - \Delta W_y = \Delta V_y + V_\infty(\Delta\phi \sin\alpha_r\cos\beta_r - \Delta\psi \cos\beta_r) \quad (21.2)$$

$$\Delta w = \Delta V_z - \Delta W_z = \Delta V_z - V_\infty(\Delta\phi \sin\beta_r - \Delta\theta \cos\alpha_r\cos\beta_r - \Delta\psi \sin\alpha_r\sin\beta_r) \quad (21.3)$$

Comparing Equations (16) and (21), we have the combined results of perturbed aerodynamic angles due to small prescribed motions about and along the body axes system of the wind tunnel model.

$$\Delta\alpha = \Delta\theta - \Delta\phi \cos\alpha_r\tan\beta_r + (1/V_\infty)\{-\Delta V_x (\sin\alpha_r/\cos\beta_r) + \Delta V_z (\cos\alpha_r/\cos\beta_r)\} \quad (22)$$

$$\Delta\beta = \Delta\phi \sin\alpha_r - \Delta\psi - (1/V_\infty)\{\Delta V_x \cos\alpha_r\sin\beta_r - \Delta V_y \cos\beta_r + \Delta V_z \sin\alpha_r\sin\beta_r\} \quad (23)$$

The different set of those aerodynamic angles for each desired motion can be found in Reference 17.

By using Assumptions {(A8) - (A10)} and the facts {(Eqns. (13) and (14)} the perturbed equations of motion of a wind tunnel model which performs angular oscillation and /or translational oscillation about body axes can be derived from Equation (11) such that

$$\Delta X = mg \cos\alpha_r \, \Delta\theta + m \, \Delta a_x \tag{24.1}$$

$$\Delta Y = - mg \cos\alpha_r \, \Delta\phi + m \, \Delta a_y \tag{24.2}$$

$$\Delta Z = mg \sin\alpha_r \, \Delta\theta + m \, \Delta a_z \tag{24.3}$$

$$\Delta L = I_x \, \Delta\dot{p} - I_{zx} \, \Delta\dot{r} \tag{24.4}$$

$$\Delta M = I_y \, \Delta\dot{q} \tag{24.5}$$

$$\Delta N = I_z \, \Delta\dot{r} - I_{zx} \, \Delta\dot{p} \tag{24.6}$$

Other possible equations of motion for a wind tunnel model can also be derived from Equation (24) by using Equations (18), (19) and (20), and two special cases will be discussed in the following sections. Other cases can be found in Reference 17.

Now, for a wind tunnel model whose control surfaces are locked and there is no propulsive force, we have the additional assumptions.

(A11) Control-locked model

(A12) No propulsive reaction on the model

Usually, the L.H.S. of Equation (24) consists of aerodynamic reactions (ΔF_A), support reaction (ΔF_S) and the applied force or torque terms (ΔF_F). Further, since a model and the balance oscillate together by employing a mechanical/hydraulic drive system as in the VPI&SU roll oscillating rig, the support reaction and applied force or torque terms are those recorded by the strain-gage balance readings. The balance forces are due to the relative motion of the model w.r.t. the balance which is assumed to be small and negligible. Consequently, the L.H.S. of Equation (24) can be written as follows.

$$\Delta F = \Delta F_A - \Delta F_B \tag{25}$$

The aerodynamic reaction terms, i.e, Equation (12) can be simplified with the help of Assumptions (A11) and (A12).

$$\Delta F_A = \Delta F_\alpha \Delta\alpha + \Delta F_\beta \Delta\beta + \Delta F_{\dot\alpha} \Delta\dot\alpha + \Delta F_{\dot\beta} \Delta\dot\beta + \Delta F_P \Delta P + \Delta F_Q \Delta Q + \Delta F_R \Delta R + \Delta F_{\dot P} \Delta\dot P + \Delta F_{\dot Q} \Delta\dot Q + \Delta F_{\dot R} \Delta\dot R \tag{26}$$

Now, it is possible to describe the entire motion of the wind tunnel model which performs small prescribed oscillations along or about the body (or horizontal) axes of the

model from the restrained perturbation equations derived in this section . The data reduction procedures with these restrained equations of roll oscillation with either upstream curved or rolling flow are described in the following subsections.

2.2.1 Forced Oscillation in Roll with Local Curved Flow

For the wind tunnel model which performs small prescribed oscillation around the x-body axis of the model center of mass with locally curved upstream flow, Equations (18), (19), (20), (22) and (23) can be written as

$$\Delta V_x = \Delta V_y = \Delta V_z = 0 \tag{27.1}$$

$$\Delta P = \dot{\Delta\phi} + \Delta\Omega_z^h \sin\alpha_r,\ \Delta Q = 0,\ \Delta R = -\Delta\Omega_z^h \cos\alpha_r \tag{27.2}$$

$$\Delta\alpha = -\Delta\phi \cos\alpha_r \tan\beta_r,\ \Delta\beta = \Delta\phi \sin\alpha_r = \Delta\phi' \sin\alpha_r \tag{27.3}$$

For small reference sideslip angles, $\Delta\alpha = O(\Delta\phi\ \beta_r)$, and can be neglected. Applying Equation (27) to Equation (26), we get

$$\Delta F_A = \Delta F_\beta(\Delta\phi \sin\alpha_r) + \Delta F_{\dot\beta}(\dot{\Delta\phi} \sin\alpha_r) + \Delta F_P(\dot{\Delta\phi} + \Delta\Omega_z^h \sin\alpha_r) \tag{28}$$
$$- \Delta F_R(\Delta\Omega_z^h \cos\alpha_r) + \Delta F_{\dot P}(\ddot{\Delta\phi})$$

Applying Equations (25), (27) and (28) to Equation (24) the equations of motion of small prescribed motion about x-body axis with the upstream curved flow can be written as follows.

$$\Delta X_{\dot{P}}\ddot{\Delta\phi} + (\Delta X_P + \Delta X_{\dot{\beta}}\sin\alpha_r)\dot{\Delta\phi} + (\Delta X_\beta \sin\alpha_r)\Delta\phi + \Delta X_P(\Delta\Omega_z^h \sin\alpha_r) - \Delta X_R(\Delta\Omega_z^h \cos\alpha_r) - \Delta X_B = 0 \quad (29.1)$$

$$\Delta Y_{\dot{P}}\ddot{\Delta\phi} + (\Delta Y_P + \Delta Y_{\dot{\beta}}\sin\alpha_r)\dot{\Delta\phi} + (\Delta Y_\beta \sin\alpha_r + mg\cos\alpha_r)\Delta\phi + \Delta Y_P(\Delta\Omega_z^h \sin\alpha_r) - \Delta Y_R(\Delta\Omega_z^h \cos\alpha_r) - \Delta Y_B = 0 \quad (29.2)$$

$$\Delta Z_{\dot{P}}\ddot{\Delta\phi} + (\Delta Z_P + \Delta Z_{\dot{\beta}}\sin\alpha_r)\dot{\Delta\phi} + (\Delta Z_\beta \sin\alpha_r)\Delta\phi + \Delta Z_P(\Delta\Omega_z^h \sin\alpha_r) - \Delta Z_R(\Delta\Omega_z^h \cos\alpha_r) - \Delta Z_B = 0 \quad (29.3)$$

$$(-I_x + \Delta L_{\dot{P}})\ddot{\Delta\phi} + (\Delta L_P + \Delta L_{\dot{\beta}}\sin\alpha_r)\dot{\Delta\phi} + (\Delta L_\beta \sin\alpha_r)\Delta\phi + \Delta L_P(\Delta\Omega_z^h \sin\alpha_r) - \Delta L_R(\Delta\Omega_z^h \cos\alpha_r) - \Delta L_B = 0 \quad (29.4)$$

$$\Delta M_{\dot{P}}\ddot{\Delta\phi} + (\Delta M_P + \Delta M_{\dot{\beta}}\sin\alpha_r)\dot{\Delta\phi} + (\Delta M_\beta \sin\alpha_r)\Delta\phi + \Delta M_P(\Delta\Omega_z^h \sin\alpha_r) - \Delta M_R(\Delta\Omega_z^h \cos\alpha_r) - \Delta M_B = 0 \quad (29.5)$$

$$(I_{zx} + \Delta N_{\dot{P}})\ddot{\Delta\phi} + (\Delta N_P + \Delta N_{\dot{\beta}}\sin\alpha_r)\dot{\Delta\phi} + (\Delta N_\beta \sin\alpha_r)\Delta\phi + \Delta N_P(\Delta\Omega_z^h \sin\alpha_r) - \Delta N_R(\Delta\Omega_z^h \cos\alpha_r) - \Delta N_B = 0 \quad (29.6)$$

2.2.2 Forced Oscillation in Roll with Local Rolling Flow

For the wind tunnel model which performs small prescribed oscillation around the x-body axis of the model center of mass with locally rolling upstream flow, Equations (18), (19), (20), (22) and (23) can be written as

$$\Delta V_x = \Delta V_y = \Delta V_z = 0 \tag{30.1}$$

$$\Delta P = \dot{\Delta\phi} - \Delta\Omega_x^h \cos\alpha_r \cos\beta_r, \quad \Delta Q = -\Delta\Omega_x^h \sin\beta_r$$
$$\Delta R = -\Delta\Omega_x^h \sin\alpha_r \cos\beta_r \tag{30.2}$$

$$\Delta\alpha = -\Delta\phi \cos\alpha_r \tan\beta_r, \quad \Delta\beta = \Delta\phi \sin\alpha_r = \Delta\phi' \sin\alpha_r \tag{30.3}$$

For small reference sideslip angles, $\Delta Q = O(\Delta\Omega_x^h \beta_r)$ and $\Delta\alpha = O(\Delta\phi \beta_r)$. Applying Equation (30) to Equation (26), we get

$$\Delta F_A = \Delta F_\beta(\Delta\phi \sin\alpha_r) + \Delta F_{\dot\beta}(\dot{\Delta\phi} \sin\alpha_r) + \Delta F_P(\dot{\Delta\phi} - \Delta\Omega_x^h \cos\alpha_r) \tag{31}$$
$$- \Delta F_R(\Delta\Omega_x^h \sin\alpha_r) + \Delta F_{\dot P}(\ddot{\Delta\phi})$$

Applying Equations (25), (30) and (31) to Equation (24) the equations of motion of small prescribed motion about x-body axis with the upstream curved flow can be written as follows.

$$\Delta X_{\dot{p}}\ddot{\Delta\phi} + (\Delta X_p + \Delta X_{\dot{\beta}}\sin\alpha_r)\dot{\Delta\phi} + (\Delta X_\beta \sin\alpha_r)\Delta\phi \qquad (32.1)$$
$$- \Delta X_p(\Delta\Omega_x^h \cos\alpha_r) - \Delta X_R(\Delta\Omega_x^h \sin\alpha_r) - \Delta X_B = 0$$

$$\Delta Y_{\dot{p}}\ddot{\Delta\phi} + (\Delta Y_p + \Delta Y_{\dot{\beta}}\sin\alpha_r)\dot{\Delta\phi} + (\Delta Y_\beta \sin\alpha_r + mg\cos\alpha_r)\Delta\phi \qquad (32.2)$$
$$- \Delta Y_p(\Delta\Omega_x^h \cos\alpha_r) - \Delta Y_R(\Delta\Omega_x^h \sin\alpha_r) - \Delta Y_B = 0$$

$$\Delta Z_{\dot{p}}\ddot{\Delta\phi} + (\Delta Z_p + \Delta Z_{\dot{\beta}}\sin\alpha_r)\dot{\Delta\phi} + (\Delta Z_\beta \sin\alpha_r)\Delta\phi \qquad (32.3)$$
$$- \Delta Z_p(\Delta\Omega_x^h \cos\alpha_r) - \Delta Z_R(\Delta\Omega_x^h \sin\alpha_r) - \Delta Z_B = 0$$

$$(-I_x + \Delta L_{\dot{p}})\ddot{\Delta\phi} + (\Delta L_p + \Delta L_{\dot{\beta}}\sin\alpha_r)\dot{\Delta\phi} + (\Delta L_\beta \sin\alpha_r)\Delta\phi \qquad (32.4)$$
$$- \Delta L_p(\Delta\Omega_x^h \cos\alpha_r) - \Delta L_R(\Delta\Omega_x^h \sin\alpha_r) - \Delta L_B = 0$$

$$\Delta M_{\dot{p}}\ddot{\Delta\phi} + (\Delta M_p + \Delta M_{\dot{\beta}}\sin\alpha_r)\dot{\Delta\phi} + (\Delta M_\beta \sin\alpha_r)\Delta\phi \qquad (32.5)$$
$$- \Delta M_p(\Delta\Omega_x^h \cos\alpha_r) - \Delta M_R(\Delta\Omega_x^h \sin\alpha_r) - \Delta M_B = 0$$

$$(I_{zx} + \Delta N_{\dot{p}})\ddot{\Delta\phi} + (\Delta N_p + \Delta N_{\dot{\beta}}\sin\alpha_r)\dot{\Delta\phi} + (\Delta N_\beta \sin\alpha_r)\Delta\phi \qquad (32.6)$$
$$- \Delta N_p(\Delta\Omega_x^h \cos\alpha_r) - \Delta N_R(\Delta\Omega_x^h \sin\alpha_r) - \Delta N_B = 0$$

2.3 REDUCTION FORMULATION

The equations of motion for the constrained wind tunnel model developed in the previous sections have the form of second order differential equations. However, in the case of forced roll oscillation, the roll displacement and conse-

quently the associated roll rates are specified functions of time. In most cases, and for the case considered here, the displacement and rate are sinusoidal functions. As a result, the aerodynamic terms in the governing equations can be developed in terms of "in-phase" and "out-of-phase" components. These components are obtained using procedures which are quite similar to those used to determine the coefficients of a Fourier sine or cosine series.

In the following discussions, the expression "in-phase derivative" denotes a component of the aerodynamic reaction which occurs in phase with the oscillating displacements associated with the forced sinusoidal oscillation test, and could be associated with the coefficient of a sine term in a Fourier series. The portion of the aerodynamic reaction which would be associated with the coefficient of a cosine term in a Fourier series is 90 degrees out of phase with the oscillation displacements and is called the "out-of-phase derivative".

In general, the model is oscillated in a sinusoidal fashion about one of the body axes in the wind tunnel air stream. Data taken during the tests includes the time history of the model position and time history of various components of the forces and moments applied to the model through

the strain gage balance used to support the model. The unique feature in the study is that this oscillatory motion is carried out in a non-uniform air stream provided by the curved and rolling flow test sections of the VPI&SU stability tunnel.

Here, two distinct procedures are applied to the data obtained from the forced roll oscillation tests about x-body axis with these upstream non-uniform flows. The first procedure is applied to the data associated with the forced oscillation to yield the combined oscillatory derivatives ($C_{i_\beta}\sin\alpha_r-(k_1)^2C_{i_{\dot{p}}}$, $C_{i_p} + C_{i_{\dot{\beta}}}\sin\alpha_r$) by employing standard single d.o.f. forced oscillation for prescribed displacement in time. The second procedure is used to obtain the combined damping derivatives ($C_{i_p}\sin\alpha_r - C_{i_r}\cos\alpha_r$, $C_{i_p}\cos\alpha_r + C_{i_r}\sin\alpha_r$). This latter procedure is applied to the data related to the sinusoidal oscillation by considering the angular variations due to upstream non-uniform flows.

2.3.1 Forced Oscillation in Roll with Local Curved Flow

The rolling moment equation { Eq. (29.4) } due to angular oscillation about x-body axis with upstream curved flow can be written in the following form.

$$\Delta L_B = (-I_x + \Delta L_{\dot{p}})\ddot{\Delta\phi} + (\Delta L_p + \Delta L_{\dot{\beta}}\sin\alpha_r)\dot{\Delta\phi} + (\Delta L_\beta \sin\alpha_r)\Delta\phi \quad (33)$$
$$+ \Delta L_p(\Delta\Omega_z^h \sin\alpha_r) - \Delta L_R(\Delta\Omega_z^h \cos\alpha_r)$$

The difference between the wind-on and the wind-off balance measurement is the reaction due to aerodynamic terms only, i.e, the effect of inertia and gravity are eliminated. Therefore, Equation (33) can be written such that:

$$(\Delta L_B)_W - (\Delta L_B)_V = \Delta L_{\dot{p}}\ddot{\Delta\phi} + (\Delta L_p + \Delta L_{\dot{\beta}}\sin\alpha_r)\dot{\Delta\phi} \quad (34)$$
$$+ (\Delta L_\beta \sin\alpha_r)\Delta\phi + \Delta L_p(\Delta\Omega_z^h \sin\alpha_r) - \Delta L_R(\Delta\Omega_z^h \cos\alpha_r) = 0$$

where, $(\ )_W$ denotes wind-on measurement and $(\ )_V$ denotes wind-off measurement of the balance output voltage signals.

The sinusoidal oscillating displacement in time about the x-body axis and angular motion due to upstream curved flow (Ref. 23) can be written respectively as follows,

$$\Delta\phi = \Delta\phi_{max} \sin\omega t \quad (35)$$

$$\Delta\Omega_z^h = V/R_o = \text{constant} \quad (36)$$

where V denotes the local velocity due to curved flow angularity, R_o denotes the local radius of the curvature.

The balance output associated with the roll channel is given by an electrical signal proportional to the rolling moment such that

$$\Delta e_1 = (e_1)_W - (e_1)_V = k_1 E\{(\Delta L_B)_W - (\Delta L_B)_V\} \quad (37)$$

where, k_1 denotes the balance calibration factor about x-axis and E denotes the strain-gage supply voltage.

By multiplying Equation (37) by an in-phase voltage or out-of-phase voltage signal, we get

$$E_{in} = \Delta e_1 \, E_R \sin\omega t \quad (38.1)$$

$$E_{out} = \Delta e_1 \, E_R \cos\omega t \quad (38.2)$$

By applying Equations (34) - (36) to Equation (38), we have

$$E_{in} = E_R k_1 E \sin\omega t\{(-\omega^2 \Delta L_{\dot{P}} + \Delta L_\beta \sin\alpha_r)\Delta\phi_{max}\sin\omega t + (\Delta L_P + \Delta L_{\dot{\beta}}\sin\alpha_r)\omega\Delta\phi_{max}\cos\omega t + \Delta\Omega_z^h(\Delta L_P \sin\alpha_r - \Delta L_R \cos\alpha_r)\} \quad (39.1)$$

$$E_{out} = E_R k_1 E \cos\omega t\{(-\omega^2 \Delta L_{\dot{P}} + \Delta L_\beta \sin\alpha_r)\Delta\phi_{max}\sin\omega t + (\Delta L_P + \Delta L_{\dot{\beta}}\sin\alpha_r)\omega\Delta\phi_{max}\cos\omega t + \Delta\Omega_z^h(\Delta L_P \sin\alpha_r - \Delta L_R \cos\alpha_r)\} \quad (39.2)$$

Integrating Equation (39) over one or more periods gives the average values of the signals such that

$$\overline{E_{in}} = \frac{1}{nT}\int_{t_o}^{t_o+nT} E_{in}dt = \frac{E_R k_1 E\Delta\phi_{max}}{2}(-\omega^2\Delta L_{\dot{p}} + \Delta L_\beta \sin\alpha_r) \quad (40.1)$$

$$\overline{E_{out}} = \frac{1}{nT}\int_{t_o}^{t_o+nT} E_{out}dt = \frac{E_R k_1 E\omega\Delta\phi_{max}}{2}(\Delta L_p + \Delta L_{\dot{\beta}} \sin\alpha_r) \quad (40.2)$$

where n denotes numbers of period of oscillation.

Finally, the unknown in-phase and out-of-phase nondimensional derivatives can be derived in terms of known values from Equation (40).

$$C_{l_\beta}\sin\alpha_r - \left(\frac{\omega b}{2V_\infty}\right)^2 C_{l_{\dot{p}}} = \frac{2}{q_\infty S b E_R k_1 E\Delta\phi_{max}}\overline{E_{in}} \quad (41.1)$$

$$C_{l_p} + C_{l_{\dot{\beta}}}\sin\alpha_r = \frac{4V_\infty}{q_\infty S b^2 E_R k_1 E\omega\Delta\phi_{max}}\overline{E_{out}} \quad (41.2)$$

Additional information can be obtained from Equation (38) by carrying out procedures similar to those used to develop Equation (41). The result of these operations will lead to a combination of pure rotary or damping derivatives. In particular we can multiply Equation (38.1) and Equation (38.2) by sin(ωt) and cos(ωt) respectively to give

$$E_{in}\ (\text{pure}) = \Delta e_l E_R \sin^2 \omega t \tag{42.1}$$

$$E_{out}(\text{pure}) = \Delta e_l E_R \cos^2 \omega t \tag{42.2}$$

Substituing Equations (34), (35) and (36) into Equation (42) and integrating the resulting equations over one or more periods, the following non-dimensional combination of pure rotary derivatives can be obtained.

$$C_{l_p} \sin\alpha_r - C_{l_r} \cos\alpha_r = \frac{4V_\infty}{q_\infty S b^2 \Delta\Omega_z^h E_R k_l E} \overline{E_{in}(\text{pure})} \tag{43.1}$$

$$C_{l_p} \sin\alpha_r - C_{l_r} \cos\alpha_r = \frac{4V_\infty}{q_\infty S b^2 \Delta\Omega_z^h E_R k_l E} \overline{E_{out}(\text{pure})} \tag{43.2}$$

If we apply similar procedures to the other set of governing equations included in Equation (29) we have oscillatory and combined damping derivatives. Table 3 describes the coefficients obtained from conventional forced oscillation techniques and the combined form of rotary derivatives can be found in Table 4 .

2.3.2 Forced Oscillation in Roll with Local Rolling Flow

The rolling moment equation { Eq. (32.4) } due to angular oscillation about x-body axis with upstream rolling flow can be written in the following form.

$$\Delta L_B = (-I_x + \Delta L_{\dot{P}})\ddot{\Delta\phi} + (\Delta L_P + \Delta L_{\dot{\beta}}\sin\alpha_r)\dot{\Delta\phi} + (\Delta L_\beta \dot{\sin\alpha_r})\Delta\phi \quad (44)$$
$$- \Delta L_P\,(\Delta\Omega_x^h \cos\alpha_r) - \Delta L_R(\Delta\Omega_x^h \sin\alpha_r)$$

Similar procedures as discussed in Section (2.3.1) are followed to get combined oscillatory derivatives. Upstream rolling flow changes the free stream angular velocity such that (Ref. 24).

$$\Delta\Omega_x^h = V_T \,/\, R = \text{constant} \quad (45)$$

where, V_T denotes transverse velocity due to roll rate, and R denotes the radius measured from tunnel centerline.

The reaction due to aerodynamic terms only can be obtained by taking the difference between the wind-on and wind-off balance measurements. Multiplying the reaction equations by modified in-phase voltage or the out-of-phase voltage signals and applying the constraint equation (Eq. 44) in addition to Equations (35) and (45), we have

$$E_{in}\,(\text{pure}) = E_R k_1 E \sin^2\omega t\{(-\omega^2 \Delta L_{\dot{P}} + \Delta L_{\dot{\beta}}\sin\alpha_r)\Delta\phi_{max}\sin\omega t \quad (46.1)$$

$$+ (\Delta L_P + \Delta L_{\dot{\beta}} \sin\alpha_r)\omega\Delta\phi_{max}\cos\omega t - \Delta\Omega_x^h(\Delta L_P\cos\alpha_r + \Delta L_R\sin\alpha_r)\}$$

$$E_{out}(pure) = E_R k_1 E \cos^2\omega t\{(-\omega^2\Delta L_{\dot{P}} + \Delta L_\beta \sin\alpha_r)\Delta\phi_{max}\sin\omega t \quad (46.2)$$
$$+ (\Delta L_P + \Delta L_{\dot{\beta}} \sin\alpha_r)\omega\Delta\phi_{max}\cos\omega t - \Delta\Omega_x^h(\Delta L_P\cos\alpha_r + \Delta L_R\sin\alpha_r)\}$$

Integrating over one or more periods of the above equation give the average values of the signals such that:

$$\overline{E_{in}(pure)} = \frac{1}{nT}\int_{t_o}^{t_o+nT} E_{in}(pure)dt = -\frac{E_R k_1 E\Delta\Omega_x^h}{2}(\Delta L_P\cos\alpha_r + \Delta L_R\sin\alpha_r) \quad (47.1)$$

$$\overline{E_{out}(pure)} = \frac{1}{nT}\int_{t_o}^{t_o+nT} E_{out}(pure)dt = -\frac{E_R k_1 E\Delta\Omega_x^h}{2}(\Delta L_P\cos\alpha_r + \Delta L_R\sin\alpha_r) \quad (47.2)$$

Finally, the unknown in-phase and out-of-phase nondimensional damping derivatives can be derived in terms of known values from Equation (47).

$$C_{l_p}\cos\alpha_r + C_{l_r}\sin\alpha_r = -\frac{4V_\infty}{q_\infty Sb^2\Delta\Omega_x^h E_R k_1 E}\overline{E_{in}(pure)} \quad (48.1)$$

$$C_{l_p}\cos\alpha_r + C_{l_r}\sin\alpha_r = -\frac{4V_\infty}{q_\infty Sb^2\Delta\Omega_x^h E_R k_{l_E}}\,\overline{E_{out(pure)}} \qquad (48.2)$$

These sets of combination of pure rotary derivatives can be found on Table 4.

Chapter III

TEST FACILITIES AND TECHNIQUES

3.1 WIND TUNNEL

The VPI&SU subsonic 6 foot stability wind tunnel is a continuous, single return type with interchangeable square, curved and round test sections. By using a 600 h.p. d.c. motor, the 14 foot, 8 bladed propeller driving system produces a dynamic pressure up to 40 psf. The 10 to 1 nozzle contraction ratio of the tunnel along with the 7 stainless steel turbulence screens in the settling chamber make it operate at a low free stream turbulence level of about 0.03 % maximum.

The curved flow 6 ft. by 6 ft. test section has vertical walls which are designed to have enough flexbility so that they may be deflected into a curve, creating a curved air flow necessary to simulate flight in a curved path. Jack screws positioned at regular intervals along each wall, allow the curvature to be set at a prescribed value. The wire screens which are located upstream of the test section, vary in mesh across the wind tunnel (densest position is located toward the center of curvature), in order to produce the desired velocity gradient across the tunnel flow. There are

four possible curved flow conditions ranging from rb/2V = 0.0 to 0.063 (based on 2.525 ft. wing span) at a dynamic pressure of q_∞ = 16 lbs/ft^2. Details of curved flow theory, calibration, and tunnel operations are given in Reference 23. A sketch of a typical curved flow test arrangement is presented in Figure 3 (Ref. 23).

The rolling flow test section is 24 ft. long and has a nominal diameter of 6 ft. It provides a means for rolling the air flow to simulate flight with rolling motion about the relative free stream wind vector. On the transition region where the tunnel cross section changes from square to round, a rotor of diameter 6.25 ft. is installed which is driven by a 40 h.p. d.c. motor and is capable of rotating at variable speeds up to approximately 100 r.p.m. Nine equally spaced steel vanes in the rotor (Fig. 4) (Ref. 24) are specially shaped and provide solid core vortex motion on the air passing through the test section. Non-dimensional rates up to pb/2V = $\pm$ 0.056 {(based on 2.525 ft. wing span; $\hat{p}$ = 0.056 (rotor motor tachometer 1250 r.p.m. ,c.c.w.), $\hat{p}$ = -0.056 (rotor motor tachometer -1120 r.p.m., c.w.)} at a dynamic pressure of 16 lbs/ft^2 are possible. A sketch of the overall rolling flow test section is shown in Figure 5 (Ref. 24). A calibration procedure along with its results for the rolling flow test section is given in Reference 31.

There are provisions for mounting a model by using a pylon supported sting mount in the curved or rolling flow test section, and angle of attack can be varied from 0 to 45 degrees. Unlike to the curved flow test section, where the turn table slide mechanism allows sideslip angles from - 10 to 10 degrees, the rolling flow test section can not be operated at arbitrary sideslip and angle of attack combinations, since the pylon is rigidly fastened to the rolling flow test section walls. However, arbitrary combinations of roll angle and sting angle can be converted to a set of aero-dynamic angles (Refs. 11,12,24), such that in general

$$\tan\alpha = \tan\theta \cos\phi + \sin\phi \tan\psi / \cos\theta \qquad (49)$$

$$\sin\beta = \sin\phi \sin\theta \cos\psi - \cos\phi \sin\psi \qquad (50)$$

The test conditions for the curved and rolling test sections, were set by adjusting the tunnel speed so that the pressure drop measured across the nozzle contraction ahead of the test section corresponded to that which was recorded for the selected speed measured in the test section with model. The nominal values used for the tests were a pressure drop of 1.23 in (0.031 m) of water in the curved flow test section and 1.28 in (0.033 m) of water for rolling flow test section corresponding to a dynamic pressure of q_∞ = 16

lbs/ft^2 (766.084 N/m^2) in both occupied test sections. The speed corresponds to Reynolds number of about 5.5 x 10^5 based on the mean aerodynamic chord {0.771 ft (0.235 m)} of the F-5 model.

3.2 ROLL OSCILLATORY RIG

The VPI&SU forced roll oscillatory rig was designed to be operated in both the curved and rolling flow test sections. In order to meet this requirement, its size had to be limited so that it could be used with the current support system. A sketch of the device for a typical test setup is given in Figure 6. In general, the object of designing the rig was to be able to examine the pure rotary stability derivatives obtained from static tests in the curved and rolling flow test sections, the combined derivatives associated with the usual oscillatory test, and the derivatives which are obtained by combining the previous two test techniques. In addition these various tests are accomplished with the same model in the same wind tunnel.

It was this requirement of compatibility which restricted the design to be limited in size as indicated above. The entire oscillatory rig is supported by a pylon which is fas-

tened to the ceiling and floor of the wind tunnel via small turntables in the case of the curved flow test section and fastened directly in the case of the rolling flow test section. The pylon is capable of varying the pitch angle of the model through a continuous range of angle-of-attack up to about 45 degrees. The turntable in the curved flow test section allows variations in the angle of yaw (relative to the tunnel centerline) continuously up to ± 10 degrees (see Section 3.1). In all cases, the model is located at the center of the test section.

The oscillatory rig is mounted on the pylon by two supporting arms, one on each side. These arms are designed with a dog-leg shape to provided the required angle-of-attack range. On the model side of the rig is a 1 and 3/4 inch sting support which supports a strain gage balance which in turn supports the model. This sting can be oscillated in roll at various frequencies and amplitudes.

The sting oscillation is driven by a variable speed 3/4 h.p. permanent magnet d.c. motor through a 10 to 1 speed reducer which in turn is connected to a scotch-yoke mechanism { Fig. (6) }. This drives an inverse yoke assembly which in turn drives the sting in an oscillatory motion in roll. The use of the two scotch-yoke like mechanisms allows the device

to be small, but still retain the sinusoidal motion in the roll angle and rate which is desired. Furthermore, the large gear ratio in the drive system allows a smaller motor to be used since the torque remains high. The speed of the motor is adjusted by varying the voltage of the input power supply allowing selected frequencies up to approximately 3 hertz. The amplitude of the oscillatory motion is controlled by varying the locations of the roller on the scotch-yoke flywheel along its radius. This adjustment occurs in discrete steps up to ± 22.6 degrees. Table 5 describes the available roller position versus the roll amplitude angle and operating frequency range of the VPI&SU roll oscillatory rig.

A precision sine-cosine potentiometer (0.5 degree accurate in rotational angle), is powered by 200 mvolt power supply. It generates voltage signals (±100 mvolt maximum) proportional to the sine and cosine of the flywheel rotational angle which in turn is related to the angular displacement of the model. These signals along with the balance signals are used in the data reduction procedure which will be described in Section 3.5 .

3.3 BALANCE AND MODEL

As mentioned previously, the model is attached to the sting by an internally mounted 6 component strain gage balance. The balance is supplied by a nominal voltage of 5 volts and, using bridge type circuits, puts out voltages proportional to the forces (normal, axial and side) and moments (roll, pitch and yaw). The constants of proportionality are determined by calibrating the balance.

The calibration procedure used here is that known as a span check. Since the output voltages are small (millivolts) changes in power supply voltage, and cable lengths, all parameters of the local environment can offset the calibration. Consequently, when a strain gage balance is originally calibrated, an additional step is taken to allow for system characteristics to be accounted for without the necessity of a completely new calibration on site. This additional step is that of a span check. Here a precision resistor is applied across part of the bridge circuit to "load" the balance and a corresponding output voltage reading taken. The same resistor is inserted in the bridge circuit in the local environment and an output voltage recorded. By comparing these results, a correction to the original calibration can be made to account for local system differences.

Once done, a few carefully placed weights are used to confirm the local calibration. It was assumed that no cross coupling exists in the balance.

The general balance characteristics and calibration data used throughout the tests are presented in Table 6.

The investigation was conducted with a 1/10 scale model of the F-5 spin resistance fighter designed for intercept and dog-fight operations. The model is constructed primarily of molded fiberglass and is the same model that was used in References 9 and 11 and similar to that used in Reference 25. A three view sketch showing the general layout of the model is shown in Figure 7 and a summary of the geometric properties of the model is presented in Table 7 .

The model and balance when mounted on the sting support system is such that the balance moment center is located at 18 percent of the mean aerodynamic chord. The vertical location of the moment reference center was 0.02 percent of the mean aerodynamic chord above the wing-chord reference line at the plane of symmetry.

3.4 TESTING PROCEDURES

The testing procedure used in the static and forced oscillation tests employing the VPI&SU SWT with roll oscillatory rig can best be explained by describing a typical test. The general sequence of events which occur in the static and dynamic tests is summarized as follows:

1. Select the desired test conditions including angle of attack and sideslip angle and set the model at the proper attitude.

2. Adjust the output signal of the sine-cosine potentiometer to zero with the oscillatory mechanism set so that the model wings are level. Measure the static wind-off forces and moments.

3. Turn on the wind until the nominal dynamic pressure is reached (for rolling flow, the dynamic pressure in the occupied test section with the rotor at rest) and measure the static wind-on forces and moments.

4. Oscillate the model to desired amplitude and frequency in the wind on condition for dynamic tests. Read the sinusoidal input signals and balance output signals. Then store those data in the controller buffer (see Section 3.5).

5. Turn off the wind but continue to oscillate the model, then read and store the wind-off data in the same manner as for step 4.

The above procedure is controlled by the data acquisition system. Once the initial position of the model is set and the sine-cosin potentiomter nulled with the wing level, the system takes the appropriate data and instructs the operator when to start or stop the tunnel and when to start or stop the model oscillation.

3.5 DATA ACQUISITION AND REDUCTION

The VPI&SU data acquisition system is used for measuring static and dynamic stability parameters on a wind tunnel model undergoing static or roll oscillatory motion in a curved or rolling flow environment. A general layout for static/dynamic data acquisition system is shown in Table 8. The system centers about Hewlett-Packard 3052A automatic data acquisition system.

As mentioned in the previous section (Section 3.4), static and dynamic data reductions can be done in sequence with single push button operations.

In the curved or rolling flow static tests, except for the wall or rotor settings, the 6 component balance reaction data are recorded as for conventional static testing. The standard tunnel blockage corrections are made {same as Refs. (9-12), originally quoted from Ref. 26 }. Additionally when the curved flow test section is employed, pressure gradient corrections as discussed in References 9 and 23 are applied.

The strain gage balance readings are taken via a digital voltmeter (HP 3455, 6 1/2 digit accuracy) by taking the average of 15 samples of 6 component reaction signals taken over an 8 second time interval. Correcting these readings for blockage effects and pressure gradient effect, if needed, and dividing the corrected force and moment readings (wind on - wind off) by the corrected dynamic pressure and appropriate geometric constants leads to non-dimensional 6 component static reactions in both body and stability axes system.

Since yaw or roll rates are in stability axes system, it is necessary to transform the above forces and moments from the stability axes system to the body axes system to obtain the body axes system pure rotary derivatives (C_{y_p} , C_{l_p} , C_{n_p} , C_{y_r} , C_{l_r} , C_{n_r}). The transformation matrix can be written as follows.

$$[A]^b = [T]_{bs}[A]^s[T]_{sb} \qquad (51)$$

where, $[A]^s = \begin{bmatrix} C_{l_p} & 0 & C_{l_r} \\ 0 & C_{m_q} & 0 \\ C_{n_p} & 0 & C_{n_r} \end{bmatrix}^s$ or, $\begin{bmatrix} 0 & C_{x_q} & 0 \\ C_{y_p} & 0 & C_{y_r} \\ 0 & C_{z_q} & 0 \end{bmatrix}^s$

$$[T]_{bs} = \begin{bmatrix} \cos\alpha & 0 & -\sin\alpha \\ 0 & 1 & 0 \\ \sin\alpha & 0 & \cos\alpha \end{bmatrix}$$

$$[T]_{sb} = [T]_{bs}^{-1} = [T]_{bs}^{T}$$

The lateral static stability derivatives (C_{y_β}, C_{l_β}, and C_{n_β}) can be obtained from the static lateral data by taking the difference in the values of the coefficients at $\pm \Delta\beta$ (nominally ± 5 degrees) and dividing by $2\Delta\beta$. The second order mixed derivatives ($C_{i_{\beta p}}$, $C_{i_{\beta r}}$) can be obtained from the static lateral data C_{i_β} by taking the difference in the values of the coefficients at $\pm\hat{\Delta p}$ (nominally ± 0.047) or at $\pm\hat{\Delta r}$ (nominally ± 0.0497) and dividing by $2\hat{\Delta p}$ or $2\hat{\Delta r}$. $C_{i_{p\beta}}$ and $C_{i_{r\beta}}$ can be obtained from C_{i_p} or C_{i_r} by taking the difference in the values of the coefficient at $\pm\Delta\beta$ (nominally ± 5 degrees).

For the case of dynamic test, whose reduction program is presented in Table 9, the input sinusoidal function and the output balance reaction signals (forces and moments) can be measured at the same instant of time. By employing the channel scanner (HP 3495, 1000 readings/second) and high speed voltmeter (HP 3437A, 3 1/2 digit accuracy), resulting sampling time interval between each force and moment signal was 1 msec. The sampling rate of each signal was 72 readings per cycle for 2 Hz. forced oscillation, giving a total sampling time of about 500 msec for one cycle. The relationships of the oscillation frequency and the number of readings of those reaction signals for other oscillation frequencies are presented in Table 10.

It was assumed that the input oscillating motion of the model has the same period as that of the rotating motion of the flywheel, hence the attitude of the model or flywheel at a certain time can be determined by utilizing the measured sinusoidal signals and known sampling time (gate time of the channel scanner).

Consequently, the stored reaction data in the computer buffer (HP 9836, 1 megabyte core memory) can be used in the calculation procedure with the known input sinusoidal function properties (initial angle, period of oscillation). By

using Equation (39) and (46) in Section 2.3, input sinusoidal and output reaction signals are multiplied with each other on a real time basis. Then those multiplied values are integrated by applying trapezoidal schemes to Equations (40) and (47) in Section 2.3 . Normally the average of the 4 procedures (measurement, multiplication and integration) are performed and they are terminated by an internal software command.

The error estimation of the above signal processing and calculations was done by using trapezoidal discrete integration and the property of the sinusoidal functions such that

$$Er=\frac{\pi}{n-1}\left[\sum_{i=2}^{n-1}\left\{2\sin^2\left(A+\frac{2\pi(i-1)}{n-1}\right)\right\}+\left\{\sin^2 A+\sin^2(A+2)\right\}\right]-\pi \tag{52}$$

where, A denotes starting sine function angle (initial angle, radian) and n denotes number of sampling measurements for one cycle.

Finally, in-phase and out-of-phase damping derivatives and combination of pure rotary derivatives in body axes system were obtained by using the reduction equations {Eqns. (41), (43), (48)} in Section 2.3 .

The differences of C_{i_β} (static data) and $C_{i_\beta}\sin\alpha_r - (k_1)^2 C_{i_{\dot{p}}}$ (out-of-phase dynamic data, roll oscillation) were determined to obtain $C_{i_{\dot{p}}}$. The differences of C_{i_p} (static data) and $C_{i_p} + C_{i_{\dot{\beta}}}\sin\alpha_r$ (in-phase dynamic data, roll oscillation) were used to determine the unsteady translational derivative $C_{i_{\dot{\beta}}}$. The differences of the static test results (C_{i_β}, C_{i_r}) and yaw oscillation dynamic test results $\{C_{i_\beta}\sin\alpha_r + (k_1)^2 C_{i_{\dot{r}}}, C_{i_r} - C_{i_{\dot{\beta}}}\sin\alpha_r\}$ yielded the unsteady dynamic derivatives $C_{i_{\dot{r}}}$ and $C_{i_{\dot{\beta}}}$.

Chapter IV

PRESENTATION OF RESULTS

The wind tunnel data presented herein were obtained with a 1/10-scale F-5 model tested in both the curved and rolling flow test sections of the VPI&SU SWT as discussed in the previous chapter. Additional data were obtained from reports (Ref. 25) of testing a similar aircraft, (0.17-scale model) at the Langley research center in the 30-by 60-foot tunnel open-throat test section.

The Reynolds number for each set of tests based on the mean aerodynamic chord of the basic wing was about 5.5×10^5 for the tests at VPI&SU and 6.5×10^5 for the tests carried out at the Langley research center. Both models are basically the same F-5 configuration and complete descriptions of their geometric characteristics are listed in Table 7 (Ref. 9) and Table 11 (Ref. 25) respectively.

The static and roll oscillatory tests at VPI&SU were carried out for angles of attack from 0° to 45° in five degree increments. Three different sideslip angles (-5°, 0°, 5°) were selected for the curved flow with roll oscillatory tests, but only a zero sideslip angle was used for the rolling flow with roll oscillatory tests. For each attitude,

non-dimensional yaw rates (rb/2V = 0 and 0.0497) and non-dimensional roll rates pb/2V = 0, 0.026, ±0.047, and 0.056 were selected. For forced oscillation in roll test, the selected reduced frequencies (ωb/2V) for the VPI&SU SWT data are 0.033 (0.5 Hz. oscillation) , 0.066 (1 Hz. oscillation) and 0.133 (2 Hz. oscillation) with the amplitude fixed at ±4.4 degrees. The dynamic tests (forced oscillation in roll and yaw) at the Langley research center were made with a reduced frequency of 0.181 (1 Hz. oscillation) and an angular amplitude of ±5 degrees.

The stability characteristics which were measured in the investigation are presented individually under the general classification of static longitudinal and lateral characteristics, lateral in-phase oscillatory derivatives and lateral out-of-phase derivatives. Those stability derivatives are presented as plots of the non-dimensional force and moment coefficients in body axes (see Section 3.5) except for the static longitudinal coefficients, where the conventional stability axes system is used.

The stability data obtained are summarized as follows:

1. Static longitudinal characteristic curves (C_m, C_L , C_D vs. α) obtained in the VPI&SU curved flow, rolling flow

test sections and the Langley full scale wind tunnel. [Fig. 8]

2. Static lateral characteristic curves (C_{y_β}, C_{l_β}, C_{n_β} vs. α) obtained in the VPI&SU SWT and the Langley full scale wind tunnel. [Fig. 9]

3. Static lateral characteristic curves for different non-dimensional yaw rates ($\hat{r}$ = 0, -0.0497) and non-dimensional roll rates ($\hat{p}$ = 0, 0.038) obtained in the VPI&SU SWT. [Fig. 10, 11]

4. The out-of-phase roll oscillatory data (C_{i_p} + $C_{i_{\dot{\beta}}} \sin\alpha_r$ vs. α) obtained in the VPI&SU curved flow test section (k_1= 0.133), rolling flow test section (k_1= 0.133) and the Langley full scale wind tunnel (k_1= 0.181). [Fig. 12]

5. The in-phase roll oscillatory data ($C_{i_\beta} \sin\alpha_r$ - $(k_1)^2 C_{i_{\dot{p}}}$ vs. α) and out-of-phase roll oscillatory data (C_{i_p} + $C_{i_{\dot{\beta}}} \sin\alpha_r$ vs. α) at different non-dimensional yaw rates ($\hat{r}$ = 0, -0.0497) and sideslip angles ($\beta = 0^\circ, 5^\circ, -5^\circ$) obtained in the VPI&SU curved flow test section. [Fig. 13, 14, 15, 16, 17, 18]

6. The out-of-phase oscillatory data (C_{i_p} + $(k_1)^2 C_{i_{\dot{\beta}}} \sin\alpha_r$ vs. α) at different non-dimensional roll rates

($\hat{p}$ = 0, 0.026, ±0.047, 0.056) obtained in the VPI&SU rolling flow test section (k_1= 0.133, k_1= 0.066, k_1= 0.033).

[Fig. 19, 20, 21, 22]

7. The combined pure rotational data ($C_{i_p} \cos\alpha_r + C_{i_r} \sin\alpha_r$ vs. α) at different non-dimensional roll rates ($\hat{p}$ = 0, 0.026, ± 0.047, 0.056) obtained in the VPI&SU SWT. [Fig. 23, 24]

8. The pure rotational data (C_{i_p} , C_{i_r} vs. α) at different sideslip angles ($\beta = 0^\circ, 5^\circ, -5^\circ$) obtained in the VPI&SU SWT. [Fig. 25, 26]

9. The static data (C_{i_β} , C_{i_p} , C_{i_r} vs. α) and oscillatory data $\{C_{i_\beta} \sin\alpha_r - (k_1)^2 C_{i_{\dot{p}}}$, $C_{i_p} + C_{i_{\dot{\beta}}} \sin\alpha_r$, $C_{i_r} - C_{i_{\dot{\beta}}} \cos\alpha_r\}$ obtained in the VPI&SU SWT and the Langley full scale wind tunnel. [Fig. 27, 28, 29]

10. The second order mixed derivatives ($C_{i_{\beta p}}$, $C_{i_{p\beta}}$, $C_{i_{\beta r}}$ and $C_{i_{r\beta}}$ vs. α) obtained in the VPI&SU SWT. [Fig. 30, 31]

Chapter V

DISCUSSION OF RESULTS

As discussed earlier (Chap. I), a vehicle flying at high angle of attack can have stability parameters which vary over a wide range and which generally are strongly connected to complex flow characteristics as well as to local geometric definition of the aircraft. To study this overall problem, the static and dynamic force and moment coefficients presented in the previous chapter will be analyzed to determine individual changes due to changes in α, β, r and p.

The analysis is presented in three sections. The first section includes comparison of static data taken in the various facilities to insure integrity of the data. In addition the general characteristics of the flow field are obtained. The second section deals with a discussion of the characteristics of the dynamic derivatives including the effects of attitude and angular rate on selected derivatives. Finally in section three, the results of the various wind tunnel tests are included in two different aerodynamic models. These two models are used in a linearized analysis to predict dynamic behavior. Comparisons of the resulting dynamic characteristics are made and details of the effects of

changes in the aerodynamic model on these effects are investigated.

5.1 STATIC STABILITY DERIVATIVES

5.1.1 Static Longitudinal Characteristics

The static longitudinal characteristics of the complete configuration are presented in Figure 8. The data denoted by square symbols are those obtained in the VPI&SU curved flow test section; the circular symbols denote data obtained in the VPI&SU rolling flow test section ; the triangle symbols denote data obtained in the Langley full-scale wind tunnel. The data indicate good agreement with the exception of the VPI&SU curved flow wind tunnel data (C_L and C_D vs. α) in the angle-of-attack range of 25° to 45° . It is believed these differences are due to an inadequate blockage correction used for the curved flow test section. The differences are relatively small and will be ignored for the remainder of the discussion.

From Figure 8, it can be observed that the slope of the lift curve changes abruptly at about 17° which corresponds to the wing stall angle (Ref. 25). At this point, as the wing lift is reduced, the flat bottom of the fuselage and

the tail surfaces increase their contribution to the lift as indicated by the continually increasing lift coefficient with increasing angle of attack as well as the increasing negative pitching moment. This contribution of lift should be noted for future reference.

5.1.2 Static Lateral Characteristics

Comparison of the static lateral-directional characteristics is presented in Figure 9 in terms of the static stability derivatives C_{y_β}, C_{l_β}, and C_{n_β}. The square symbols in the Figure 9 denote the average of the C_{i_β} obtained in the curved and rolling flow test sections. Considering the method of computing the slope (C_i vs. β) (see Section 3.5), the agreement is quite good at angles of attack up to about 30°. Beyond 30° the curves show similar trends but are different. Results such as these are typical for conditions where the flow is separated, and illustrates what is usually associated with data scatter in these regions.

At low angles of attack the values of C_{y_β} and C_{n_β} remain nearly constant at their respective zero angle of attack value up until about 15°, the region where the wing flow starts to separate. At this point the value of C_{y_β}

increases with angle of attack while C_{n_β} dips to near zero at 25° angle of attack after which it increases with angle of attack. This combination of changes in C_{y_β} and C_{n_β} beyond 25° angle of attack indicates the side force is increasing in the positive direction for positive sideslip and its center of pressure is located forward near the nose region. This phenomena is discussed elswhere (Ref. 14) and is attributed to the asymmetric shedding of vortices from the region of the vehicle nose. The windward vortex tends to remain close to the fuselage and to follow it back over the wing to the neighborhood of the vertical tail surface generally weakening as it flows aft. The leeward vortex on the other hand separates from the fuselage and tends to follow a free streamline carrying it away from the vehicle rendering its effects negligible. The result is low pressure on the windward side of the nose tending to draw it toward the flow direction. The dip in the C_{n_β} curve at 25° angle of attack occurs when the vertical tail loses its effectiveness and the asymmetric vortex system is not yet fully developed.

The dihedral effect represented by C_{l_β} shows an additional effect of the windward nose vortex. In general the presence of the vortex along the windward side of the fuselage enhances the lift on the windward wing by causing the separation of the flow to be delayed until higher angle of

attack. The result of this delay is to maintain a higher lift on the windward wing causing a stabilizing rolling moment. From Figure 9 it can be seen that as the vertical tail loses its effectiveness (indicated by decreasing C_{l_β}), the asymmetric lift maintains the negative value of C_{l_β}. Again more details concerning the flow field about the vehicle are given in Reference 14.

From the above descriptions the principal flow field characteristics can be identified, the main wing separation, and the asymmetric nose vortex. These are the dominant features that will be investigated in the following.

Figure 10 shows the effect of curved flow on the static lateral-directional stability coefficients. The values of C_{y_β} and C_{n_β} are more positive for the straight flow than the corresponding values measured in the curved flow. The opposite is true for the dihedral effect C_{l_β}. In general, these differences are smaller at the lower angles of attack and increase rather suddenly for angles of attack greater than 15°. All these results are consistent with the theory that the asymmetric nose vortex effects are reduced at the higher sideslip angles and strongest at zero sideslip. When the model is immersed in curved flow, the sideslip angle that the nose "sees" is different from that of the aircraft.

In particular, if the aircraft is at a positive sideslip, the nose is tending toward zero sideslip. On the other hand, a negative sideslip of -5° will cause relative sideslip at the nose of greater magnitude, -8° for example (see Fig. 3). As a result, the average value of sideslip at the nose is greater in curved flow than in straight flow, reducing their contribution at the higher angles of attack. Since this flow characteristic dominates the high angle of attack region, one would expect the β static stability derivatives to be reduced in magnitude in the curved flow.

Figure 11 shows the effect of roll rate variation on the static lateral-directional stability derivatives. As in the case of the curved flow discussed previously, the rolling flow tends to reduce the magnitudes of all the lateral-directional stability derivatives at the higher angles of attack. The reason for this decrease is precisely the same as that for the curved flow. Since the axis of roll passes through the vehicle center of mass and is aligned with the wind vector, at high angles of attack, the nose is well off the roll axis and "sees" considerable sideslip caused by the roll rate. As a result the effects of the asymmetric nose vortex are reduced. Further details associated with the flow field in the rolling flow test section can be found in Reference 14.

5.2 DYNAMIC STABILITY DERIVATIVES

Comparisons of out-of-phase lateral-directional dynamic stability of the F-5 models for three different test facilities (straight flow condition) is presented in Figure 12. The data denoted by square symbols are those obtained in the VPI&SU curved test section (straight flow) with roll oscillatory rig (k_1= 0.133); the round symbols denote data obtained in the VPI&SU rolling flow test section (straight flow) with roll oscillatory rig (k_1= 0.133); the triangle symbols denote data obtained in the Langley full scale wind tunnel (k_1= 0.181). Here the general trends of all curves are similar with some differences noted at the high angles of attack. Although the scatter of the data at these high angles of attack is not unusual for oscillatory type tests, there appears to be a definite trend observed in Figure 12. The sting-pylon mount in the curved and rolling flow test sections has considerable flexibility at the high angles of attack. This flexibility shows up by allowing some sway oscillation in addition to the roll oscillation. It is felt this additional flexibility tended to bias of the data one way or the other.

5.2.1 Rolling Oscillation/Curved Flow

Comparisons of the effects of curvature on the in-phase and out-of-phase lateral-directional derivatives at different sideslip angles are presented in Figures 13 to 18.

Before examining these results in detail, it is important to describe the overall motion and its interaction with the straight and curved flow. In the straight flow at high angles of attack, asymmetric nose vortices form as discussed previously. As the model rolls about the body oriented axis with the right wing down, the relative angle of attack and sideslip angle change according to Equations (49) and (50). Consequently with a positive roll angle, the aircraft sees a positive sideslip. The windward vortex which lies along the fuselage in this case would be the one on the starboard side. As the vehicle rolls to the left, the vortex close to the fuselage shifts from starboard to port side. Exactly when this switch occurs has not been determined. One would expect that this switch would occur near the wing level position, but not necessarily at the exact wing level position. Furthermore the angle at which the switch occurs most likely is a function of the reduced frequency.

In the curved flow environment the situation is changed somewhat from that described above. As explained earlier,

when the aircraft is at zero sideslip angle, the nose "sees" some negative relative sideslip due to the curvature. Consequently when the aircraft oscillates about the body roll axis, the range of sideslip angles that the nose "sees" is no longer centered about zero. In fact the nose sideslip angle can be determined from Equation (50) where the value of ψ used is the value of the nose sideslip angle in the wing-level position. The bank angle for zero nose sideslip can be determined by setting Equation (50) equal to zero:

$$\tan\phi\big|_{\beta=0} = \tan\psi_n \,/\, \sin\theta \tag{53}$$

or, for the small angles we are involved with here

$$\phi = \psi_n \,/\, \sin\theta \tag{54}$$

It can be seen from Equation (54) that at the higher pitch angles, the bank angle for zero sideslip angle can fall within the magnitude of the roll oscillation used here (4.4°). On the other hand, below some pitch angle $\{\theta = 35^\circ$, $\psi_n = 2.53^\circ$(based on the $\hat{r} = 0.0497$), $\phi_{max} = 4.4^\circ\}$ the nose will experience only a negative sideslip angle throughout the oscillation cycle.

From the geometry of the curved flow test section it can be observed that when the aircraft is at a positive sideslip the nose tends to be aligned with the flow while at a nega-

tive sideslip position it "sees" a value larger than that set. Equation (54) indicates that for this latter condition it is likely that the relative sideslip on the nose does not change sign during an oscillation for all angles of attack. For $\beta = 0^{\circ}$ and $\beta = 5^{\circ}$, there most likely is switching in the apparent sideslip at the nose. Consequently one would expect any effects dominated by the nose vortex flow field to be stronger for the $\beta = 0^{\circ}$ and 5° cases than for the $\beta = -5^{\circ}$ case. This trend is observed in Figures 13,14 and 15, where the $\beta = -5^{\circ}$ case (Fig. 15) shows reduced magnitude in the various stability derivatives at higher angles of attack.

It is shown later that the unsteady aerodynamic terms are negligible (see Fig. 27) for these in-phase derivatives. Consequently the effects observed come from the in-phase averaging of the static forces over an oscillation cycle. From the figures it is clear that the maximum effect of curvature occurs in the side force derivative when the vehicle nose is mostly aligned with the free stream as might be expected.

The results of the out-of-phase oscillatory derivatives in roll for the straight flow are compared with the results for the curved flow at different sideslip angles in Figures 16, 17 and 18.

The combination side force parameter $C_{y_p} + C_{y_\beta} \sin\alpha_r$ for the curved flow environment is more positive than in the straight flow environment for all sideslip angles, as seen in Figures 16, 17 and 18. The combined cross derivatives of yaw moment due to roll shows a trend at the higher angles of attack where the curved flow results are greater in a positive sense then for the corresponding straight flow case for the $\beta = 0^\circ$ and $\beta = 5^\circ$ cases. For $\beta = -5^\circ$, there is no similar trend throughout the high angle of attack range. This result indicates that this effect is related to the nose vortex switching from side to side during the roll oscillation cycle. A similar occurrence is noticed for the combined roll damping parameter $C_{l_p} + C_{l_\beta} \sin\alpha_r$. Here the roll damping is more negative in the curved flow environment than in the straight flow for the case where the nominal $\beta = 0^\circ$ and $\beta = 5^\circ$. For the case where $\beta = -5^\circ$ and the relative wind approaches the nose from the same direction throughout the oscillation cycle, the roll-damping parameter is approximately the same value for both the curved and straight flow. The interaction of the nose vortex location with the roll damping occurs at the wing and tail surfaces with the near-body vortex delaying separation at the wing or influencing the flow field at the tail. The more negative values of this parameter for the curved situation indicate that the

vortex tends to remain on the same side of the fuselage during most of the oscillaton cycle. It appears that the phasing of its switching with respect to the oscillaton cycle is also important.

5.2.2 Rolling Oscillation/Rolling Flow

The variation of the out-of-phase oscillatory derivatives obtained during roll oscillation with upstream rolling flow are presented in Figures 19 to 24.

Figure 19 shows the effect of equal and opposite roll rates superimposed upon the roll oscillation. It is important to emphasize that the roll rate is about the free stream velocity vector, while the roll oscillation is about the body oriented roll axis. Since the two flow situations considered in Figure 19 are equivalent from the point of view of the aircraft, the result should be the same. The curves displayed are indeed similar with the differences being in the range of scatter usually found in oscillatory type testing. An exception of this observation occurs in the side force coefficient at the highest angle of attack. It is felt this error can be attributed to the flexibility of the support system which exhibited considerable sway in

this region. Under these conditions it is likely that the side force and possibly the yaw moment readings might be corrupted more than those for roll moment. It appears from Figure 19 that such a conjecture is true. In general, however good agreement is noted in the two cases indicating proper data acquisition.

Figures 20 and 21 show the effect of roll rate as well as reduced frequency on the combined lateral-directional derivatives. Before discussing the figures, it is important to discuss the significance of the various angular rate parameters. If the reduced frequency of oscillation is greater than the non-dimensional roll rate, the angular rate of the model exceeds the angular rate of the free stream. Under these conditions it is clear that the relative angle of attack on the wing surfaces switches sign during an oscillation cycle. On the other hand if the reduced frequency is lower than the non-dimensional angular rate, the relative angle of attack on the wing surfaces do not change sign. Actually the above discussion must be modified slightly to account for the two different roll axes. Hence the non-dimensional roll rate in the above discussion should be replaced by $(pb/2V)\cos\alpha_r$.

Figure 20 shows the result of increased roll rate on the combined lateral-directional derivatives for the case where the reduced frequency is greater than the body axis component of the non dimensional roll rate. The effects only show up for angle of attack greater than 25°. For the case of yaw and roll moment due to roll rate, the trends are well defined. The magnitudes of the combined derivatives are diminished with increasing roll rate. This trend is most likely due to the effect of roll rate on the attached nose vortex. In particular, the additional roll rate tends to carry this vortex away from the body diminishing its effect. Further comments on the mechanism for producing the observed yaw and rolling moments would be speculative.

A lower reduced frequency was used to generate Figure 21, than that used for Figure 20. Here the non-dimensional angular rate was selected so that the lower value was less than the reduced frequency while the higher value was greater than the reduced frequency. In the first case the wing angle of attack switches signs during an oscillation cycle while in the second case it does not. One would expect that the lower roll rate curves should be similar to those of the previous figure, and in fact they are similar in shape and generally larger in amplitude which is the usual effect of lowering the reduced frequency. At the higher roll rate, the values of the combined lateral-directional derivatives

are generally lower in magnitude than at the lower roll rate. Since in this case the apparent angle of attack of the wing is of constant sign, it appears that the effects of the nose vortex on the wing flow is reduced if the wing angle of attack is of constant sign.

The effects of reduced frequency on the out-of-phase derivatives is presented in Figure 22. All parameters are affected by changes in the reduced frequency for angles of attack greater than 25°. In general, the higher the reduced frequency, the smaller the magnitude of the parameter. This trend has been observed in the discussion previously and is typical in oscillating testing. Since the angle of attack region is that where the nose vortex effects are dominant, it is expected that the observed trends are related to the ability of the attached nose vortex to switch sides. At the lower oscillation frequency the switch occurs more in phase with the angular dispacement and hence more out of phase with the angular rate, creating the maximum force and moment changes with rate. As the frequency is incresed, this phasing is changed, leading to a reduction of out-of-phase force and moment components.

In Figure 23, the rectangles ($\hat{p} = -0.047$) and round symbols ($\hat{p} = 0.047$) denote the data obtained uniquely with the

VPI&SU forced roll oscillation rig used in the rolling flow environment (see Section 2.3); the triangle symbols denote the data obtained in the VPI&SU curved and rolling flow test sections without using the roll oscillatory rig. The latter is obtained from the curved and rolling flow data by converting C_{i_p} and C_{i_r} (stability axis) to body oriented stability derivatives and, subsequently multiplying these results by $\cos\alpha_r$ or $\sin\alpha_r$ respectively. As can be seen, the agreement amongst data at low angles of attack is good. At high angles of attack the curves (triangle symbols) show a some differences.

This is the first example of pure rotary data extracted from an oscillating test. The fact that the data from positive and negative roll rates agrees so well is indicative of the quality of the data obtained. Comparison with the static data shows good agreement with some exception at high angles of attack. These differences may indicate that the pure rotary derivatives are affected by the environment in which they are obtained. In this case, they may be affected by the oscillation.

The variations of the combined pure rotational derivatives presented in Figure 24 indicate that the non-dimensional roll rate does not have much influence on the parameter $C_{i_p}\cos\alpha_r + C_{i_r}\sin\alpha_r$.

5.2.3 Pure rotational and mixed derivatives

The variation with angle of attack of the pure rotational characteristics at different sideslip angles obtained from the static tests (VPI&SU curved and rolling flow test sections) are presented in Figure 25 and 26. The methods for obtaining these non-dimensional pure rotational derivatives are derived in Section 3.5 .

Significant effects of non-zero sideslip angles on pure rotational derivatives (C_{y_p} , C_{l_p} , C_{n_p}) can be seen in Figure 25 at angles of attack above 25°. One should be reminded that in the nominal condition, $\beta = 0^{\circ}$, at high angles of attack and with positive roll rate, the nose "sees" a positive sideslip angle. With a negative roll rate, the nose "sees" a negative sideslip angle. These conditions change with changes in the nominal sideslip angles. In particular a negative sideslip position with a positive roll rate would tend to reduce the sideslip angle that the nose "sees" while a positive sideslip with positive roll rate would increase that angle.

From the above observations many of the curves in Figure 25 can be explained. In the $\beta = 0^{\circ}$ condition, a positive

roll rate would cause the asymmetric nose vortex on the starboard side to remain close to the fuselage causing a positive force in the y-direction at the nose. This scenario is verified by noting that C_{y_p} and C_{n_p} are both positive. The rolling moment on the otherhand is strongly negative because the near body vortex is carried across the top of the body by the rolling flow to the opposite side of the vertical tail creating a negative side force on the tail. There is a delicate balance on the nose and tail side forces. At 35° angle of attack they are both strong, but about equal leading to a small net side force, but a large yaw and negative roll moment. At the higher angles of attack, the nose force tends to increase while that at the tail tends to decrease leading to the curves in Figure 25 for $\beta = 0^{\circ}$.

For $\beta = 5^{\circ}$, a positive roll rate increases the sideslip angle that the nose "sees". Under these conditions the side force due to the asymmetric nose vortices is reduced, because the near body vortex tends to roll over the nose to the top. This activity is enhanced by the rolling motion of the flow field. As a result, the effect of this asymmetric vortex is nullified with the dominating forces determined by the mean flow. Under these circumstances, the nose force is negative and that on the tail positive leading to the curves for $\beta = 5^{\circ}$ shown in Figure 25.

For $\beta = -5^{\circ}$, the nose tends to line up with the free stream. Under these conditions, the nose effects are strong, but those at the tail small. The result is a somewhat weaker side force, yaw moment, and roll moment than is seen in the $\beta = 0^{\circ}$ case in Figure 25.

The effects of sideslip on the lateral-directional derivatives with sideslip are shown in Figure 26. Again one should be reminded that in curved flow, in the nominal position, $\beta = 0^{\circ}$, the nose "sees" a negative sideslip angle, and the tail "sees" a positive sideslip angle. In general, one would expect small curvature to cause the upwind-close-body vortex to generate a negative C_{y_r} at the higher angles of attack. However, the curved flow environment carries this same vortex over the body and back into the vertical tail, generating a positive side force on the tail. Apparently this force dominates at the higher angles of attack as indicated by the positive C_{y_r}.

A comparison of the in-phase oscillatory derivatives obtained using forced oscillation test in the VPI&SU curved flow test section ($k_1 = 0.133$) with the lateral directional static rotational derivatives obtained from static tests in the VPI&SU curved and rolling flow test sections in Figure 27 indicates that the unsteady derivatives $(k_1)^2 C_{i_{\dot{p}}}$ can be

negligible for angles of attack from 0° to 45° (see section 5.2.1)

The results of the comparison of out-of-phase and pure rotational derivatives from different tests, are shown in Figures 28 and 29. As can be seen, the unsteady $\dot{\beta}$ contribution is significant in the high angle of attack region.

The effects on the roll rate derivatives are shown in Figure 28 with the unsteady aerodynamic effects showing up at angles of attack above 25°. It is in this same region of angles of attack that the asymmetric nose vortex pattern is found in the nose region. Consequently, the unsteady effects seem to be predominantly associated with the time history of the near-body vortex switching from side to side with its associated effects on the wing and tail lifting surfaces. A slight change in the phase relation associated with the roll angle at which the near-body vortex switches sides during an oscillation test can lead to large differences in the value of these combined derivatives. The pure roll rate derivatives are essentially a zero phase relation, where the near-body vortex is on the same side as the relative sideslip on the nose.

Similar comments can be made with regard to the yaw rate derivatives. Again the large effects of unsteadiness are

apparent at 25° angle of attack and above. The key item to note in both these cases is that at certain conditions the combined derivatives and the pure rotary derivatives have opposite signs. As a result, one might expect that the static stability of the aircraft in these regions might be calculated differently (and incorrectly) if the combined derivatives were used instead of the pure rotary derivatives and unsteady derivatives used separately. Some results regarding such calculations are presented in the next section.

Figures 30 and 31 represent the terms which would arise if higher order stability derivatives were retained. Those represent the second order terms which would occur in the Taylor series representation of the forces and moments. In Chapter II , these terms are assumed to be negligible leading to the completely linearized equations of motion developed there {see Eqns. (26), (29) and Eq. (32)}. The procedures for calculating these so called mixed derivatives are discussed in Section 3.5 . In a well behaved function, the value of these derivatives should be independent of the order in which they are calculated. Here we note that in the high angle of attack region this "smoothness" does not exist leading to differences in the derivatives taken each way.

5.3 ANALYSIS OF FLIGHT SIMULATIONS

As mentioned earlier, the need for reliable theoretical prediction of vehicle motion at high angle of attack requires a better understanding of the complex flow phenomena and its relationship to the characteristics of vehicle motion.

The present section looks at an analytical method for predicting vehicle motions and the effects on these predicted motions due to a change in the aerodynamic modelling methods. The purpose is to show the sensitivity of the resulting motion to the various standard methods of representing out-of-phase oscillating derivatives either by individual unsteady and pure rotary aerodynamic derivatives or with terms combining the unsteady and pure rotational derivatives.

Comparison of mathematical aerodynamic models are made by utilizing the fully coupled linear equations of motion and applying eigenvalue, eigenvector analysis for determining their sensitivity to the various aerodynamic models.

5.3.1 Method of Analysis

It has been shown that application of a linear model to obtain the dynamic stability characteristics of an aircraft is useful in describing the complex motions corresponding to out-of-control flight. This same linear model can also prove useful for demonstrating the influence of aerodynamic parameter variation on stability and consequently helpful in developing and formulating an aerodynamic model which may be applicable to flight conditions involving high angles of attack and non-zero sideslips (Ref. 27).

Some success has been achieved with the linear formulation in that linearly predicted stability derivatives or aerodynamic models lead to valuable insight of the aircraft motions throughout the angle of attack range (Refs. 28,29).

For the linear model, six general differential equations describing vehicle motion and two kinematic relations representing the vehicle orientation are used. The resulting 8-dimensional system with the state vector $\vec{x}_1 = \{ u, w, q, \theta, v, p, r, \phi \}^T$ is shown in Appendix A-1. Upon linearization (Ref. 27), the system is transformed into conventional aircraft variables such that the state is

$$\vec{x}_1 = \{ v, \alpha, q, \theta, \beta, p, r, \phi \}^T \qquad (55)$$

Then, a quasi-nondimensional system is defined such that the state variables have following form

$$\vec{x}_2 = \{ \hat{V}, \alpha, \hat{q}, \theta, \beta, \hat{p}, \hat{r}, \phi \}^T \tag{56}$$

By using the non-dimensional stability data obtained at a particular reference equilibrium point, Equation (3) in Appendix A-2 can be converted to a single linear matrix equation of motion. Conventional eigenvalue and eigenvector analysis applied to the above matrix system yields the system characteristics.

The sensitivity of the system eigenvalues and eigenvectors to variations in the aerodynamic stability derivatives of the system matrix is useful to determine the influence of a change of each stability derivative on the respective eigenvalues and eigenvectors.

Since the sensitivity of the eigenvalues and eigenvectors is determined by taking the derivative of the eigenvalues and eigenvectors with respect to the elements (stability derivatives) of the system matrix, it is possible to calculate the importance of various parameters on system characteristics. Furthermore these derivatives can be used to make a preliminary estimation of the changes in the charac-

teristics of vehicle motion due to changes in the parameters of interest.

The following equation is the derivative of the eigenvalue λ with respect to the parameter α which appears in the element of [E] and [Z] matrices {see Appendix (A-1), Eq. (1)}.

$$\frac{\partial \lambda_i}{\partial \alpha} = \vec{y}_i^T \left(- \lambda_i \frac{\partial [E]}{\partial \alpha} + \frac{\partial [Z]}{\partial \alpha} \right) \vec{x}_i \qquad (57)$$

$$i = 1, 2, 3 \ldots\ldots\ldots n$$

The derivative of the eigenvector is given by

$$\frac{\partial \vec{x}_i}{\partial \alpha} = \sum_{\substack{j=1 \\ j \neq i}}^{n} \frac{1}{(\lambda_i - \lambda_j)} \vec{y}_j^T \left(\lambda_i \frac{\partial [E]}{\partial \alpha} - \frac{\partial [Z]}{\partial \alpha} \right) \vec{x}_i (\vec{x}_j - x_j^k \vec{x}_i) \qquad (58)$$

$$i = 1, 2, 3 \ldots\ldots\ldots n$$

where k corresponds to the element of $\vec{x}_i$ which equals unity, i.e. , $x_i^k = 1$, and $\vec{y}_i$s are components of the left eigenvector.

Detailed methods for calculating the derivatives of the eigenvalues and eigenvectors are presented in Appendix A-3 (Refs. 30,31,32).

5.3.2 Results of Dynamic Stability Calculations

The results of lateral dynamic stability calculations using two different sets of data were compared. One is the "unsteady" model which accounts for $C_{i_{\dot{\beta}}}$ separated by subtracting the pure rotary derivatives from the forced oscillation data. The other is the "combined" model where the out-of-phase oscillatory derivatives are taken to be equal to the pure rotary derivatives such that,

$$C_{i_p} + C_{i_{\dot{\beta}}} \sin\alpha_r \longrightarrow C_{i_p} \tag{59}$$

$$C_{i_r} - C_{i_{\dot{\beta}}} \cos\alpha_r \longrightarrow C_{i_r} \tag{60}$$

Table 12 shows the geometric, mass and inertial properties of the aircraft and the flight parameters used as reference flight conditions about which a linearized analysis was performed. The lateral dynamic stability input data for both models are shown in Table 13.

The dynamic stability characteristics of the lateral directional modes of motion are calculated for the "unsteady" and "combined" models. Table 14 represents the period T and time to half-amplitude ($t_{1/2}$) of the Dutch roll mode and time to half-amplitude of the rolling convergence and spiral modes for each of the models.

The variation with angle of attack of the damping characteristics ($1/t_{1/2}$) of various modes of motion for different models are graphically demonstrated in Figure 32. Positive values of $1/t_{1/2}$ represent damped (dynamically stable) while negative values represent negatively damped (dynamically unstable) modes.

For a straight and level flight reference condition with equilibrium angles of attack from 30° through 43° (unsteady model) or 23° through 43° (combined model), the Dutch roll mode is unstable. The onset of lateral instability suggests directional divergence near 31° for the unsteady model which corresponds well with flight tests (Ref. 25).

The rolling convergence and spiral modes of motion for unsteady aerodynamic model remain stable over the range of angles of attack with the exception of rolling convergence for angles of attack above 35 degrees. The unstable rolling convergence mode indicated by the calculations for the unsteady aerodynamic model has been evident in flight test results (Fig. 33). This Figure shows that the roll rate enters into large amplitude oscillations above 35° angle of attack (Ref. 33).

The unstable spiral mode for combined aerodynamic model at angles of attack between 27° to 37° does not agree with

the flight test result, demonstrating the earlier assertion that this model is not reliable as a pre-indicator of vehicle characteristics at high angles of attack.

The relative magnitude and phase relationships of the β, ϕ, ψ and p in Table 15 indicate the general nature of the lateral oscillation. The data indicate that the magnitude of ϕ component is relatively larger than other components throughout the angle of attack range especially at angles of attack from 25° to 35°, thereby indicating that the Dutch roll becomes predominantly a rolling motion about the longitudinal axis. As angle of attack is increased, the phase relationship of β/ϕ becomes more in phase and β/p becomes more out-of-phase.

Comparison of the computation results (magnitude and phase relationship for Dutch roll mode, Table 15) of the unsteady and combined aerodynamic data indicates that both models are in good agreement and shows the combined aerodynamic model yields the basic trends of the dynamic characteristics. For vehicle motion with large values of sideslips and angular velocities such as incipient spin and oscillatory spin motions, the acceleration derivatives must be employed (unsteady aerodynamic model) to simulate more accurately the stability characteristics of the Dutch roll mode (Ref. 27).

In order to investigate the dynamic stability characteristics of the vehicle motion, it is desirable to study the sensitivity of the eigendata to changes in system parameters (stability derivatives). The results and input parameter variations presented in Table 16 show that the exact values on eigendata and computed values are in good agreement.

Eigendata sensitivity comparisons for unsteady and combined model are made throughout the angle of attack range from 0° to 45° . At lower angles of attack, the results of two models are in good agreement for 6 different eigendata, $\partial\lambda/\partial C_{y_\beta}$, $\partial\lambda/\partial C_{l_\beta}$, $\partial\lambda/\partial C_{n_\beta}$, $\partial\lambda/\partial C_{y_p}$, $\partial\lambda/\partial C_{l_p}$ and $\partial\lambda/\partial C_{n_p}$. As shown in Table 17, the $\partial\lambda/\partial C_{l_\beta}$ and $\partial\lambda/\partial C_{n_\beta}$ data between two models are significantly different at the higher angles of attack. The key observation here is that in the angle of attack ranges from 35 to 45 degrees the sensitivity of the real part of the eigenvalue to changes in C_{l_β} and C_{n_β} are different in sign. Hence the effect of these parameters on stability is the opposite, depending upon the aerodynamic model used.

Chapter VI

SUMMARY AND CONCLUSIONS

The capabilities of the VPI&SU Stability Wind Tunnel have been expanded in this study. In particular a roll oscillatory rig was designed and constructed to be compatible with the existing curved and rolling flow test sections. The rig permits one to oscillate an aircraft model about its longitudinal axis while immersed in a straight, curved or rolling flow air stream allowing new and unique flight conditions to be examined systematically.

In order to make use of this facility the general equations of motion of a model constrained to operate under specified motions in a non uniform stream were developed. The method of their development was different than that usually found in the literature in that they were obtained by considering special cases of the general equations of an aircraft in flight in the presence of a moving atmosphere. As a result the equations developed are rigorous. The particular conditions of interest here were for specified sinusoidal roll oscillation about the vehicle longitudinal or roll axis in the presence of curved flow (about the z horizontal axis) or in the presence of rolling flow (about the x horizontal axis). Additional equations of motion were developed

for the case of lateral translational oscillation of the model in the same non uniform flow conditions. Although not used in this research, these latter equations would serve as a basis for including sway in the prescribed model motion. This sway motion could be due to the flexibility of the support or an additional prescribed motion. In general these equations could be used to determine new forced or free oscillation tests in various combinations of motions and flow environments to extract particular aerodynamic stability derivatives. They can also be used for the purpose of aiding in the development of parameter estimation techniques and the shaping of compatible experiments to be used in wind tunnel testing.

A model of an F-5 aircraft was used in conjunction with the roll oscillation rig and tested in the curved and rolling flow test section. Static and roll oscillatory tests were carried out in a straight, curved, and rolling flow environment at various angles of attack and sideslip angles. The results are presented in terms of graphs and charts showing comparisons of lateral-directional stability parameters at various angles of attack, sideslip, yaw rate and roll rate.

In addition the aerodynamic stability derivative information was used to develop two aerodynamic models. These in turn were used in a full set of linearized equations of motion for the purpose of predicting aircraft motion at high angles of attack. The validity of the two different aerodynamic models for predicting motions was examined by comparing the predicted motions with actual flight test data. In addition an eigenvalue and eigenvector analysis was performed on the linear system using each of the aerodynamic models, and a sensitivity of these parameters examined with respect to changes in the lateral-directional static stability derivatives.

In examining the results of the above activities, the following observations and conclusions can be made.

1. Static lateral-directional stability is affected by the curvature and roll rate variations at angles of attack above that for wing stall ($\alpha = 17^{o}$).

2. Pure rotary derivatives obtained from static test and dynamic test show that they are in good agreement up to 30 degrees angles of attack. Differences among the data are observed at higher angles of attack.

3. The in-phase oscillatory derivatives have similar values to those of pure rotary derivatives throughout the angles of attack ($\alpha = 0^{\circ}$ to 45°) such that

$$C_{i_\beta} \sin\alpha_r - (k_1)^2 C_{i_{\dot{p}}} = C_{i_\beta} \sin\alpha_r$$

4. The out-of-phase oscillatory derivatives become small either positively or negatively at higher angles of attack ($\alpha > 25^{\circ}$) with increasing frequency of oscillation.

5. The unsteady lateral translational derivatives, C_{i_β} contribute significantly to the out-of-phase oscillatory derivatives at higher angles of attack.

6. Differences are shown in the mixed derivatives ($C_{i_{\beta p}}$ and $C_{i_{p\beta}}$, $C_{i_{\beta r}}$ and $C_{i_{r\beta}}$) at higher angles of attack ($\alpha > 25^{\circ}$).

7. Compared to the "combined" aerodynamic model which assigns forced oscillation data to the pure rotary derivatives, the "unsteady" aerodynamic model data yields better agreement with the full-scale flight test results at high angles of attack

8. Eigendata, along with the sensitivity analysis of the fully-coupled linearized equations of motion using the two aerodynamic models indicate that at certain flight condi-

tions the two models give opposite results with regard to stability and with regard to changes in stability due to changes in selected stability parameters.

From the above results, two main features can be observed. The first is that the VPI&SU SWT facility allows the gathering of extensive data in a wide variety of test environments. Here the effects of rotary motion on the normal static stability derivatives are easily obtained. Further, the combination of test environments allows certain combined derivatives obtained from oscillatory testing to be separated, and the individual properties observed. In addition all this information is obtained with the same tunnel, model and data acquisition system, and hence comparisons can be made directly.

The second feature to note is that the predicted dynamic behavior at certain flight conditions is significantly different depending upon the aerodynamic model used. Further there is indication that the so-called unsteady aerodynamic model gives results which are closer to those obtained from flight tests. In addition the effect of changing the usual static stability derivatives on the dynamic stability of the aircraft at certain flight conditions depends upon which aerodynamic model is used.

In conclusion, there is evidence that in order to adequatly determine an aircraft aerodynamic model from which to faithfully predict or simulate aircraft motions, a complete set of wind tunnel tests is required so that the unsteady aerodynamic model can be determined. Currently the most convenient method of obtaining this data is in the VPI&SU Stability Wind Tunnel.

REFERENCES

1. P. R. Kurzhals, "Systems Implications of Active Controls", AGARD CP-260, Paper 1, May 1979.

2. J. K. Ramage, J. W. Morris, "Design Considerations for Reliable FBW Flight Control", AGARD CP-260, Paper 15, May 1979.

3. J. M. DUC, "Control Configured Vehicle Design Philosophy", AGARDograph No. 234, Paper 1, May 1978.

4. B.R.A. Burns, "Control Configured Combat Aircraft", AGARDograph No. 234, Paper 3, May 1978.

5. K. J. Orlik-Ruckemann, "Aerodynamic Aspects of Aircraft Dynamics of High Angle of Attack", AIAA 9th Atmospheric Flight Mechanics Conference, Aug. 1982.

6. C, J. Schueler, L.K. Ward, A. E. Hodapp,Jr, "Techniques for Measurement of Dynamic Stability Derivatives in Ground Test Facilities", AGARDgraph 121, Oct. 1967.

7. K. J. Orlik-Ruckemann, "Techniques for Dynamic Stability Testing in Wind Tunnels", AGARD CP-235, Paper 1, Nov. 1978.

8. G. N. Malcolm, "Rotary and Magnus Balances", AGARD LS-114, Paper 6, May 1981.

9. F.H. Lutze, "Curved Flow Wind Tunnel Test of A Spin-Resistent Aircraft Configuration", VPI Aero-067, Aug. 1977.

10. F.H. Lutze, "Curved Flow Wind Tunnel Test of F-18 Aircrafs", VPI Aero-108, Apr. 1980.

11. F.H. Lutze, "Rolling Flow Wind Tunnel Test of A Spin-Resistent Aircraft Configuration", VPI Aero-075, Dec. 1977.

12. F.H. Lutze, "Rolling Flow Wind Tunnel Test of F-18 Aircraft", VPI Aero-109, May 1980.

13. M. Tobak, L. B. Schiff, "On the Formulation of the Aerodynamic Chracteristics in Aircraft Dynamics", NASA TR R-456, Jan. 1976.

14. C. E. Steidle, "Analysis and Application of Curved and Rolling Flow Wind Tunnel Testing", Master's Thesis, VPI&SU, Dec. 1979.

15. K. J. Orlik-Ruckemann, E. S. Hanff, "Experiments on Cross-Coupling and Translational Accerelation Derivatives", AGARD CP-235, Paper 8, Nov. 1978.

16. M. J. Queijo, S. Fletcher, C. G. Marple, F. M. Huges, "Preliminary Measurements of Aerodynamic Yawing Derivatives of a Triangular, a Swept, and an Unswept Wing Performing Pure Yawing Oscillations", NASA RM-L55L14, 1955.

17. J. S. Ko, "Analysis of Various Forced Oscillaton Techniques for Obtaining Dynamic Stability Derivatives", Master's Thesis, VPI&SU, July 1982.

18. J. R. Chambers, S. B. Grafton, "Aerodynamic Chracteristics of Airplanes at High Angles of Attack", NASA TM-74097, Dec. 1977.

19. B. Etkin, "Dynamics of Atmospheric Flight", John Wiley & Sons, 1972.

20. C. D. Perkins, R. E. Hage, "Airplane Performance Stability and Control", John Wiley & Sons, 1949.

21. J. Roskam, "Airplane Flight Dynamics and Automatic Flight Controls I, II", Roskam Aviation and Engineering Corporation, 1979.

22. J. Sanford, "Lateral-Longitudinal Cross-Coupling Effects", Aerodynamic Inputs for Problems in Aircraft Dynamics, Von Karman Institute for Fluid Dynamic Lecture Series 99 Vol 1, Apr. 1977.

23. F. H. Lutze, E. M. Cliff, "New Calibration and Corrections for the VPI&SU Stability Wind Tunnel Curved Flow Test Section", VPI Aero-069, Aug. 1977.

24. F. H. Lutze, "Calibration of the VPI&SU Stability Wind Tunnel Rolling Flow Test Section", VPI Aero-070, Aug. 1977.

25. S. B. Grafton, J. R. Chambers, P. L. Coe, Jr. , "Wind Tunnel Free Flight Investigation of a Model of a Spin-Resistent Fighter Configuration, NASA TN D-7716, June 1974.

26. A. Pope, J. Harper , "Low Speed Wind Tunnel Testing", John Wiley & Sons, 1966.

27. M. H. Hreha, "Linear Analysis of Incipient Spin Dynamics", Master's Thesis, VPI&SU, June 1979.

28. F. C. Haus, "Stability of Helicoidal Motions at High Incidence", AGARD CP-199, Paper 9, June 1976.

29. J. R. Chambers, E. L. Anglin, "Analysis of Lateral-Directional Stability Characteristics of a Twin-Jet Fighter Airplane at High Angles of Attack", NASA TN D-5361, June 1969.

30. L. C. Rogers, "Derivatives of Eigenvalues and Eigenvectors", AIAA Journal, Vol 8, No 5, pp 943-944, May 1970.

31. R. B. Nelson, "Simplified Calculation of Eigenvector Derivatives", AIAA Journal, Vol 14, No 9, pp 1201-1205, Sep 1976.

32. J. W. Crane, "Design of an Adaptive Control System for the EBF/STOL Aircraft with Provisions for Eigenvalue and Eigenvector Selection", Ph.D. Dissertation, VPI&SU, Feb, 1980.

33. L. E. Arent, "F-5E Spin Susceptibility Test Program", The Many Displines of Flight Test, Proc. of 7th Annual Symposium, Eastsound Orcas Island, Wash, Aug 4-6, 1976, Society of Flight Test Engrs 1976, pp 29-1 to 29-17.

Table 1. Wind Tunnel Methods of Measurement of Dynamic Chracteristics(Ref. 7).

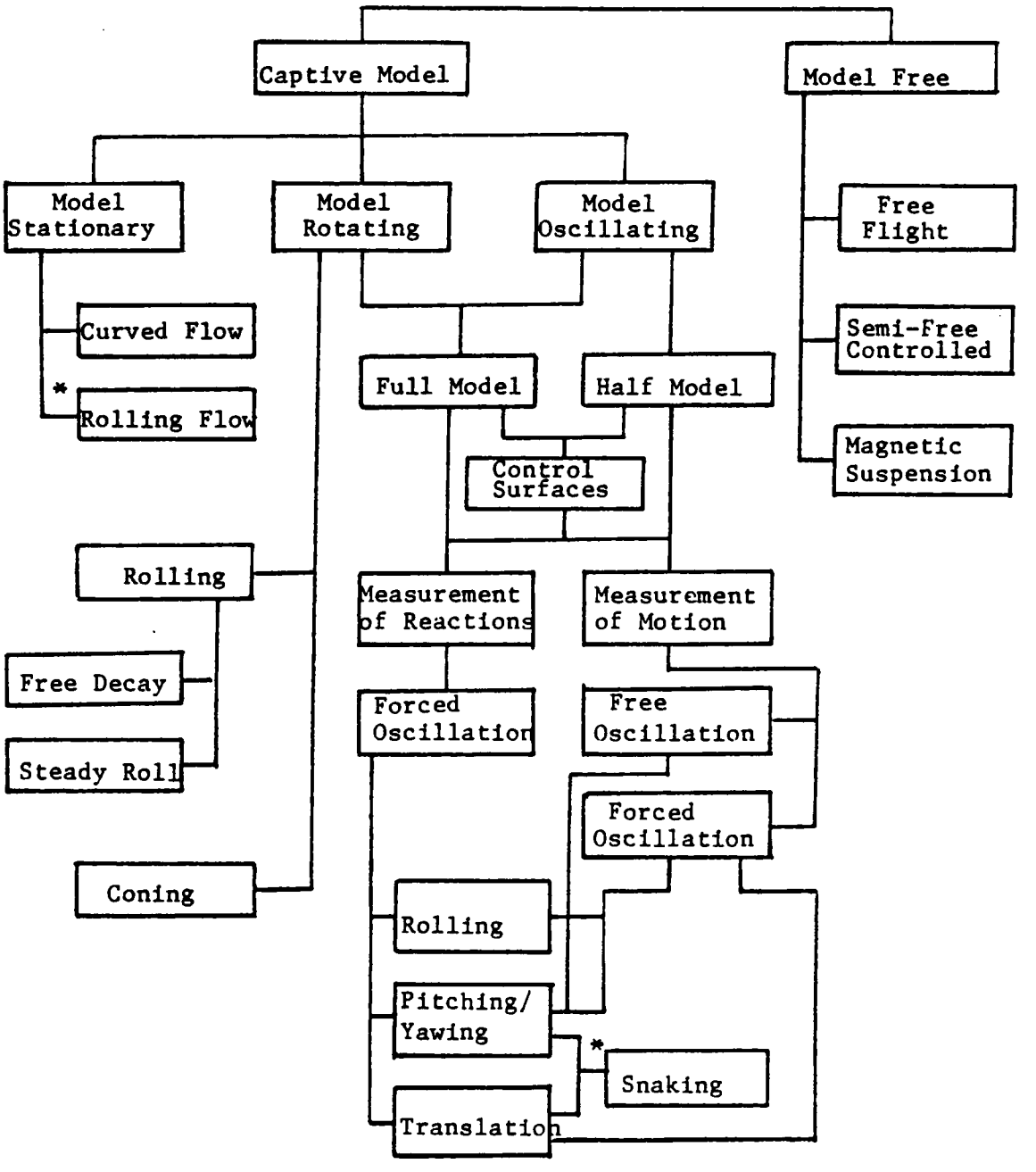

* are additioned to the original reference

Table 2. Dynamic Derivatives.

Dynamic Force Derivatives

Pure Rotation	Translational Acceleration	Oscillation around Fixed Axis	
		Damping Derivatives	Cross-Coupling Derivatives
C_{x_p} C_{y_p} C_{z_p}	$C_{x_{\dot{\alpha}}}$ $C_{y_{\dot{\alpha}}}$ $C_{z_{\dot{\alpha}}}$	$C_{x_q}+C_{x_{\dot{\alpha}}}$	$C_{x_p}+C_{x_{\dot{\beta}}}\sin\alpha_r$
C_{x_q} C_{y_q} C_{z_q}	$C_{x_{\dot{\beta}}}$ $C_{y_{\dot{\beta}}}$ $C_{z_{\dot{\beta}}}$	$C_{y_p}+C_{y_{\dot{\beta}}}\sin\alpha_r$	$C_{x_r}-C_{x_{\dot{\beta}}}\cos\alpha_r$ $C_{y_q}+C_{y_{\dot{\alpha}}}$
C_{x_r} C_{y_r} C_{z_r}		$C_{y_r}-C_{y_{\dot{\beta}}}\cos\alpha_r$ $C_{z_q}+C_{z_{\dot{\alpha}}}$	$C_{z_p}+C_{z_{\dot{\beta}}}\sin\alpha_r$ $C_{z_r}-C_{z_{\dot{\beta}}}\cos\alpha_r$

Dynamic Moment Derivatives (Ref. 7).

Pure Rotation	Translational Acceleration	Oscillation around Fixed Axis		
		Damping Derivatives	Cross Derivatives	Cross-Coupling Derivatives
C_{l_p} C_{m_p} C_{n_p}	$C_{l_{\dot{\alpha}}}$ $C_{m_{\dot{\alpha}}}$ $C_{n_{\dot{\alpha}}}$	$C_{l_p}+C_{l_{\dot{\beta}}}\sin\alpha_r$	$C_{l_r}-C_{l_{\dot{\beta}}}\cos\alpha_r$	$C_{l_q}+C_{l_{\dot{\alpha}}}$
C_{l_q} C_{m_q} C_{n_q}	$C_{l_{\dot{\beta}}}$ $C_{m_{\dot{\beta}}}$ $C_{n_{\dot{\beta}}}$	$C_{m_q}+C_{m_{\dot{\alpha}}}$		$C_{m_r}-C_{m_{\dot{\beta}}}\cos\alpha_r$ $C_{m_p}+C_{m_{\dot{\beta}}}\sin\alpha_r$
C_{l_r} C_{m_r} C_{n_r}		$C_{n_r}-C_{n_{\dot{\beta}}}\cos\alpha_r$	$C_{n_p}+C_{n_{\dot{\beta}}}\sin\alpha_r$	$C_{n_q}+C_{n_{\dot{\alpha}}}$

Table 3. Oscillatory Derivatives Obtained by Employing Forced Oscillation about the Body Axis (Prescribed Displacement).

In-Phase	Out-of-Phase
Pitching Setup	
$C_{x_\alpha}-(k_2)^2C_{x_{\dot{q}}}$	$C_{x_q}+C_{x_{\dot{\alpha}}}$
$C_{y_\alpha}-(k_2)^2C_{y_{\dot{q}}}$	$C_{y_q}+C_{y_{\dot{\alpha}}}$
$C_{z_\alpha}-(k_2)^2C_{z_{\dot{q}}}$	$C_{z_q}+C_{z_{\dot{\alpha}}}$
$C_{l_\alpha}-(k_2)^2C_{l_{\dot{q}}}$	$C_{l_q}+C_{l_{\dot{\alpha}}}$
$C_{m_\alpha}-(k_2)^2C_{m_{\dot{q}}}$	$C_{m_q}+C_{m_{\dot{\alpha}}}$
$C_{n_\alpha}-(k_2)^2C_{n_{\dot{q}}}$	$C_{n_q}+C_{n_{\dot{\alpha}}}$
Rolling Setup	
$C_{x_\beta}\sin\alpha_r-(k_1)^2C_{x_{\dot{p}}}$	$C_{x_p}+C_{x_{\dot{\beta}}}\sin\alpha_r$
$C_{y_\beta}\sin\alpha_r-(k_1)^2C_{y_{\dot{p}}}$	$C_{y_p}+C_{y_{\dot{\beta}}}\sin\alpha_r$
$C_{z_\beta}\sin\alpha_r-(k_1)^2C_{z_{\dot{p}}}$	$C_{z_p}+C_{z_{\dot{\beta}}}\sin\alpha_r$
$C_{l_\beta}\sin\alpha_r-(k_1)^2C_{l_{\dot{p}}}$	$C_{l_p}+C_{l_{\dot{\beta}}}\sin\alpha_r$
$C_{m_\beta}\sin\alpha_r-(k_1)^2C_{m_{\dot{p}}}$	$C_{m_p}+C_{m_{\dot{\beta}}}\sin\alpha_r$
$C_{n_\beta}\sin\alpha_r-(k_1)^2C_{n_{\dot{p}}}$	$C_{n_p}+C_{n_{\dot{\beta}}}\sin\alpha_r$
Yawing Setup	
$C_{x_\beta}\cos\alpha_r+(k_1)^2C_{x_{\dot{r}}}$	$C_{x_r}-C_{x_{\dot{\beta}}}\cos\alpha_r$
$C_{y_\beta}\cos\alpha_r+(k_1)^2C_{y_{\dot{r}}}$	$C_{y_r}-C_{y_{\dot{\beta}}}\cos\alpha_r$
$C_{z_\beta}\cos\alpha_r+(k_1)^2C_{z_{\dot{r}}}$	$C_{z_r}-C_{z_{\dot{\beta}}}\cos\alpha_r$
$C_{l_\beta}\cos\alpha_r+(k_1)^2C_{l_{\dot{r}}}$	$C_{l_r}-C_{l_{\dot{\beta}}}\cos\alpha_r$
$C_{m_\beta}\cos\alpha_r+(k_1)^2C_{m_{\dot{r}}}$	$C_{m_r}-C_{m_{\dot{\beta}}}\cos\alpha_r$
$C_{n_\beta}\cos\alpha_r+(k_1)^2C_{n_{\dot{r}}}$	$C_{n_r}-C_{n_{\dot{\beta}}}\cos\alpha_r$

Table 4. Combined Damping Derivatives Obtained by Employing Forced Oscillation with a Curved/Rolling Flow.

Pitch, Rolling and Yawing Setup

Oscillation (Curved Flow)	Oscillation (Rolling Flow)
$Cx_p \sin\alpha_r - Cx_r \cos\alpha_r$	$Cx_p \cos\alpha_r + Cx_r \sin\alpha_r$
$Cy_p \sin\alpha_r - Cy_r \cos\alpha_r$	$Cy_p \cos\alpha_r + Cy_r \sin\alpha_r$
$Cz_p \sin\alpha_r - Cz_r \cos\alpha_r$	$Cz_p \cos\alpha_r + Cz_r \sin\alpha_r$
$Cl_p \sin\alpha_r - Cl_r \cos\alpha_r$	$Cl_p \cos\alpha_r + Cl_r \sin\alpha_r$
$Cm_p \sin\alpha_r - Cm_r \cos\alpha_r$	$Cm_p \cos\alpha_r + Cm_r \sin\alpha_r$
$Cn_p \sin\alpha_r - Cn_r \cos\alpha_r$	$Cn_p \cos\alpha_r + Cn_r \sin\alpha_r$

Table 5. Amplitude and Frequency Characteristics in Roll Oscillatory Rig (VPI&SU).

Amplitude of Roll Oscillation

Flywheel Roller Position (in)	Maxmum Amplitude Angle (deg.)
2.50	+ 22.6
2.25	+ 20.3
2.00	+ 17.9
1.75	+ 15.6
1.50	+ 13.3
1.25	+ 11.1
1.00	+ 8.9
0.75	+ 6.6
0.50	+ 4.4

Frequency of Roll Oscillation

Oscillation Frequency (Hz.)	* Reduced Frequency ($\omega b/2V$)
0.3	0.020
0.5	0.033
0.7	0.094
1.0	0.066
1.5	0.099
2.0	0.132
2.5	0.165
3.0	0.198

* Based on b = 2.525 ft. , V = 120 ft/sec

Table 6. Balance Characteristics and Calibration Data.

Balance Characteristics (Langley FF09C)

Moment center (from front of balance) ..... 2 inch

Balance input voltage ..... 5 volts

Balance Calibration Data

Component	Load Limit (lb or in-lb)	Balance Constant (lb/mvolt, ft-lb/mvolt)
Normal Force	100.0	25.314
Axial Force	50.0	10.873
Pitching Moment	480.0	7.195
Rolling Moment	176.8	2.813
Yawing Moment	540.0	8.300
Side Force	60.0	15.705

Table 7. Geometric Properties of Model.

Reference Geometry	
Wing Span	$b = 0.770$ m (2.525 ft)
Wing Area	$S = 0.161$ m^2 (1.734 ft^2)
Mean Aerodynamic Chord	$\bar{c} = 0.235$ m (0.771 ft)
Volumes	
Fuselage (including nose)	1.324×10^{-2} m^3 (808.1 in^3)
Nose only	2.155×10^{-3} m^3 (131.5 in^3)
Wings	8.439×10^{-4} m^3 (51.5 in^3)
Horizontal Tail	1.180×10^{-4} m^3 (7.2 in^3)
Vertical Tail	1.704×10^{-4} m^3 (10.4 in^3)
Full Configuration	1.437×10^{-2} m^3 (877.2 in^3)

Table 7. Geometric Properties of Model (concluded).

Areas		
	Top View	Front View
Fuselage (including nose)	1.651×10^{-1} m^2 (255.88 in^2)	1.875×10^{-2} m^2 (29.06 in^2)
Nose Only	3.402×10^{-2} m^2 (52.74 in^2)	1.057×10^{-2} m^2 (16.38 in^2)
Wings	1.108×10^{-1} m^2 (171.76 in^2)	5.181×10^{-3} m^2 (8.03 in^2)
Horizontal Tail	3.057×10^{-2} m^2 (47.38 in^2)	1.329×10^{-3} m^2 (2.06 in^2)
Vertical Tail	- - - - -	9.677×10^{-4} m^2 (1.50 in^2)
Full Configuration	3.065×10^{-1} m^2 (475.02 in^2)	2.622×10^{-2} m^2 (40.65 in^2)

Areas	
	Side View
Fuselage (including nose)	1.250×10^{-1} m^2 (193.74 in^2)
Nose Only	2.939×10^{-2} m^2 (45.55 in^2)
Wings	- - - - -
Horizontal Tail	- - - - -
Vertical Tail	3.472×10^{-2} m^2 (53.82 in^2)
Full Configuration	1.597×10^{-1} m^2 (247.56 in^2)

Table 8. Data Acquisition Block Diagram, VPI&SU.

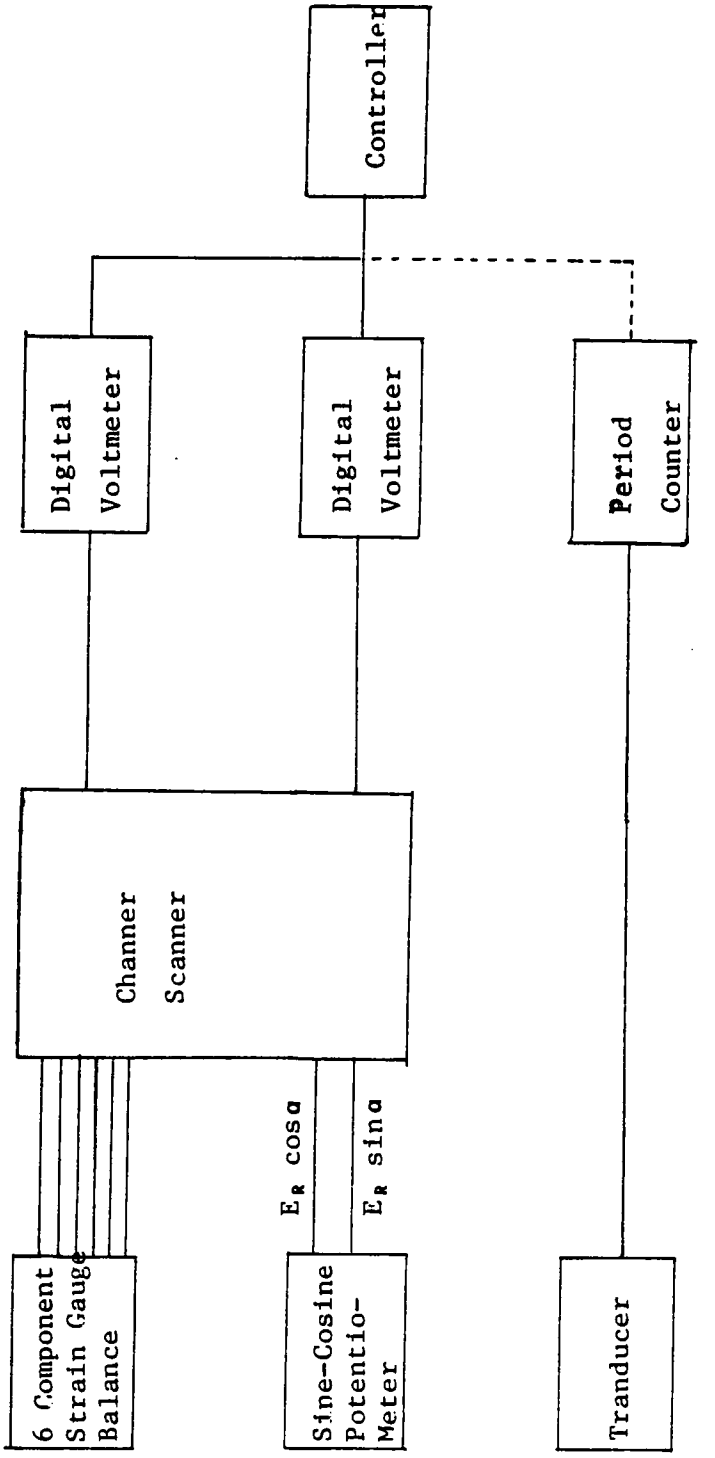

Table 9. Simplified Block Diagram of Dynamic Test Data Reduction .

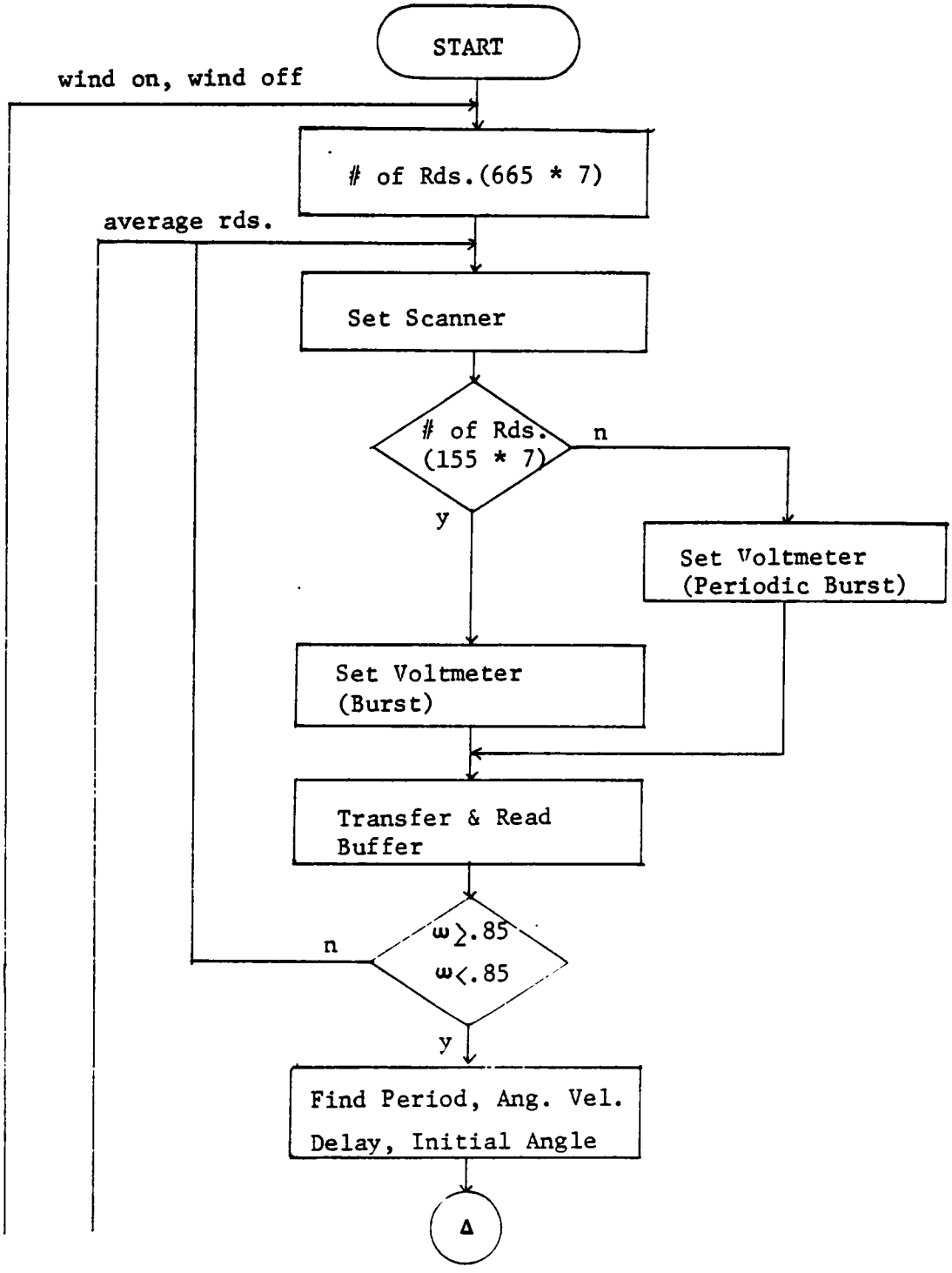

Table 9. Simplified Block Diagram of Dynamic Test Data Reduction (concluded).

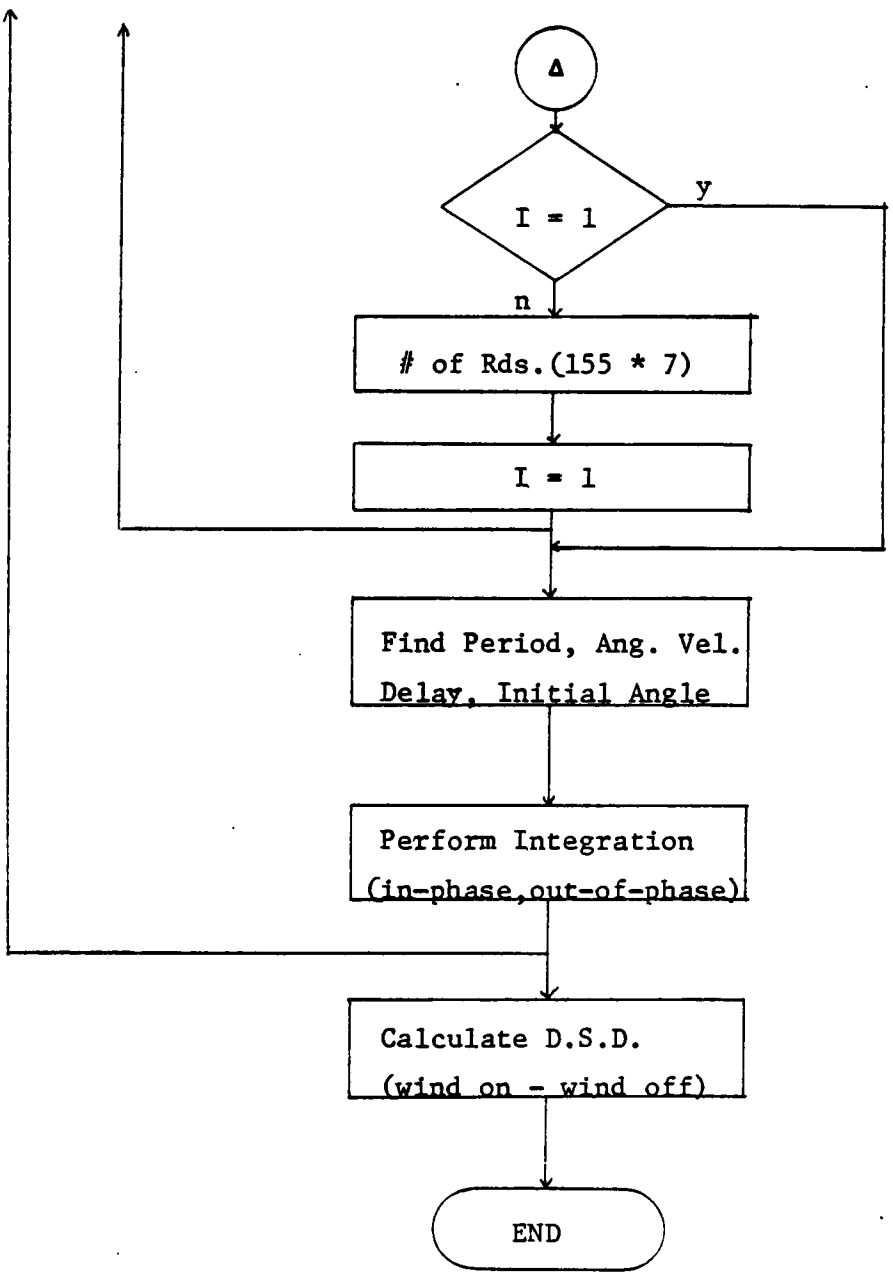

Table 10. Relationship of the Oscillation Frequency and Sampling Data (VPI&SU).

Parameter / Mode	Frequency (Hz.)	# of Readings		b Delay/NRDS (msec)
		a NRDS/Cycle	NRDS/Sec	
Burst Readings	3	49	143	7
	2	72	143	7
	1.5	96	143	7
	1.0	143	143	7
Periodic Burst Readings	0.6	143	86	12
	0.4	143	58	17
	0.3	143	43	23

a NRDS denotes number of readings

b Delay/NRDS denotes time interval between first and next sampling readings (sine fn. and 6 reaction signals)

Table 11. Mass and Geometric Characteristics of the Basic Wing Model Configuration (Ref. 25).

Model weight	251.3 N (56.5 lb)
Model moment of inertia	
I_X	0.56 kg-m² (0.41 slug-ft²)
I_Y	8.53 kg-m² (6.29 slug-ft²)
I_Z	8.95 kg-m² (6.60 slug-ft²)
Wing	
Span	1.34 m (4.39 ft)
Area	0.49 m²(5.24 ft²)
Root chord	0.59 m (1.95 ft)
Tip chord	0.15 m (0.48 ft)
Mean aerodynamic chord	0.41 m (1.34 ft)
Aspect ratio	3.68
Taper ratio	0.25
Dihedral	0
Aileron area (one side)	0.013 m²(0.14 ft²)
Horizontal tail	
Area	0.165 m²(1.78 ft²)
Span	0.75 m (2.46 ft)
Aspect ratio (exposed)	2.88
Taper ratio	0.33
Dihedral	-4.0
Vertical tail	
Area (exposed)	0.12 m²(1.25 ft²)
Aspect ratio (exposed)	1.22
Taper ratio (exposed)	0.25
Rudder area (aft of hinge)	0.017 m²(0.18 ft²)
Overall fuselage length	2.38 m (7.81 ft)

Table 12. Equilibrium Flight Trajectories .

Geometric, mass and inertia characteristics

Chord	7.73 ft
Span	25.25 ft
Area	170 ft^2
Mass	312 slug
I_x	1700 (slug-ft^2)
I_Y	29500 (slug-ft^2)
I_z	30100 (slug-ft^2)

Flight parameters

α	0 - 45 (deg)
$\overline{q}$	43.1825 (lb/ft^2)
V	384 (ft/sec)
Mach #	.3955
h	36000 (ft)

Table 13. Dynamic Stability Input Data.

α (deg)	model	C_{y_p}	C_{l_p}	C_{n_p}	C_{y_r}	C_{l_r}	C_{n_r}	$C_{y_{\dot{\beta}}}$	$C_{l_{\dot{\beta}}}$	$C_{n_{\dot{\beta}}}$
0	unsteady	-0.028	-0.369	0.020	1.876	0.095	-0.730	0.288	0.018	-0.110
	combined	0.00	-0.03	0.05	1.30	0.06	-0.51	-	-	-
5	unsteady	0.123	-0.338	-0.054	1.796	0.138	-0.742	1.166	0.129	0.027
	combined	0.30	-0.32	-0.03	1.50	0.09	-0.52	-	-	-
10	unsteady	0.125	-0.254	-0.001	1.691	0.113	-0.672	-0.312	0.135	-0.082
	combined	0.00	-0.20	-0.01	1.60	0.15	-0.56	-	-	-
15	unsteady	0.238	-0.091	-0.035	1.674	0.022	-0.826	0.365	-0.202	-0.150
	combined	0.30	-0.14	-0.06	1.20	0.23	-0.61	-	-	-
20	unsteady	0.130	-0.078	-0.128	1.975	-0.058	-0.522	0.647	-0.183	0.097
	combined	0.40	-0.08	-0.17	1.50	0.28	-0.82	-	-	-
25	unsteady	-0.081	-0.085	-0.106	2.379	-0.087	-0.415	1.216	-0.022	-0.085
	combined	0.35	-0.03	-0.18	1.10	0.07	-0.42	-	-	-
30	unsteady	0.774	-0.242	0.159	0.681	-0.077	-0.326	-1.678	0.340	-0.773
	combined	-0.20	0.05	-0.27	1.90	-0.16	0.27	-	-	-
35	unsteady	-1.009	-0.651	0.860	3.671	0.130	-0.265	-0.994	1.455	-2.081
	combined	-2.20	0.57	-0.88	3.60	-0.51	0.66	-	-	-
40	unsteady	1.445	-0.416	0.656	4.269	0.282	0.374	-5.195	0.967	-1.713
	combined	-4.20	0.38	-0.87	5.50	-0.25	1.18	-	-	-
45	unsteady	0.794	-0.327	0.794	3.431	0.537	0.976	-3.990	0.265	-1/618
	combined	-3.80	-0.23	-0.92	4.50	0.26	1.55	-	-	-

Table 14. Calculated Lateral Dynamic Stability Characteristics.

model / mode / para. / α (deg)	unsteady model				combined model			
	dutch roll		roll	sprial	dutch roll		roll	sprial
	$t_{1/2}$	T	$t_{1/2}$	$t_{1/2}$	$t_{1/2}$	T	$t_{1/2}$	$t_{1/2}$
0	26.25	4.79	.48	67.96	69.31	4.81	.57	68.63
5	7.00	3.92	.59	40.77	7.30	3.92	.62	55.01
10	4.56	3.06	1.03	19.04	4.81	3.03	1.18	28.88
15	4.68	2.92	2.02	8.68	4.72	2.93	1.68	-49.51
20	4.68	2.71	2.10	11.73	9.76	2.70	2.04	23.50
25	12.38	3.69	2.75	13.18	-7.15	3.61	2.26	15.75
30	57.76	1.93	[b] 9.78	[b] 9.78	-3.40	1.92	3.14	-12.10
35	[a] -1.39	1.46	[c] 39.16	[c] 39.16	-.58	1.47	3.19	-10.44
40	-1.27	2.00	-4.70	5.37	-.84	2.00	[d] 9.04	[d] 9.04
45	3.32	2.21	-1.29	5.18	2.69	2.22	-2.28	3.00

a negative values of $t_{1/2}$ indicate instability

b,c,d are combined modes

Table 15. Relative Magnitudes and Phase Relationships of the Dutch Roll Mode.

mode / para / α (deg)	unsteady model						combined model					
	magnitude			phase angle (deg)			magnitude			phase angle (deg)		
	β/Φ	β/P	β/ψ	β/Φ	β/P	β/ψ	β/Φ	β/P	β/ψ	β/Φ	β/P	β/ψ
0	.44	.33	1.11	312.9	221.8	176.6	.40	.30	1.11	318.3	227.9	175.3
5	.29	.18	1.52	329.4	236.4	183.1	.29	.18	1.53	327.8	234.9	184.0
10	.29	.14	2.58	346.0	252.2	185.9	.29	.14	2.61	346.5	252.9	185.3
15	.43	.19	2.62	350.3	257.1	186.9	.43	.19	2.61	350.5	257.3	186.6
20	.44	.18	4.69	353.5	260.3	189.4	.44	.18	4.68	353.7	262.5	186.6
25	.38	.13	8.63	321.3	260.8	337.5	.39	.23	8.76	350.8	264.6	319.3
30	.52	.16	24.14	353.8	266.1	224.0	.52	.16	22.33	355.8	269.9	221.4
35	.62	.14	15.11	356.7	273.8	193.5	.63	.14	12.24	355.5	282.0	203.2
40	.82	.23	6.02	356.7	276.9	179.5	.82	.23	5.98	356.4	281.6	180.7
45	1.25	.21	2.74	336.9	256.1	200.8	1.21	.32	2.54	330.5	252.6	206.4

Table 16. Parameter Sensitivity Test.

case / para.	1	2
C_{y_β}	-1.1133	-2.1133
C_{l_β}	-.1139	-.2139
C_{n_β}	.2617	.4617
C_{y_p}	.1227	.2227
C_{l_p}	-.3439	-.4439
C_{n_p}	-.0556	-.1556
λ	-.0972 + 1.6287 i	-.1498 + 2.1899 i
$\vec{X}$	-16.9723 - 4.4236 i	-38.3838 -14.7943 i
	2.6825 - 2.4430 i	9.7076 - 7.2736 i
	-.1494 + .5641 i	-.5362 + 1.7740 i
	-47.5062 -47.0185 i	-107.5938 -126.875 i

Results

value / para.	Exact Value	Calculated Value
$\Delta\lambda$	-.053 + .560 i	-.050 + .573 i
$\Delta\vec{X}$	-21.412 - 10.371 i	-21.338 - 10.604 i
	7.025 - 4.831 i	6.939 - 4.686 i
	-.387 + 1.210 i	-.382 + 1.196 i
	-60.088 - 79.857 i	-59.368 - 80.365 i

Table 17. Eigendata Sensitivity Comparisons for Different Models.

para. / model / α (deg)	$\frac{\partial \lambda}{\partial C_{l_\beta}}$		$\frac{\partial \lambda}{\partial C_{n_\beta}}$		$\frac{\partial \lambda}{\partial C_{l_p}}$		$\frac{\partial \lambda}{\partial C_{n_p}}$	
	unsteady	combined	unsteady	combined	unsteady	combined	unsteady	combined
25	.761 -15.460 i	1.503 -13.883 i	.017 +1.885 i	-.535 +1.565 i	2.189 + .465 i	1.977 + .403 i	-.269 -.041 i	-.218 -.098 i
30	.071 - 8.540 i	.049 - 8.451 i	.203 + .845 i	-.024 + .816 i	1.772 + .135 i	1.768 + .014 i	-.178 +.030 i	-.171 -.005 i
35	.150 - 7.149 i	- .127 -. 7.257i	.252 +.611 i	-.116 + .536 i	1.689 - .075 i	1.690 - .390 i	-.140 +.069 i	-.131 -.0005 i
40	.234 -10.872 i	- .396 -10.973 i	.003 +.004 i	-.0001 + .0045 i	1.537 - .151 i	1.549 - .375 i	-.105 +.032 i	-.101 +.001 i
45	-.574 -13.245 i	- .144 -13.398 i	-.109 +.793 i	-.029 + .769 i	1.335 + .270 i	1.315 + .398 i	-.076 -.030 i	-.074 -.027 i

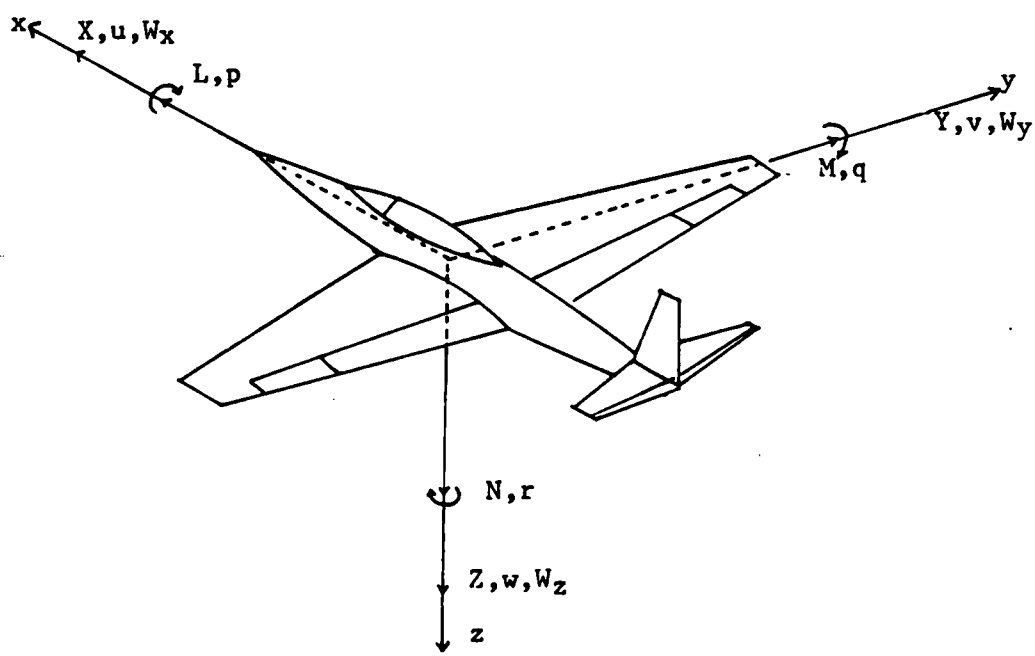

Figure 1. Body Axes Coordinate System.

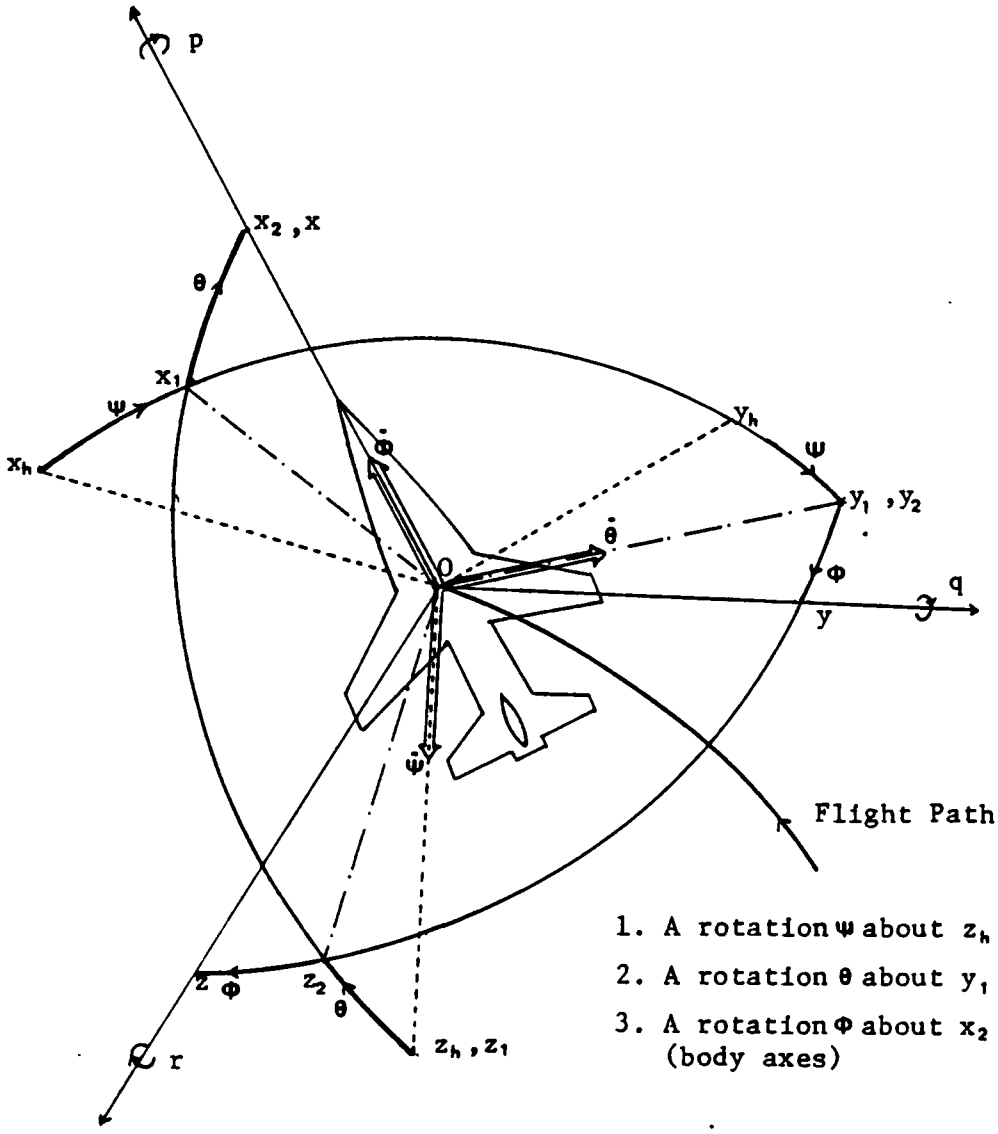

1. A rotation ψ about z_h to $x_1 y_1 z_1$
2. A rotation θ about y_1 to $x_2 y_2 z_2$
3. A rotation Φ about x_2 to x y z (body axes)

Figure 2. Kinematic Relation of Euler Angles and Euler Angle Rates (Ref. 17).

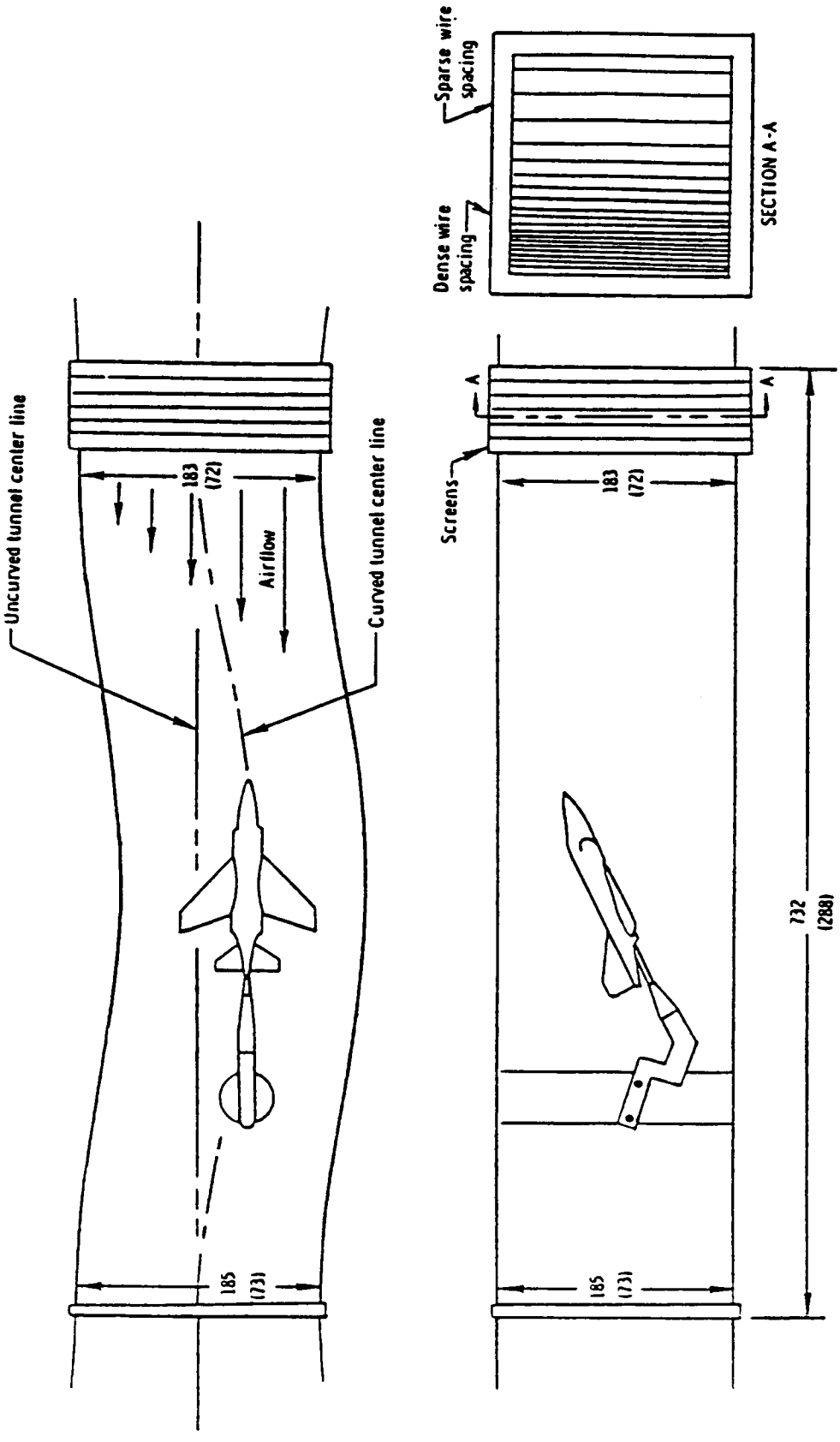

Figure 3. Curved Flow Test Section, VPI&SU (Ref. 23).
Dimensions are given in cm (in)

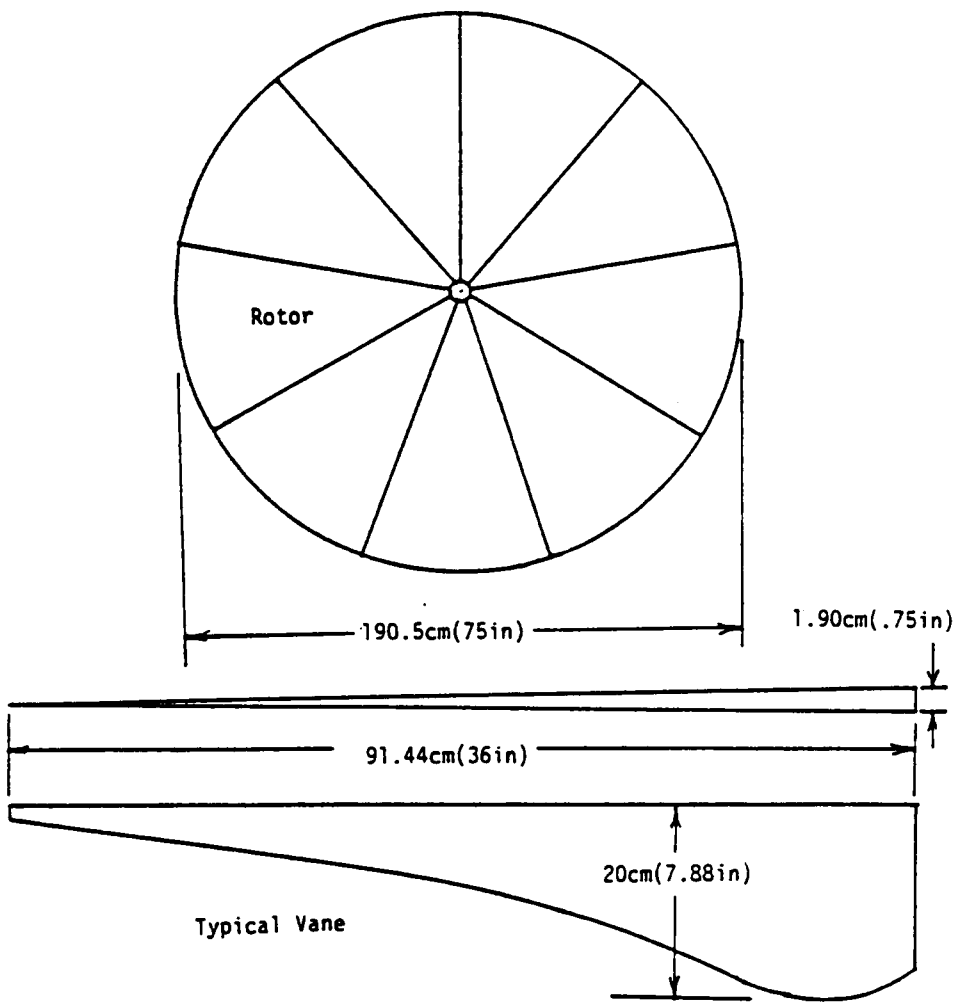

Figure 4. Rolling Flow Rotor and Vane, VPI&SU (Ref. 24).

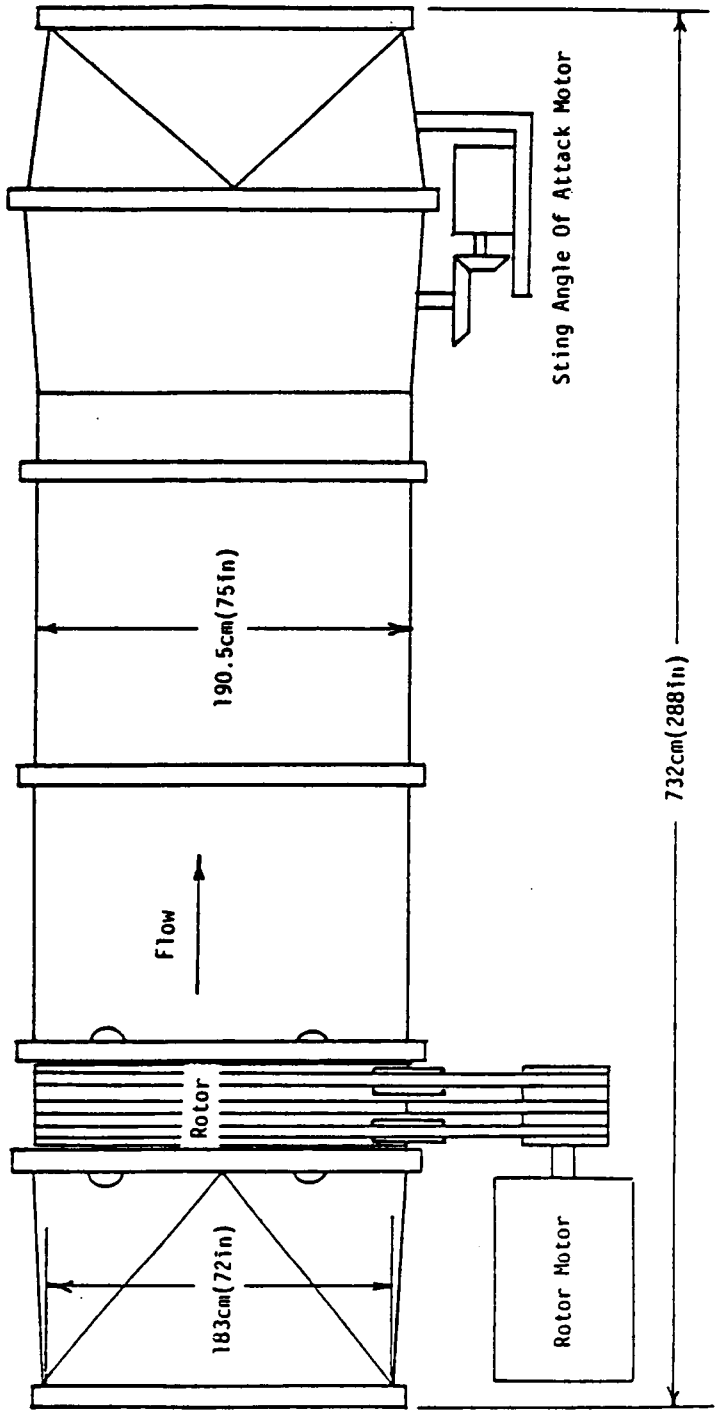

Figure 5. Rolling Flow Test Section, VPI&SU (Ref. 24).

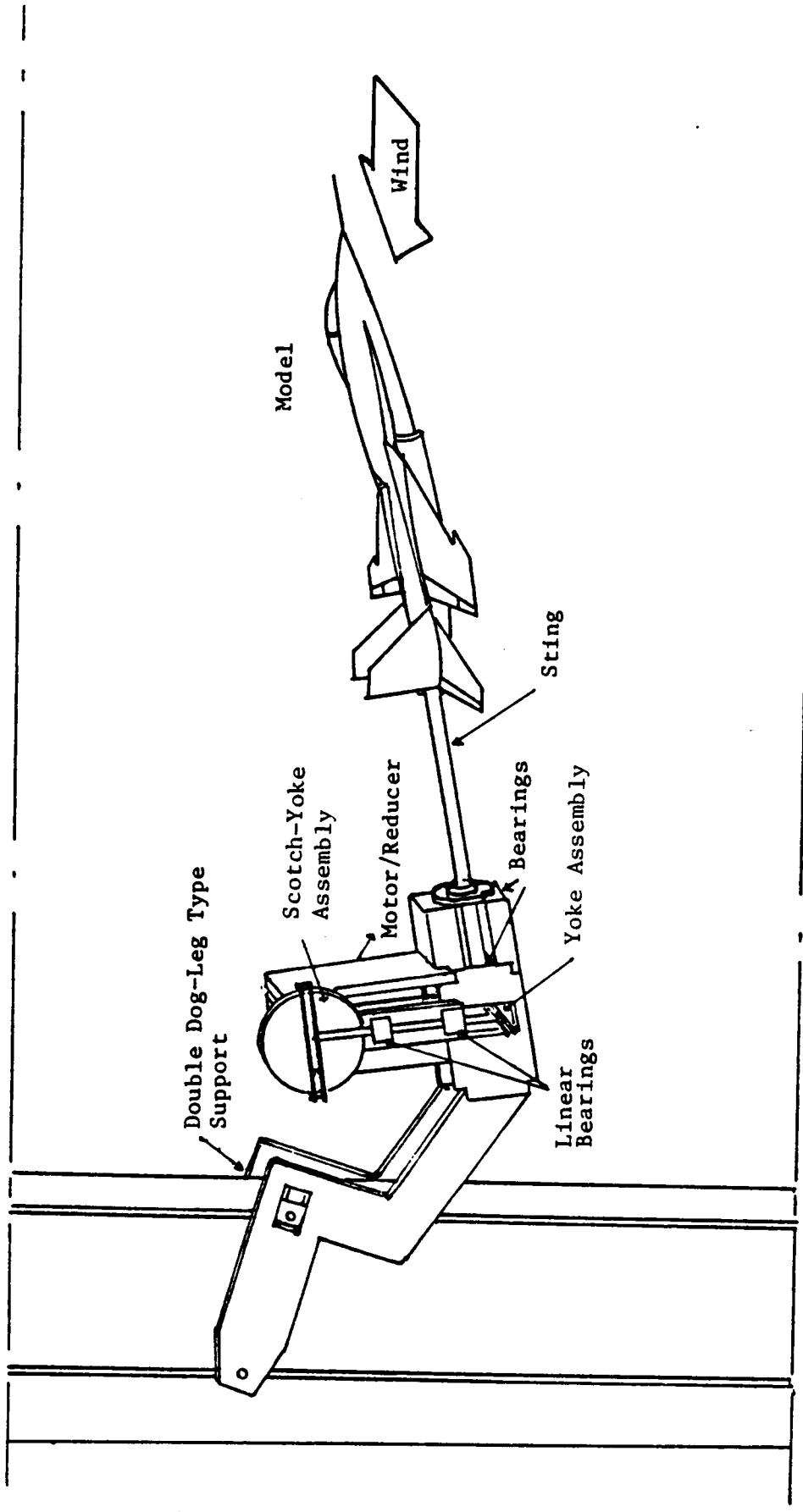

Figure 6. Roll Oscillatory Rig, VPI&SU.

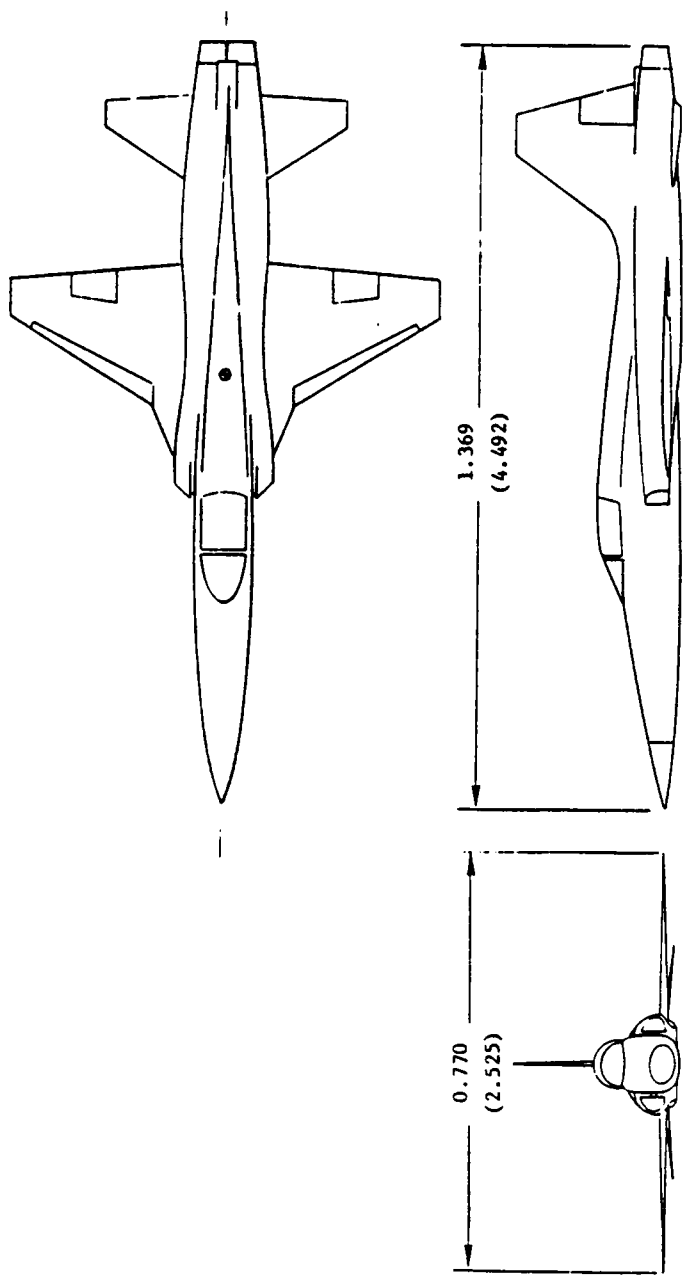

Figure 7. Three-View Sketch of F-5 Model (Ref. 25).
Dimensions are given in m (ft)

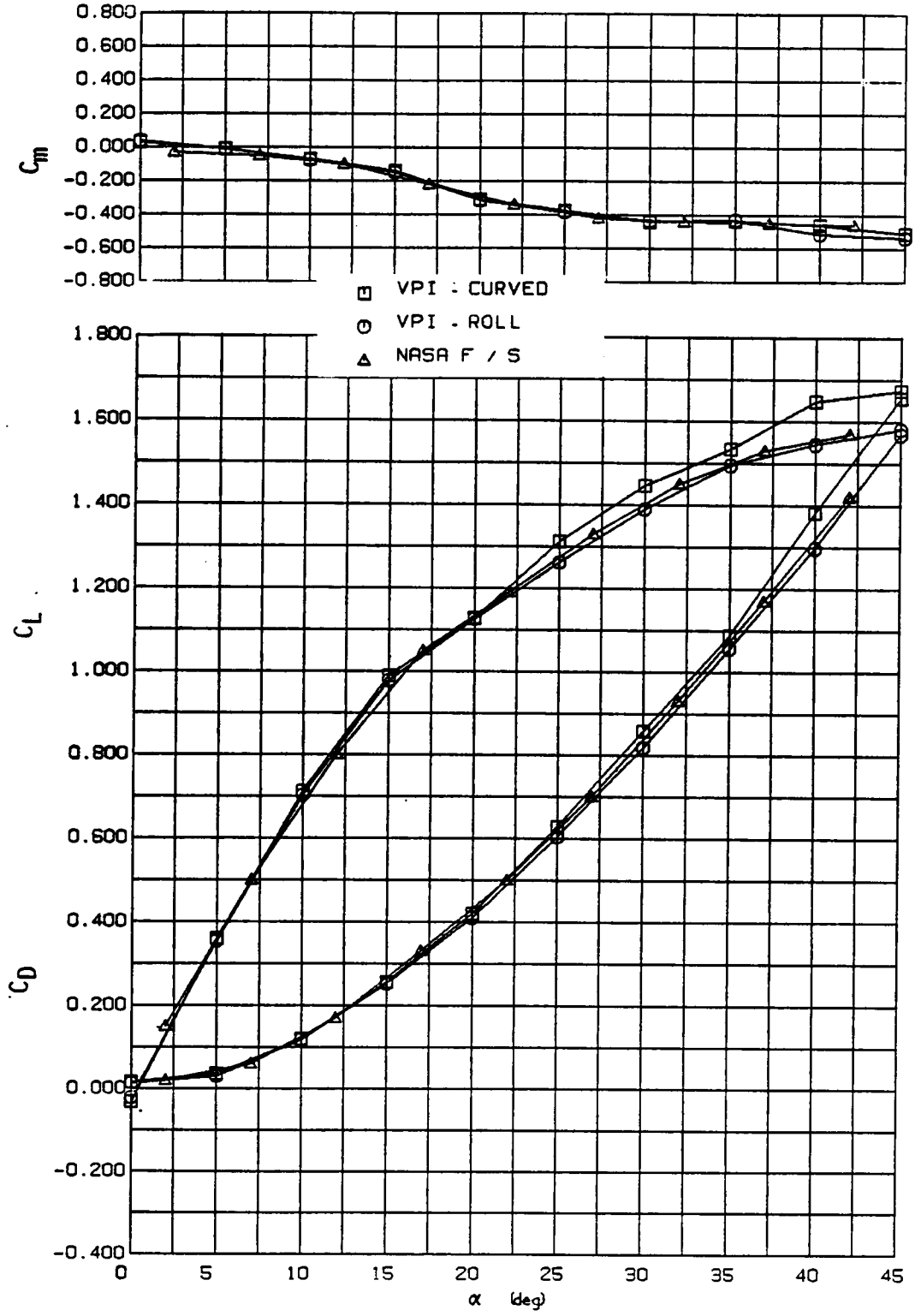

Figure 8 . Comparison of Static Longitudinal Characteristics.

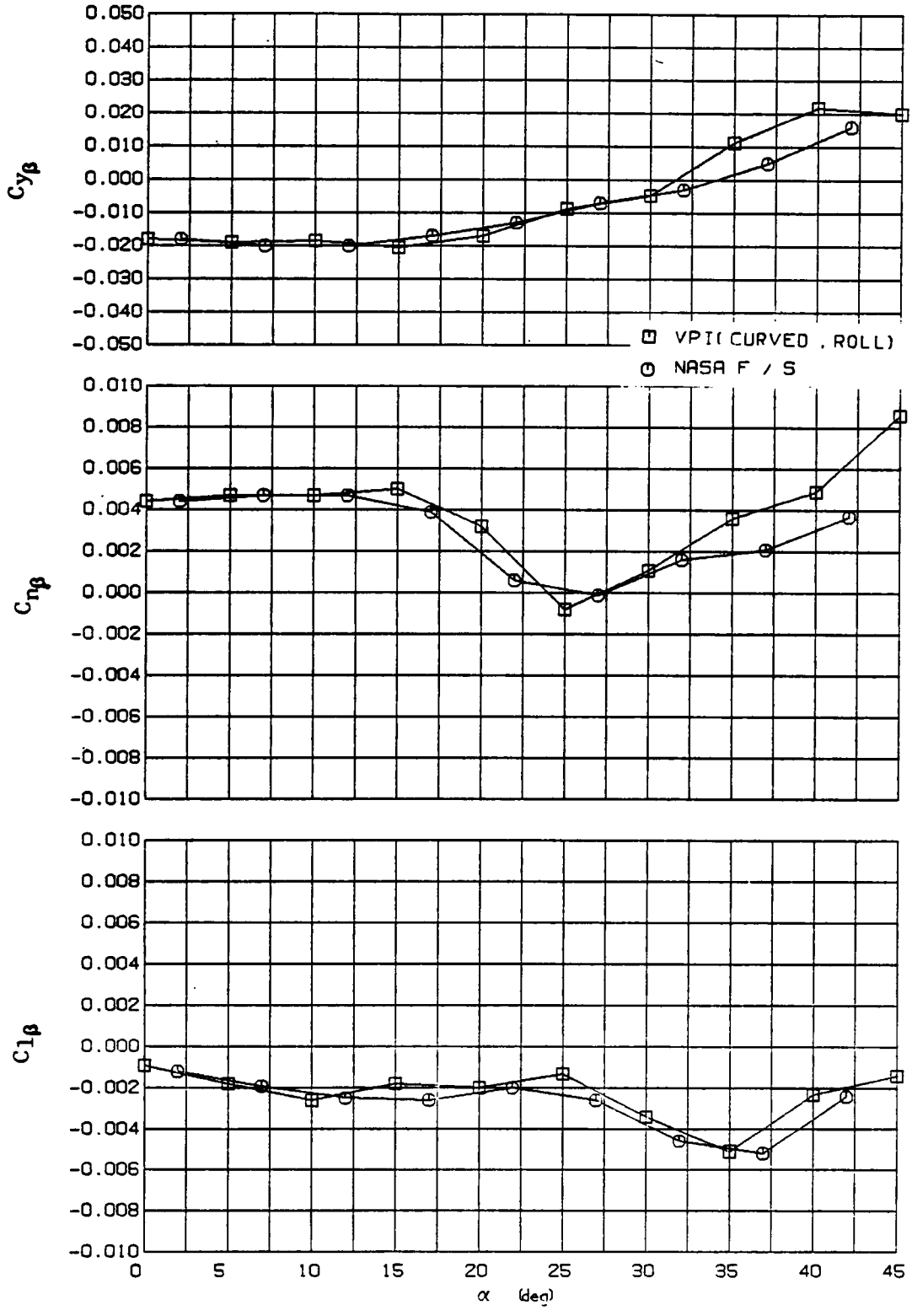

Figure 9. Comparison of Static Lateral Characteristics.

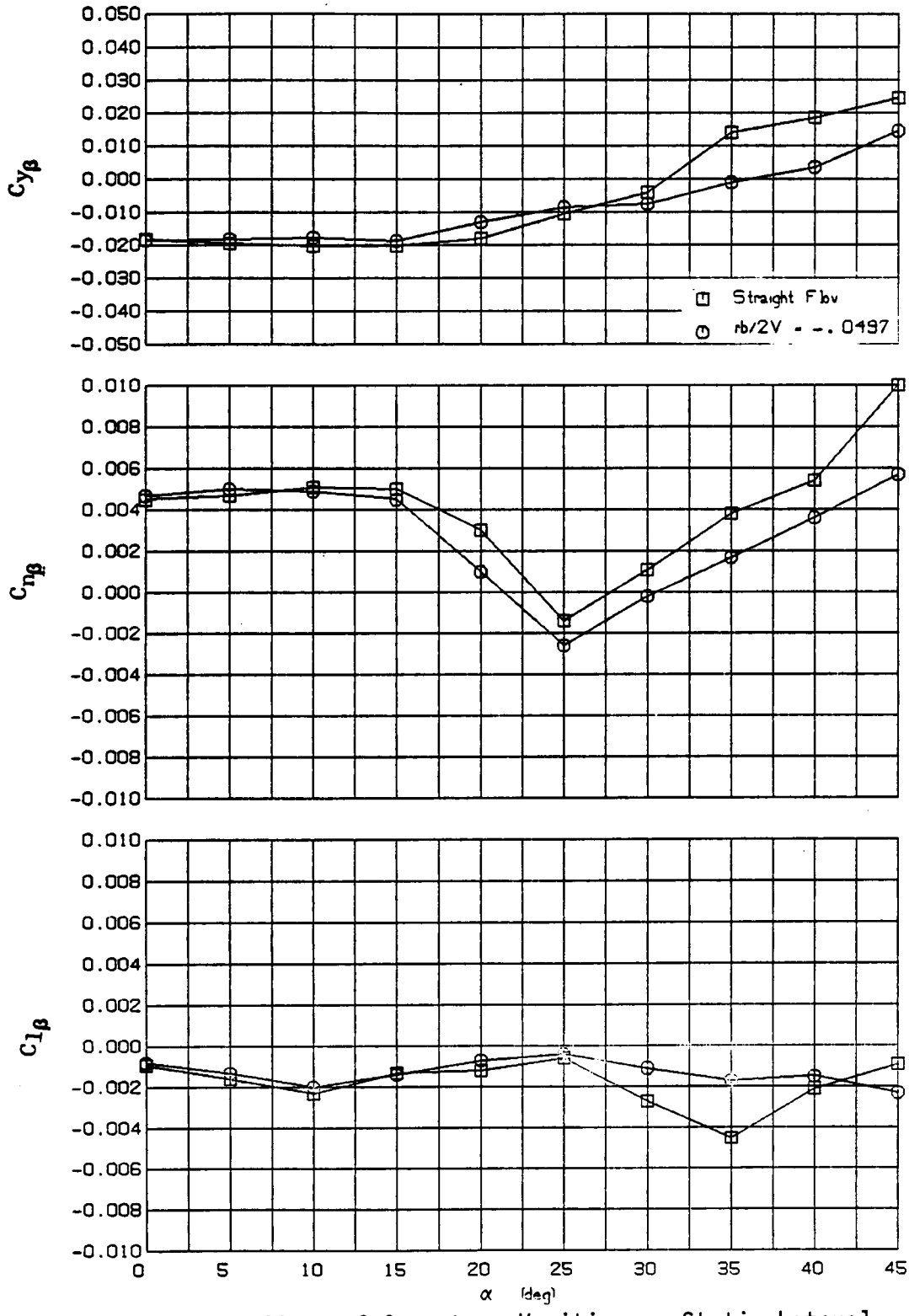

Figure 10. Effect of Curvature Varition on Static Lateral Directional Stability.

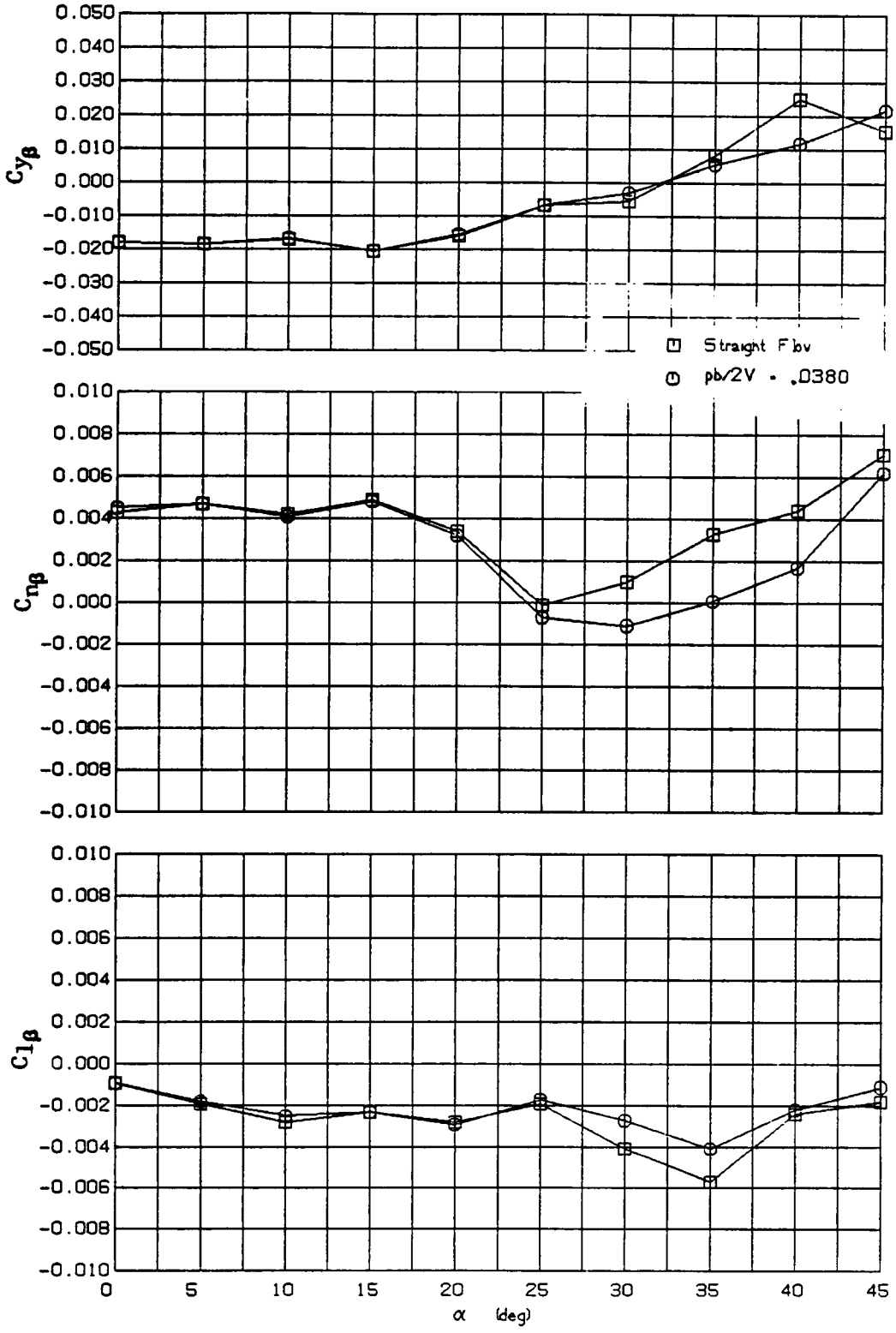

Figure 11. Effect of Roll Rate Variation on Static Lateral Directional Stability.

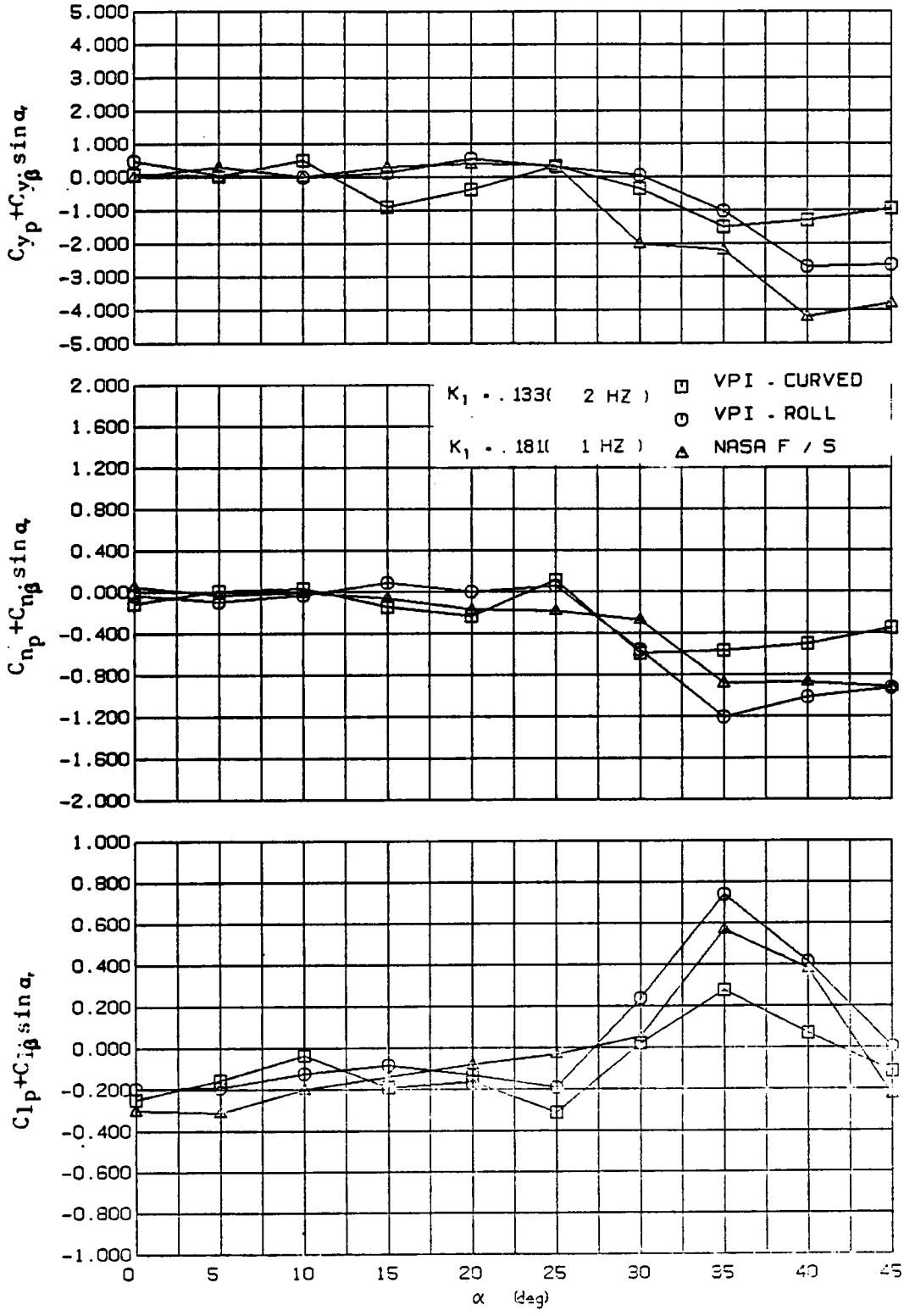

Figure 12. Comparison of Oscillatory Derivatives from Different Tests.

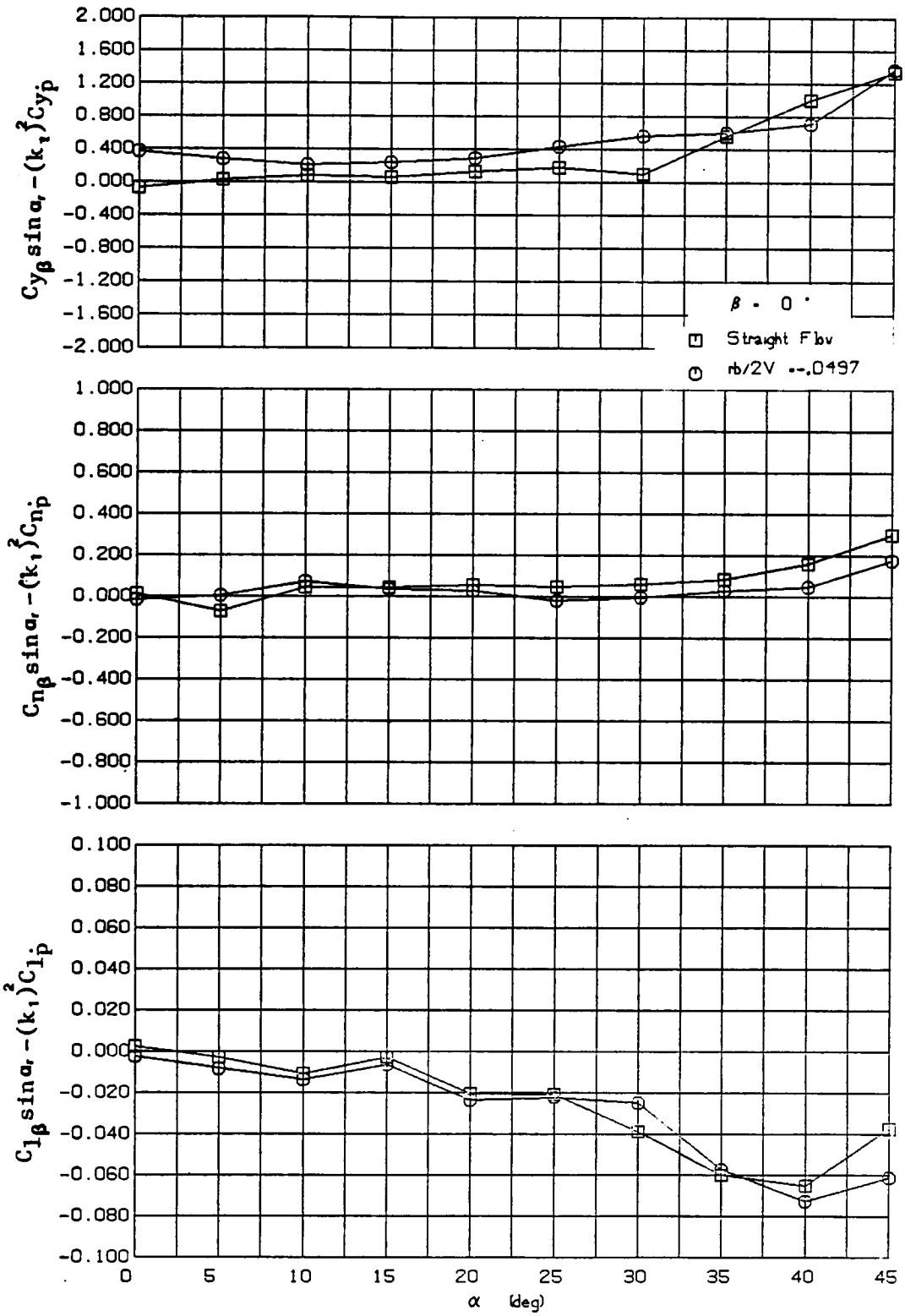

Figure 13. Effect of Curvature Variation on In-Phase Oscillatory Derivatives ($\beta = 0°$, $k_1 = .133$).

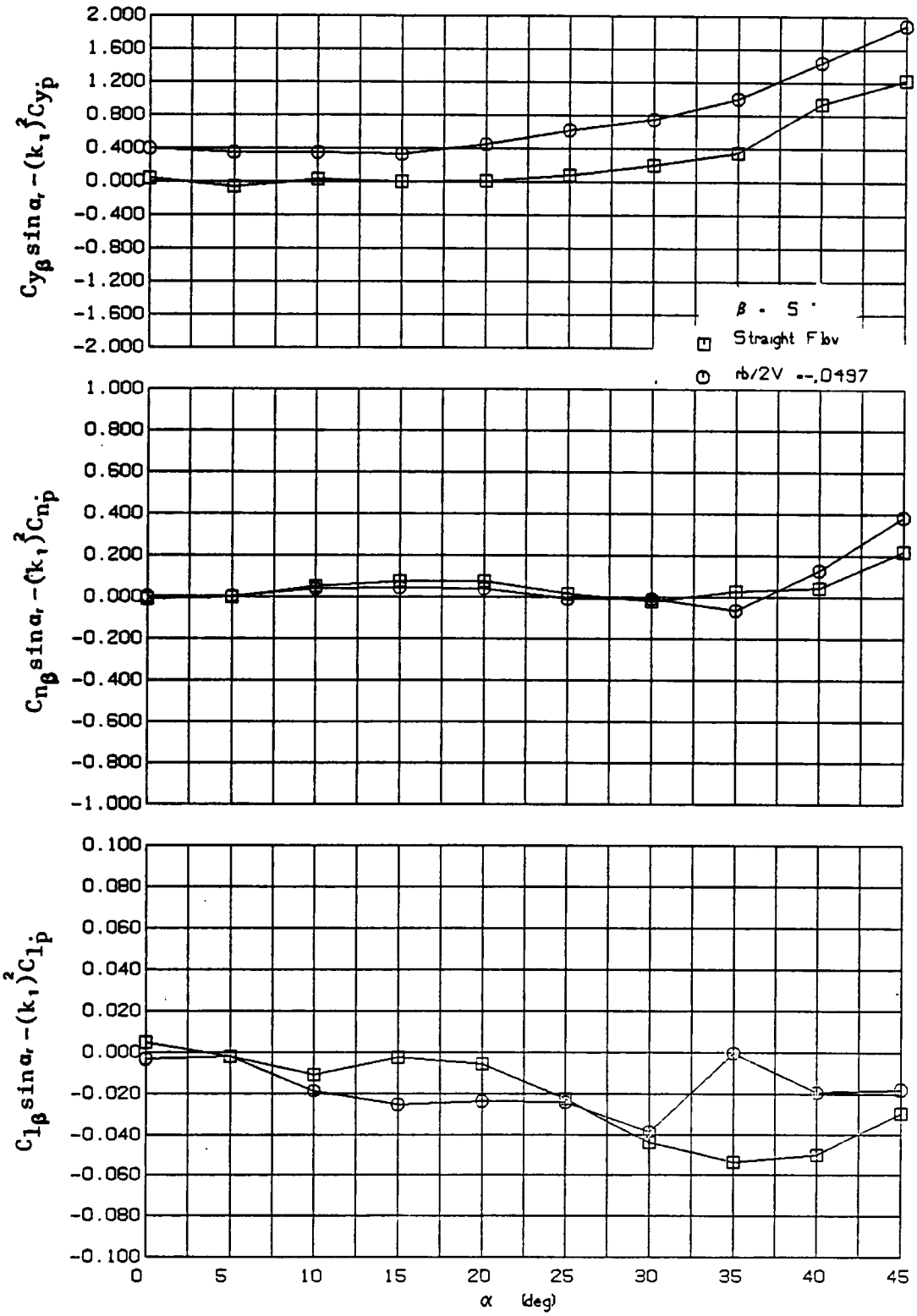

Figure 14. Effect of Curvature Variation on Ir - Phase Oscillatory Derivatives (β = 5 °, k_1 = .133).

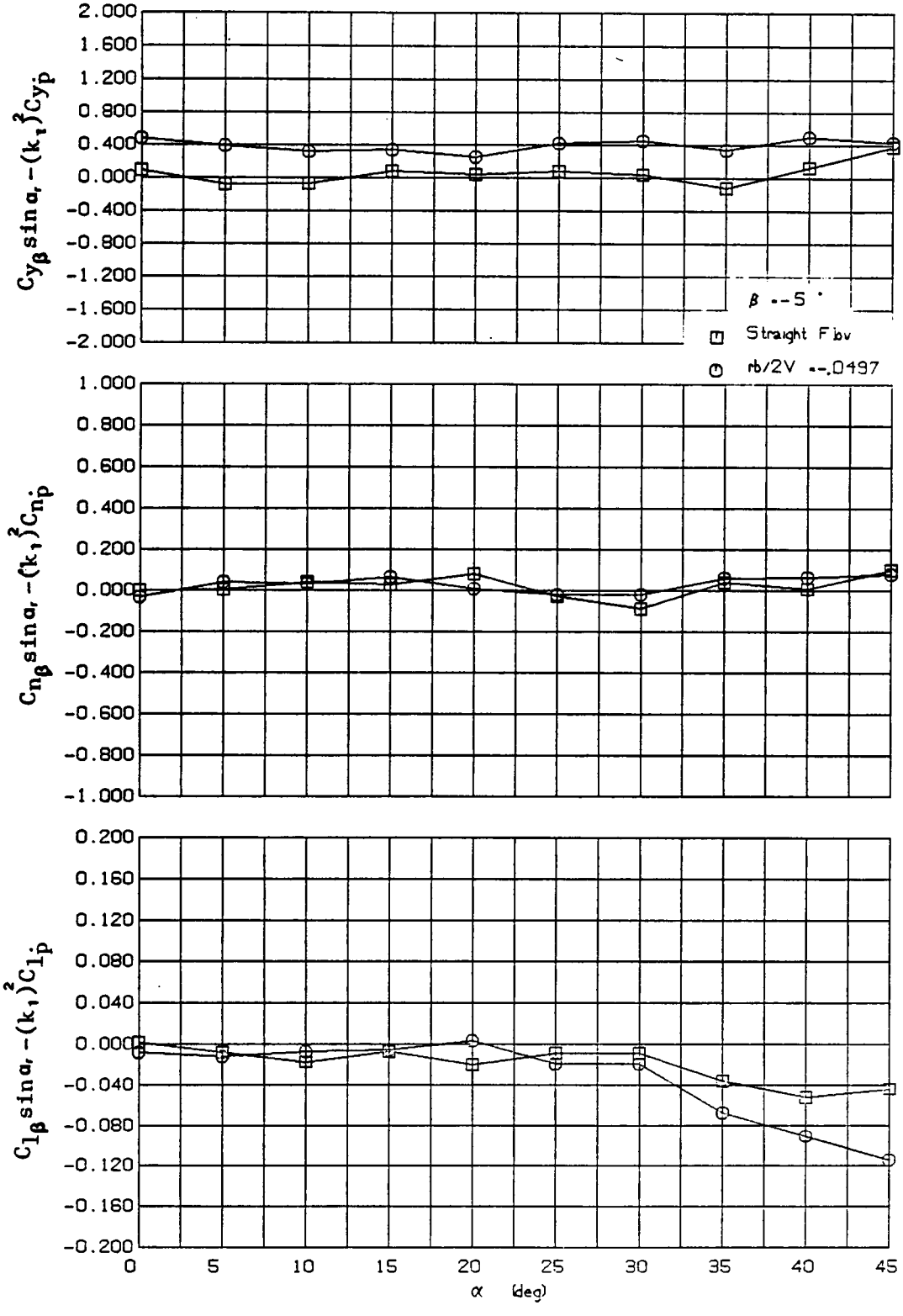

Figure 15. Effect of Curvature Variation on Ir - Phase Oscillatory Derivatives ($\beta = -5°$, $k_1 = .133$).

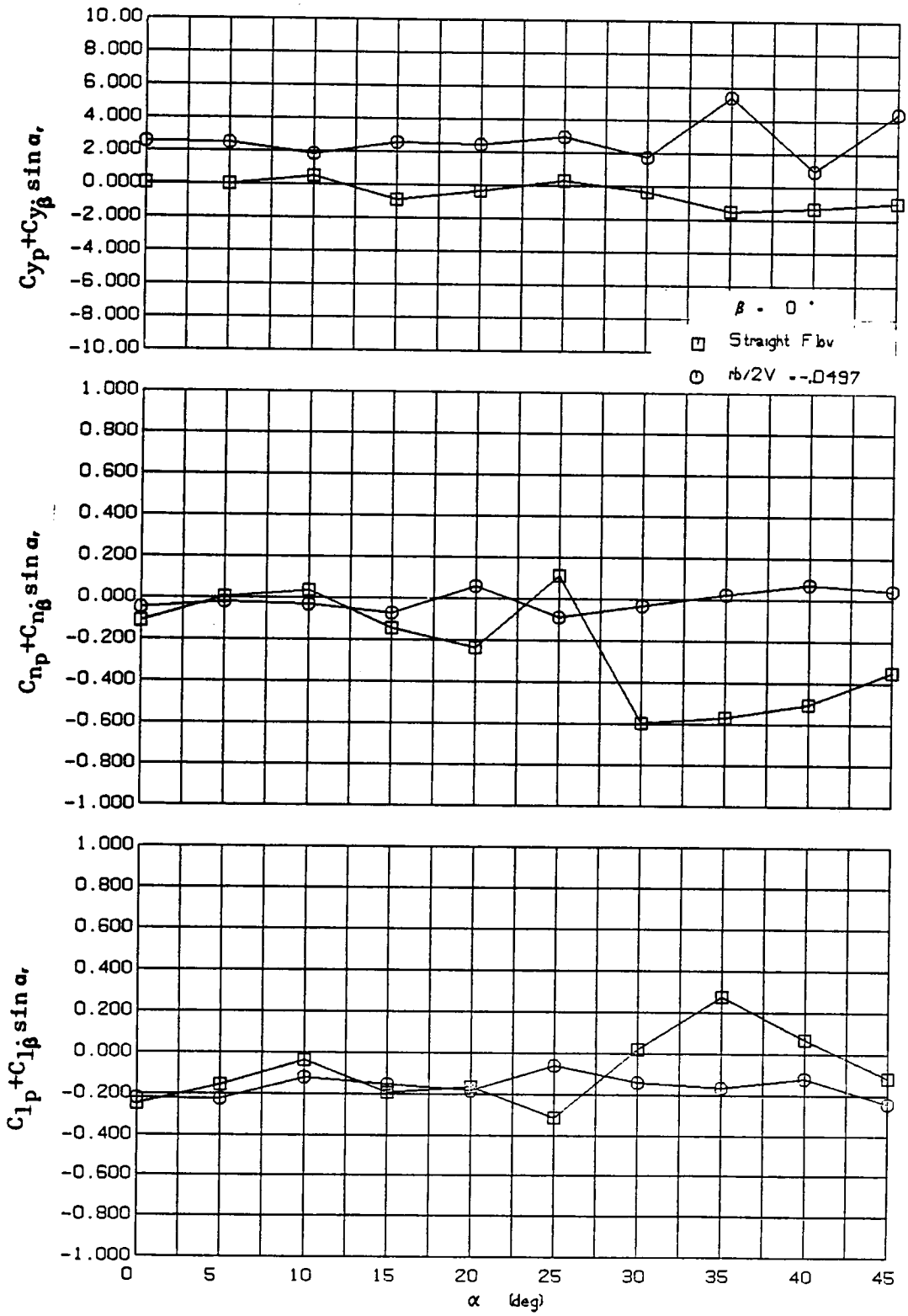

Figure 16. Effect of Curvature Variation on Out-of-Phase Oscillatory Derivatives ($\beta = 0^\circ$, $k_1 = .133$).

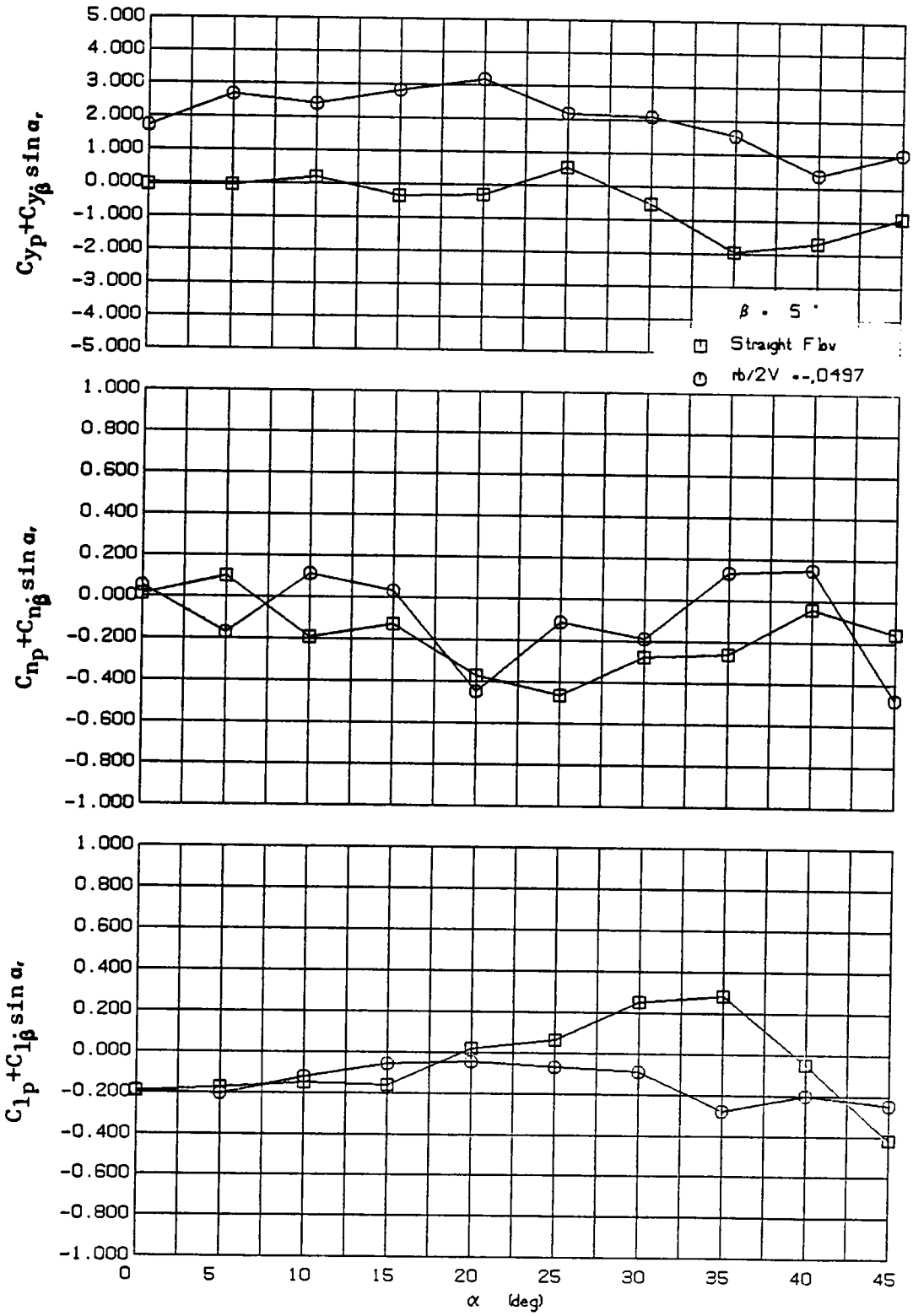

Figure 17. Effect of Curvature Variation on Out-of Phase Oscillatory Derivatives ($\beta = 5°$, $k_1 = .133$).

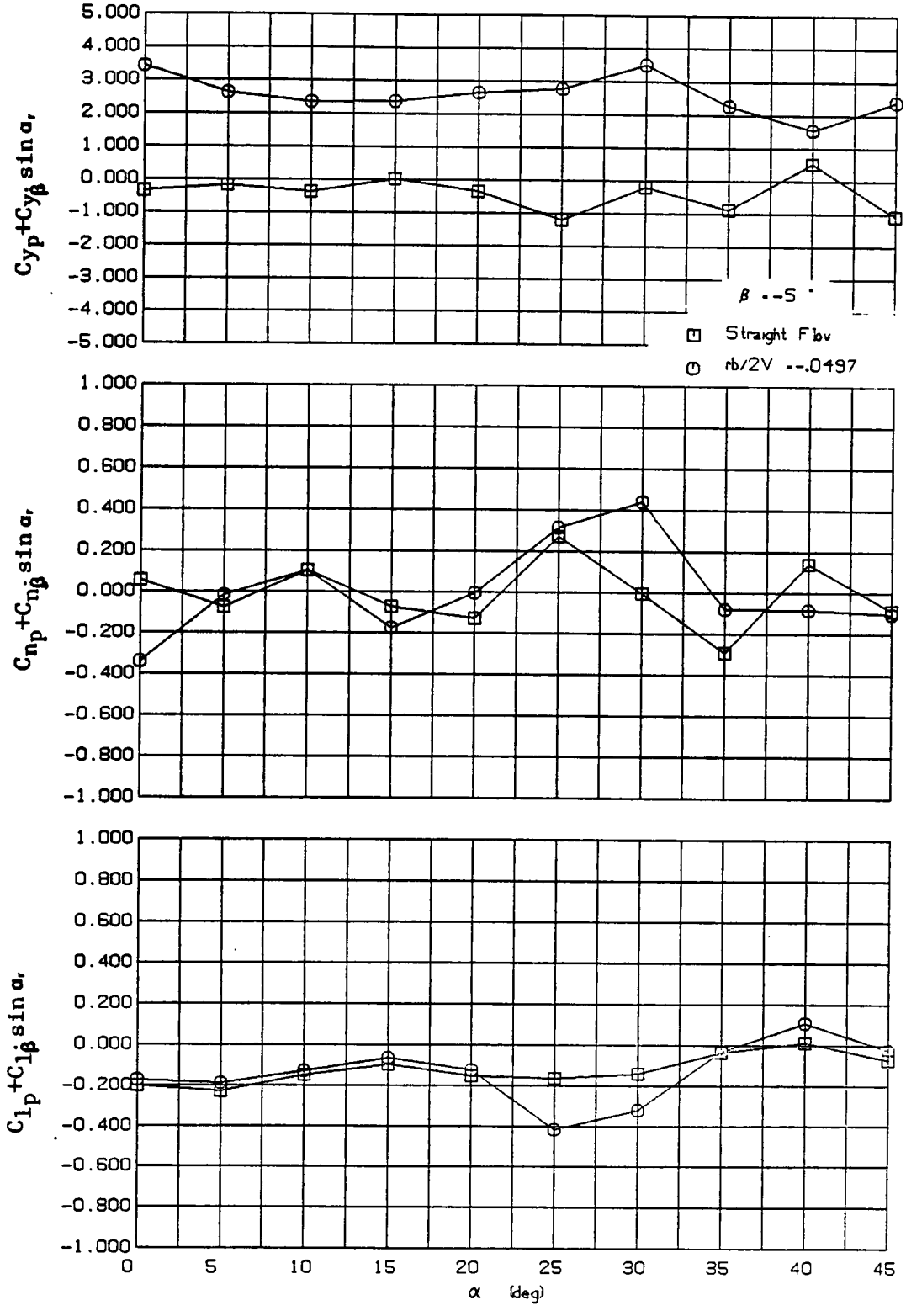

Figure 18. Effect of Curvature Variation on Out-of-Phase Oscillatory Derivatives ($\beta = -5°$, $k_1 = .133$).

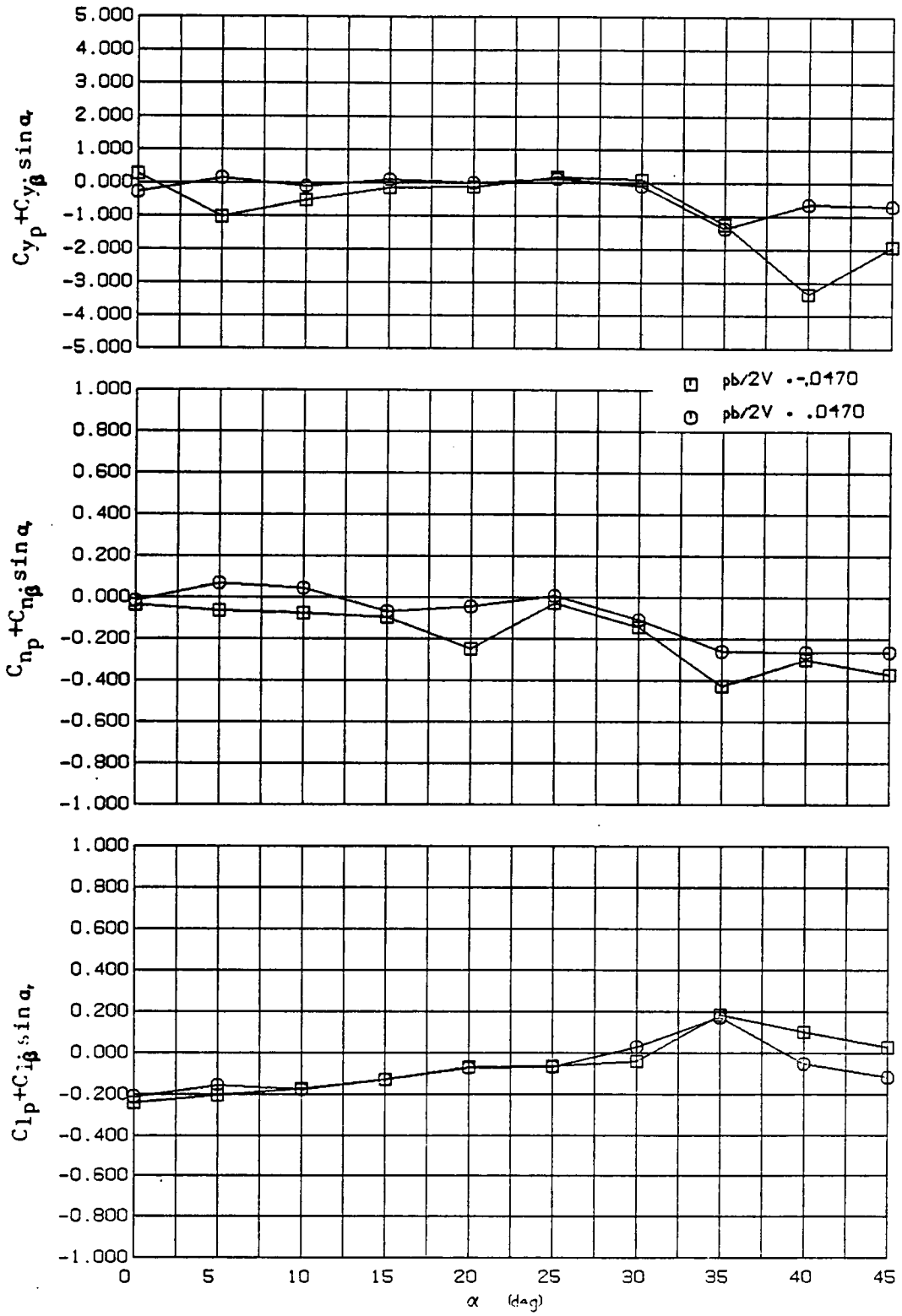

Figure 19. Effect of Rolling Flow Variation on Out-of-Phase Oscillatory Derivatives (1) (k_1 = .133).

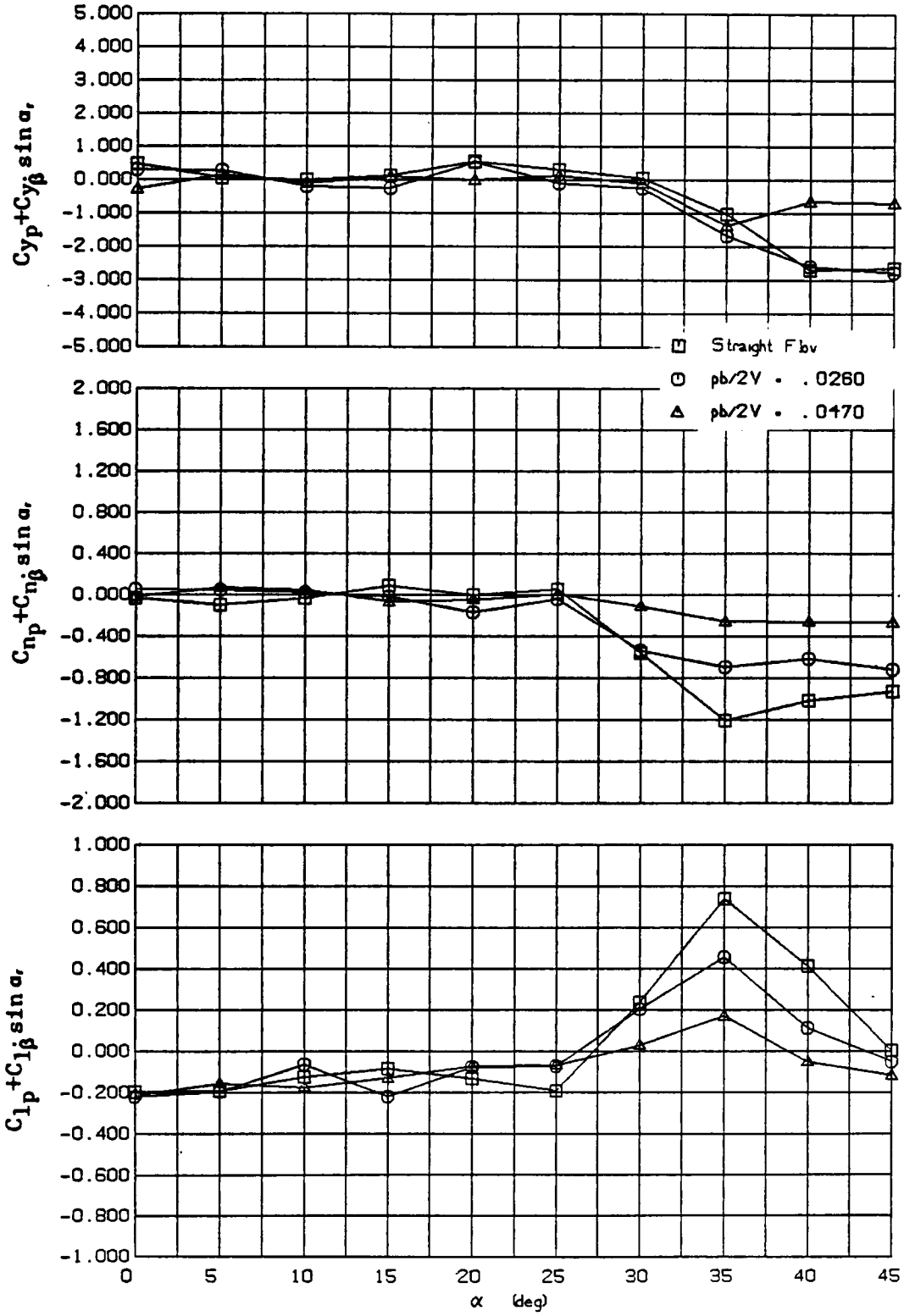

Figure 20. Effect of Rolling Flow Variation on Out-of-Phase Oscillatory Derivatives (2) (k_1 = .133).

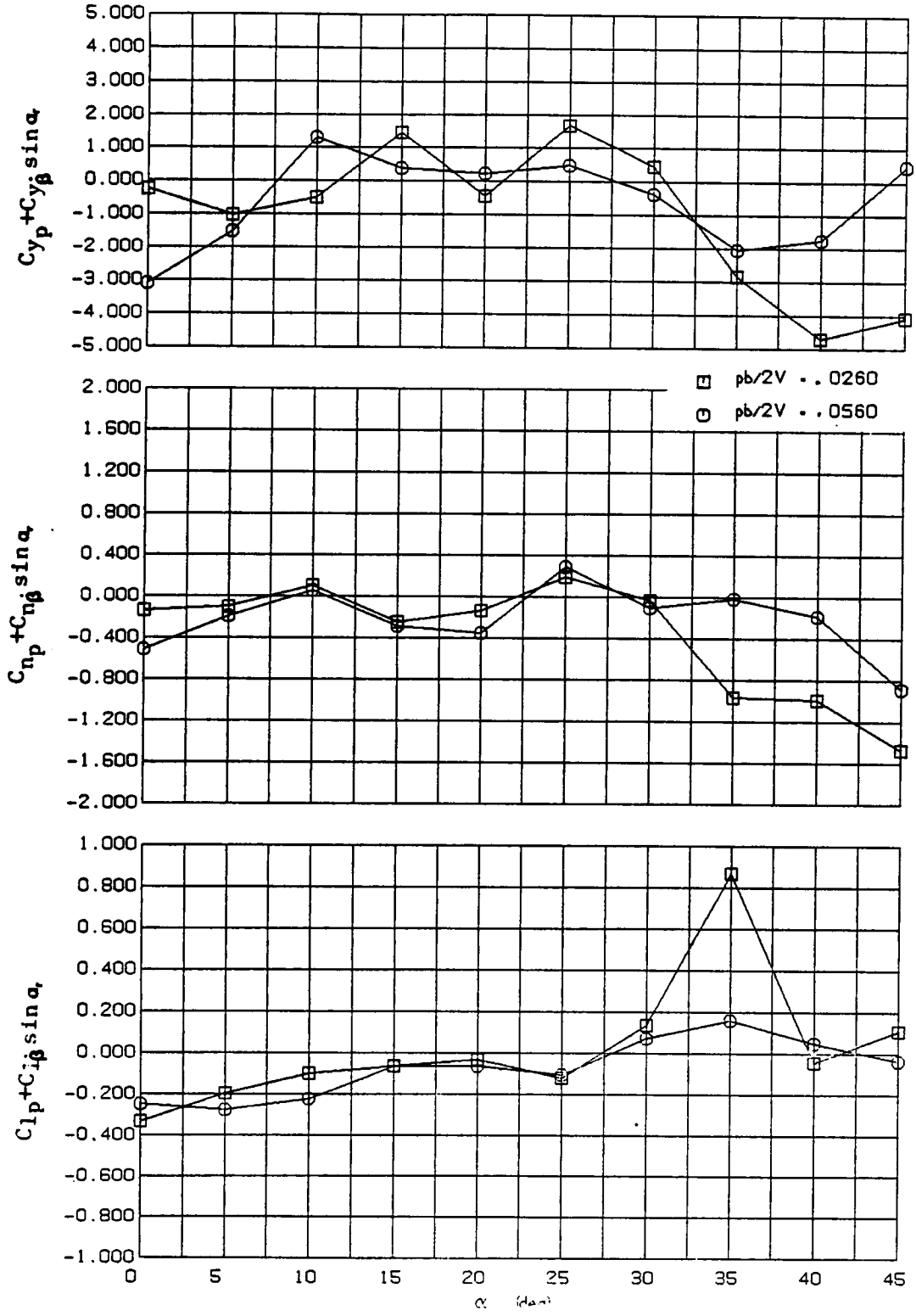

Figure 21. Effect of Rolling Flow Variation on Out-of-Phase Oscillatory Derivatives (k_1 = .033).

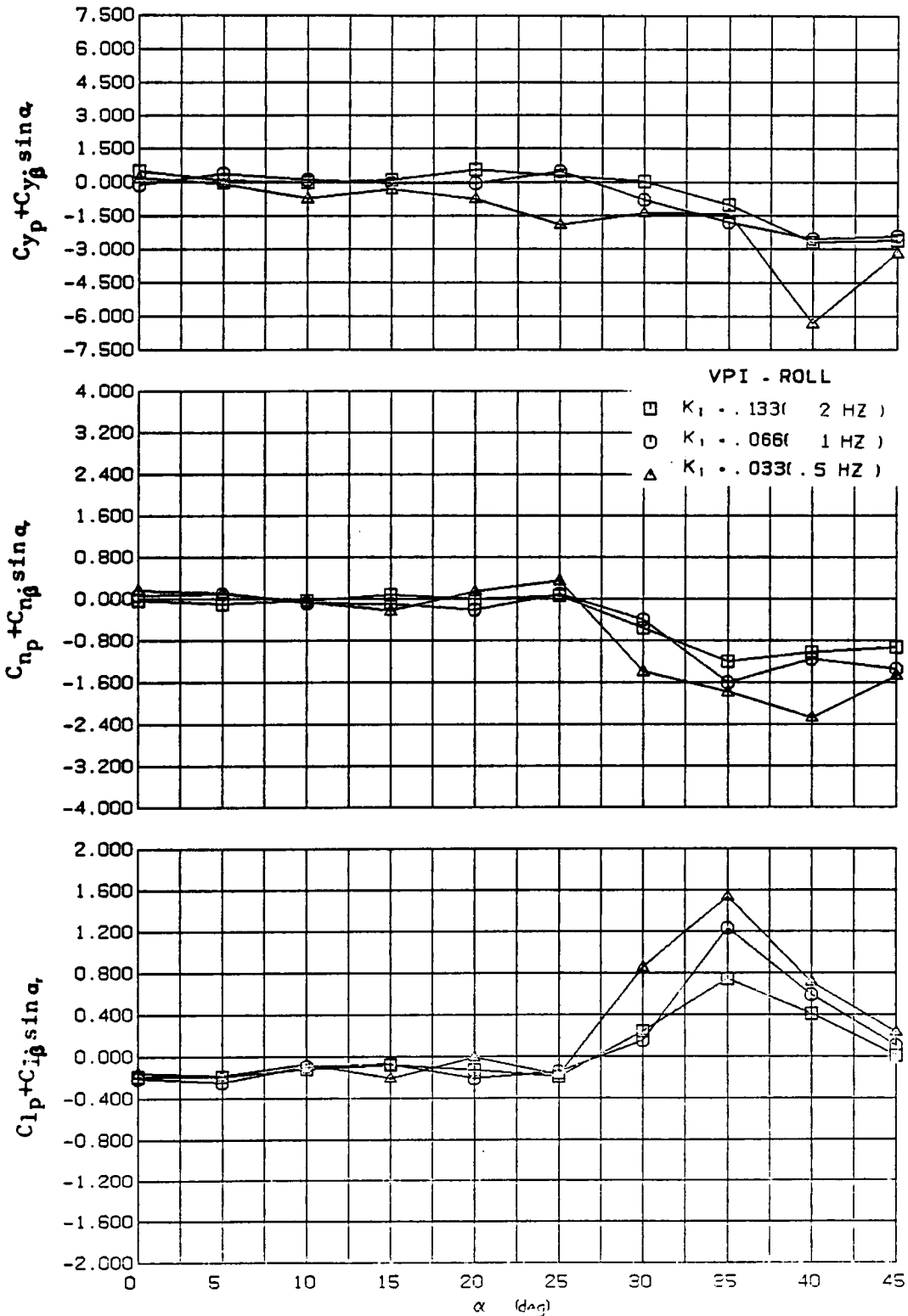

Figure 22. Comparison of Oscillatory Derivatives for Different Frequencies.

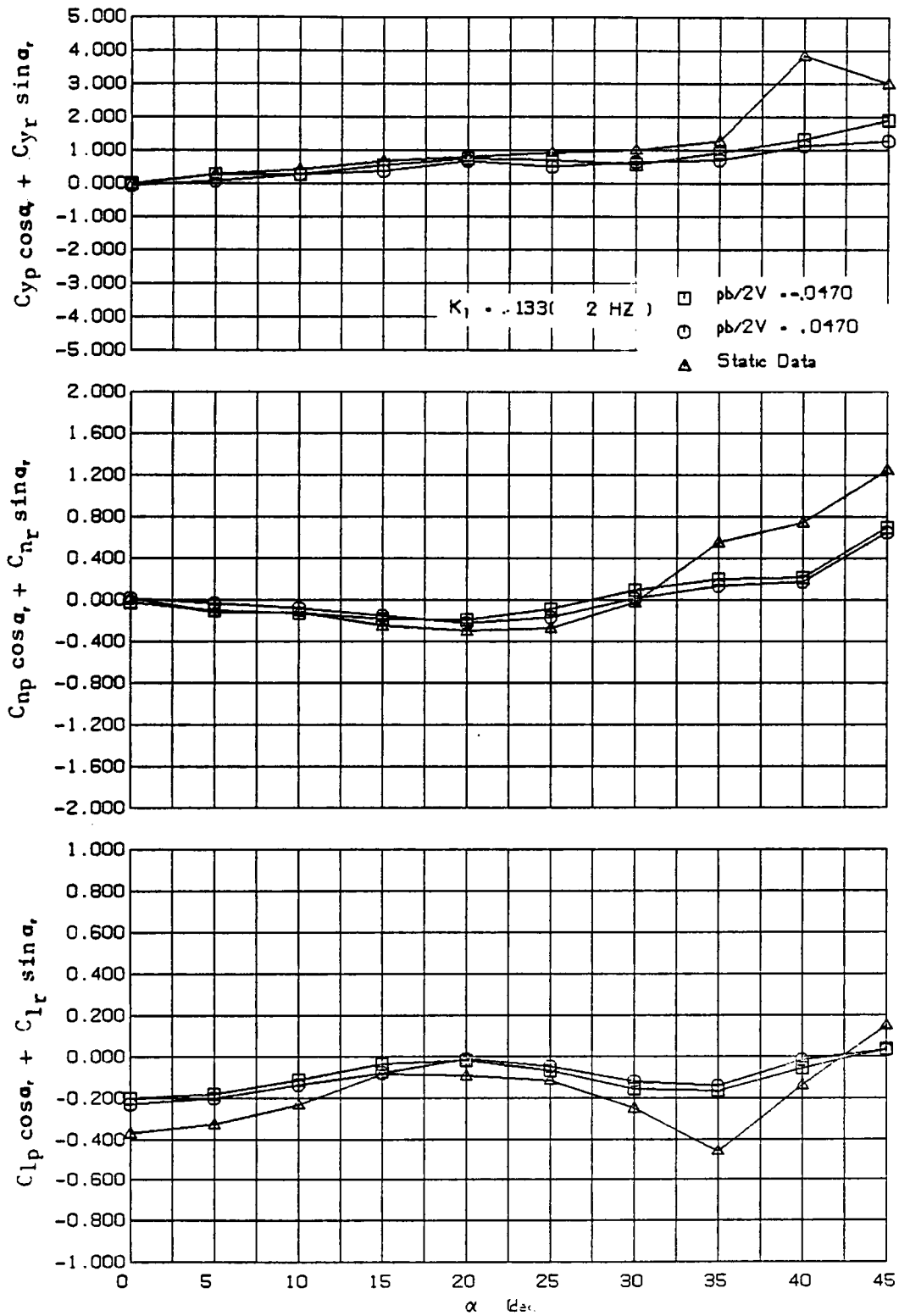

Figure 23. Comparison of Combined Pure Rotational Derivatives from Different Tests.

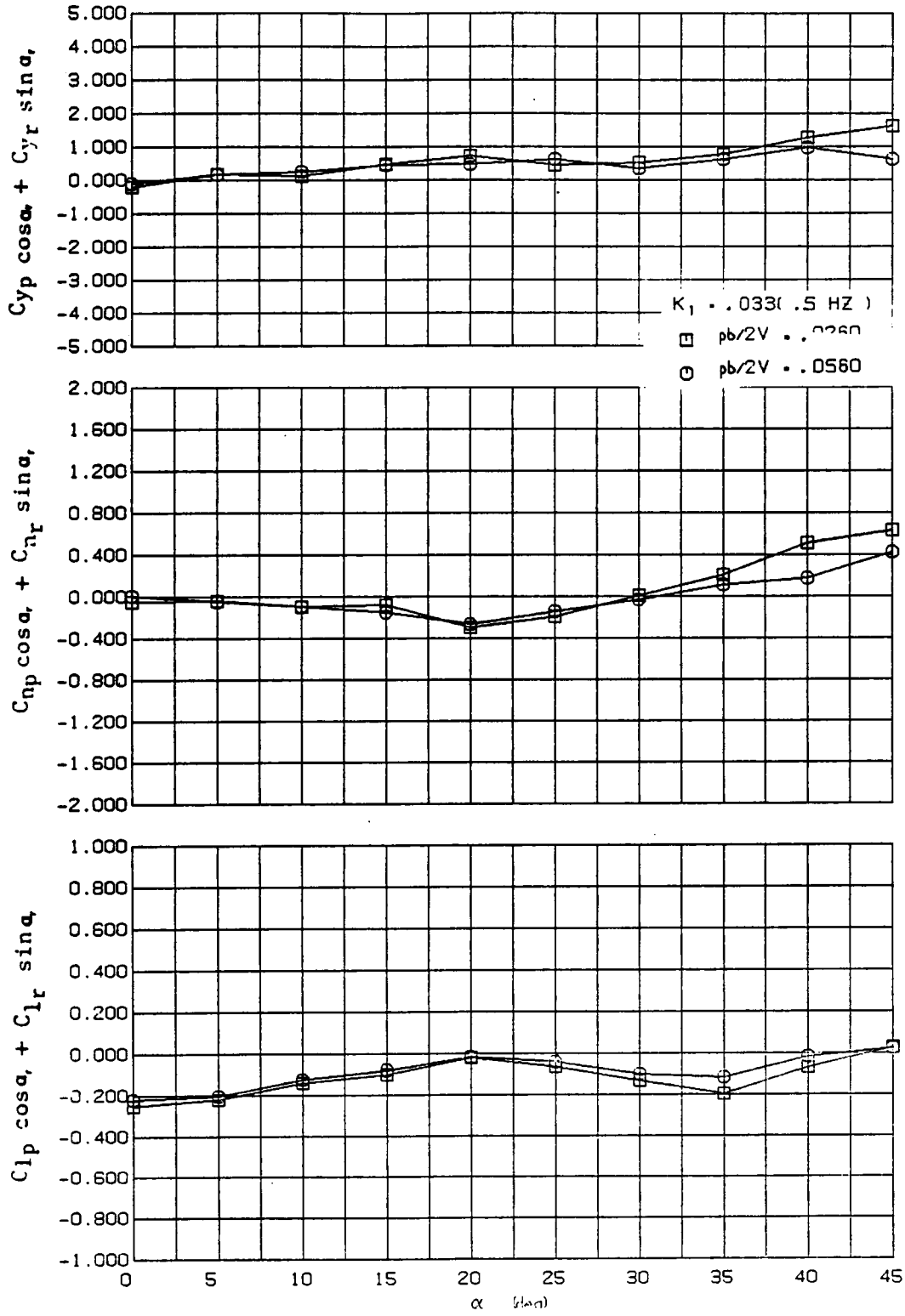

Figure 24. Comparison of Combined Pure Rotational Derivatives for Different Roll Frequency.

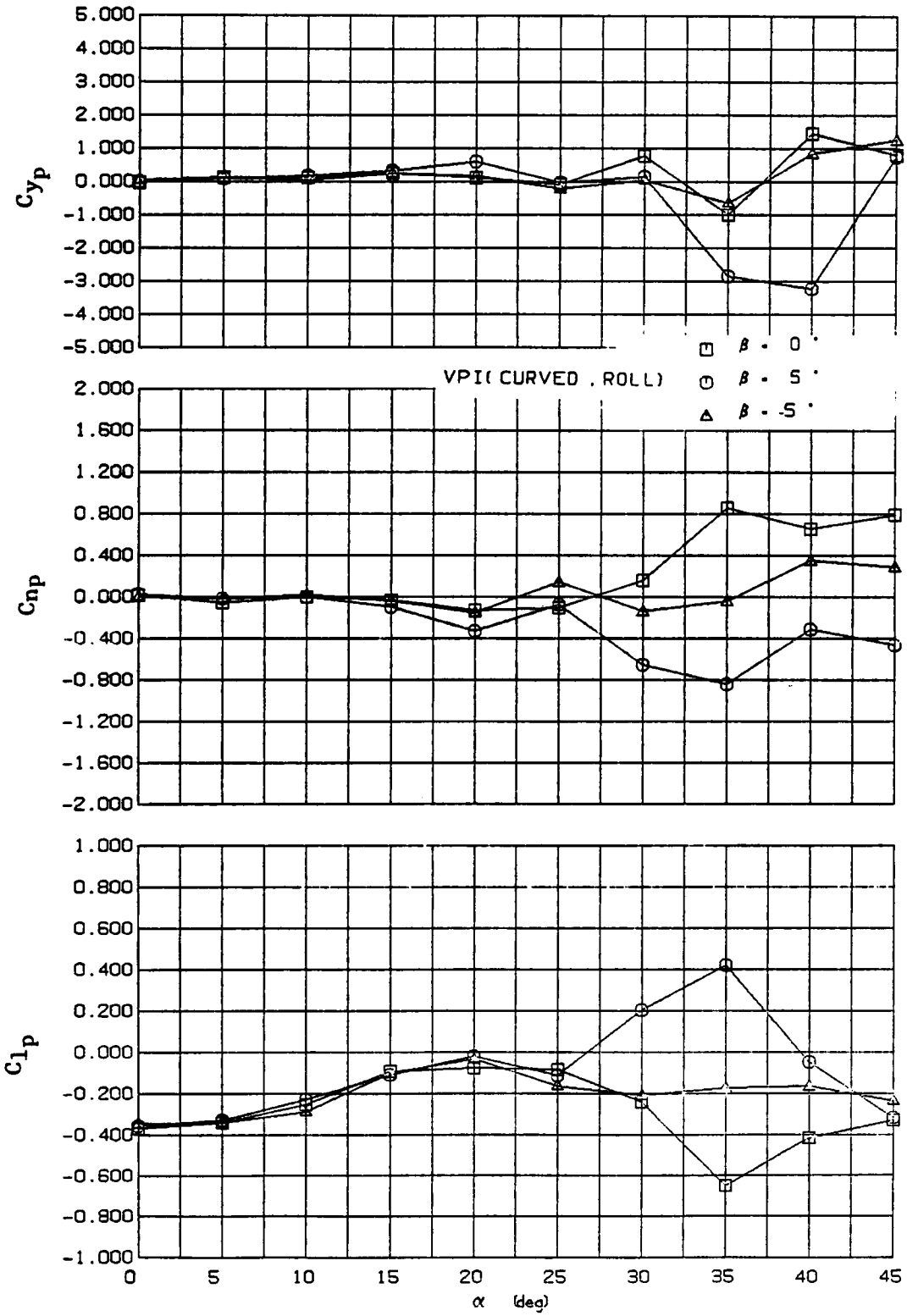

Figure 25. Variation of Pure Rotational Derivatives for Different Side Slip Angles(1).

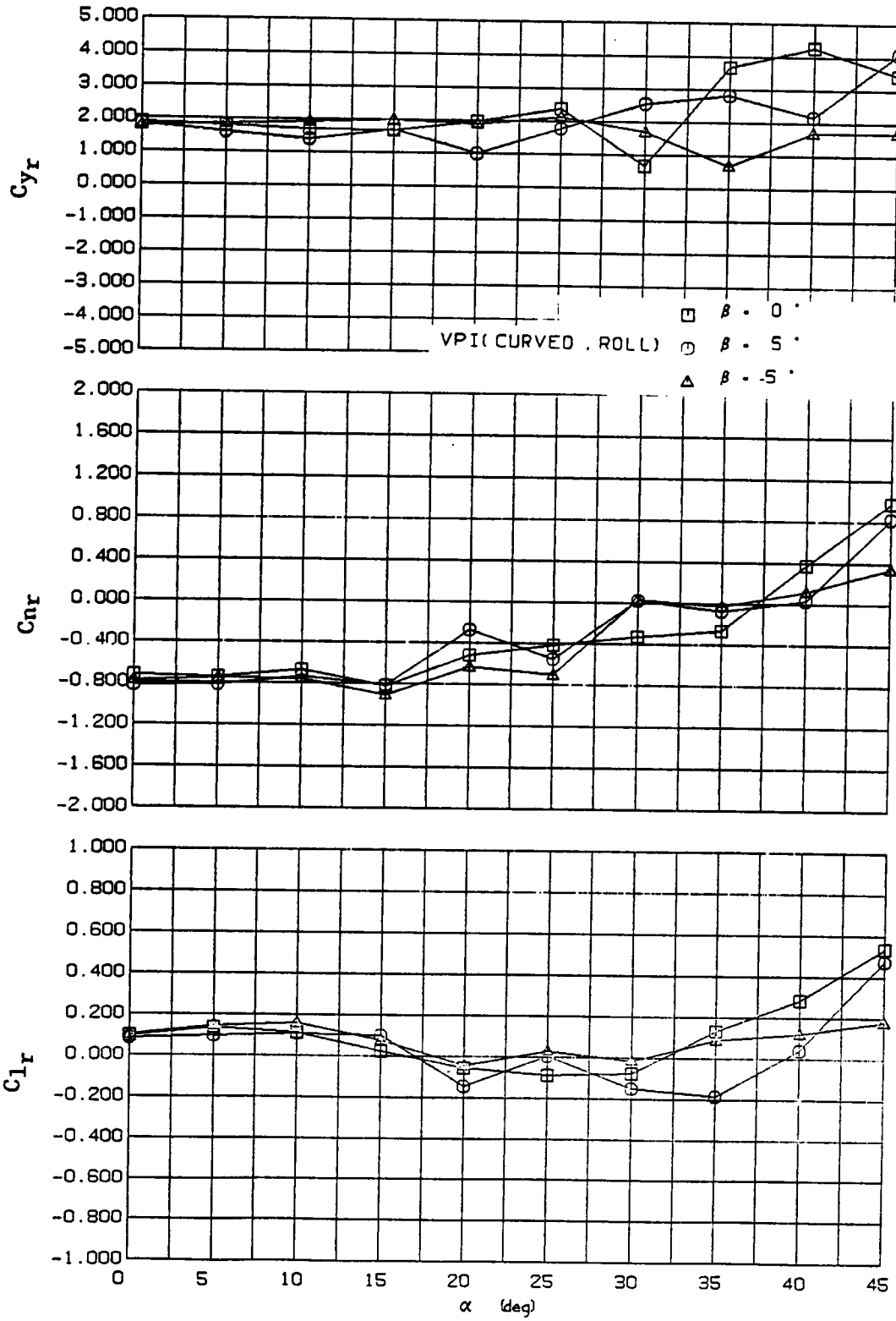

Figure 26. Variation of Pure Rotational Derivatives for Different Sideslip Angles (2).

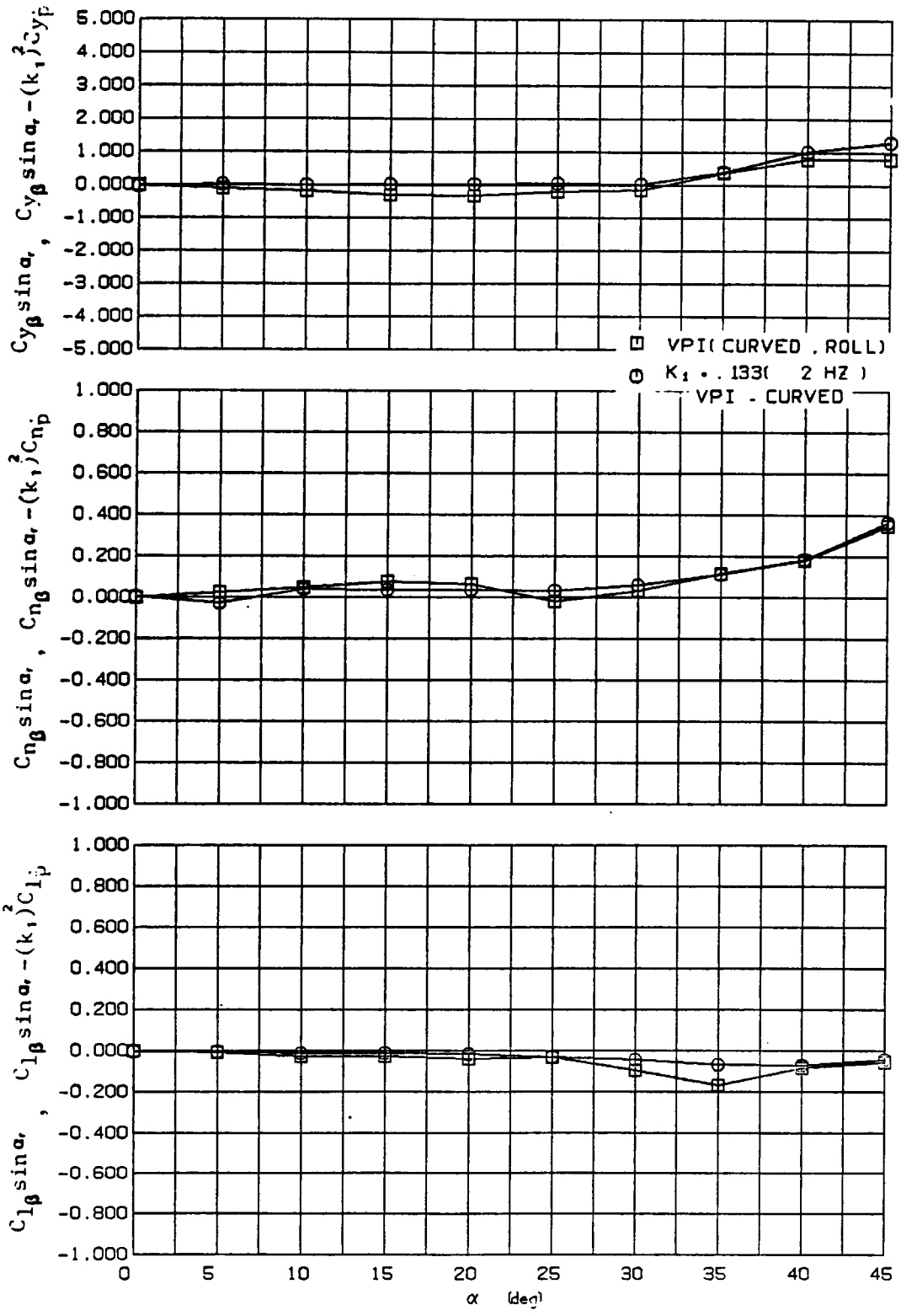

Figure 27. Comparison of Static and In-Phase Derivatives from Different Tests.

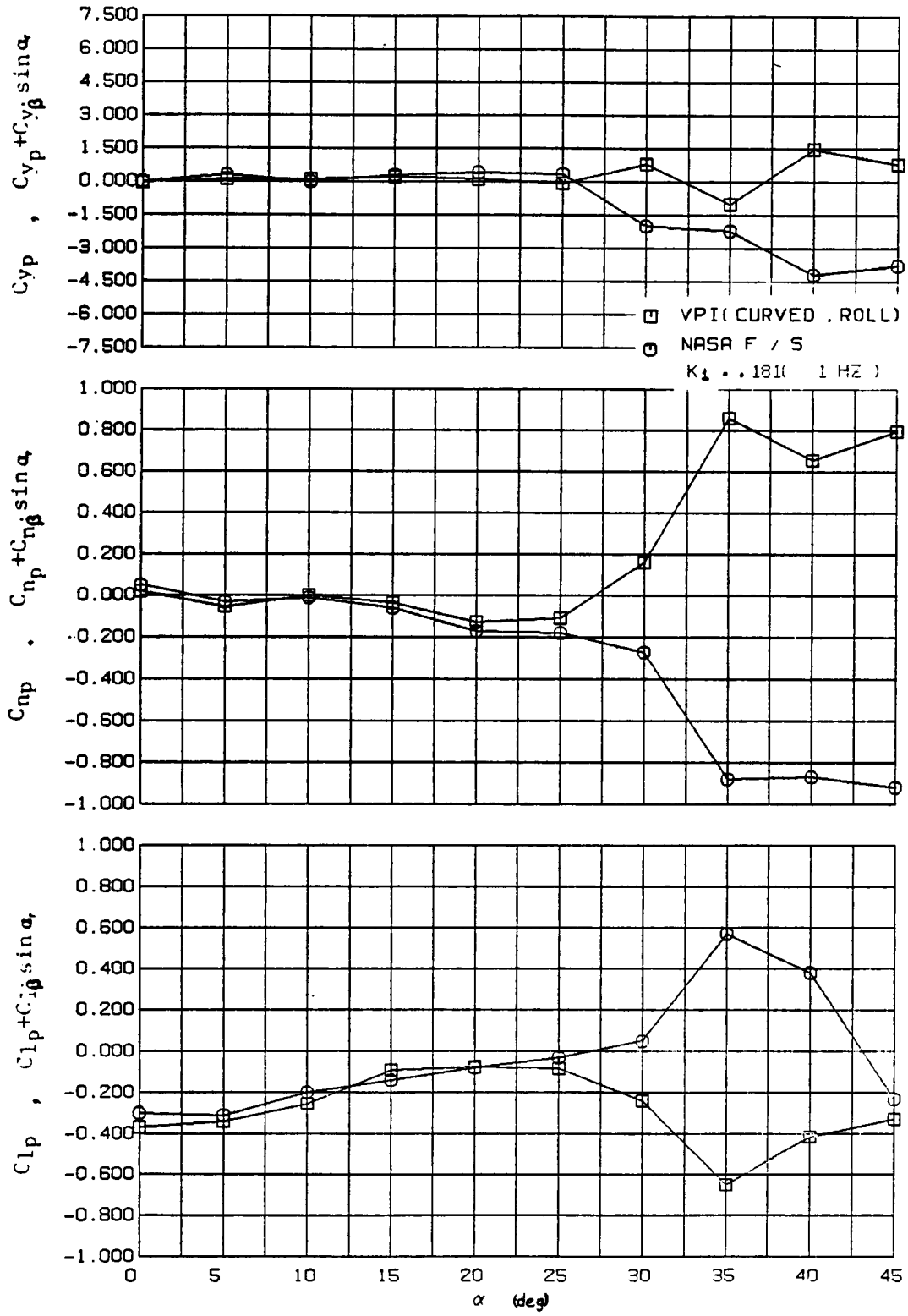

Figure 28. Comparison of Static and Out-of-Phase Derivatives from Different Tests (1).

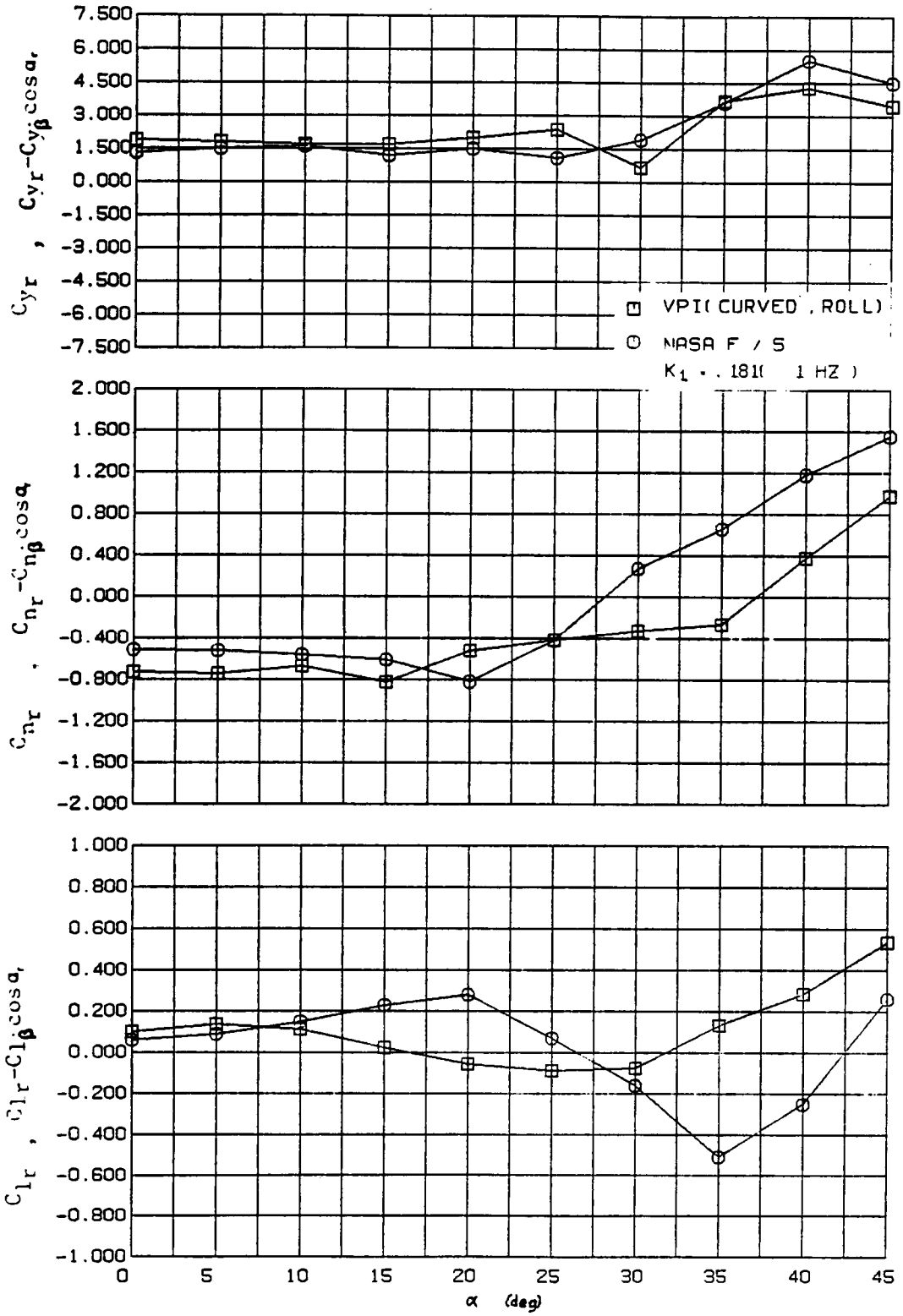

Figure 29. Comparison of Static and Out-of-Phase Derivatives from Different Tests (2).

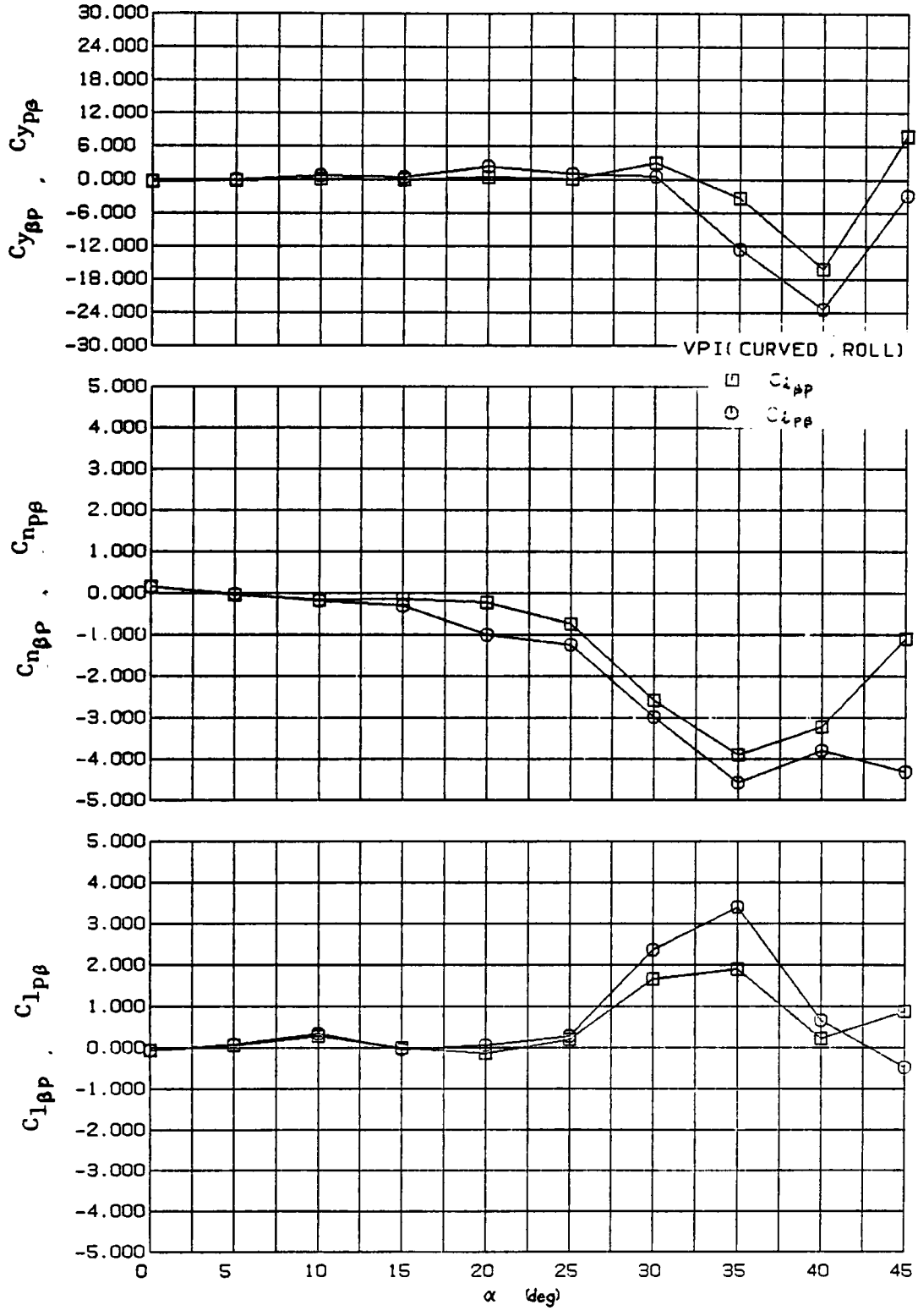

Figure 30. Comparison of Second Order Mixed Derivatives (1).

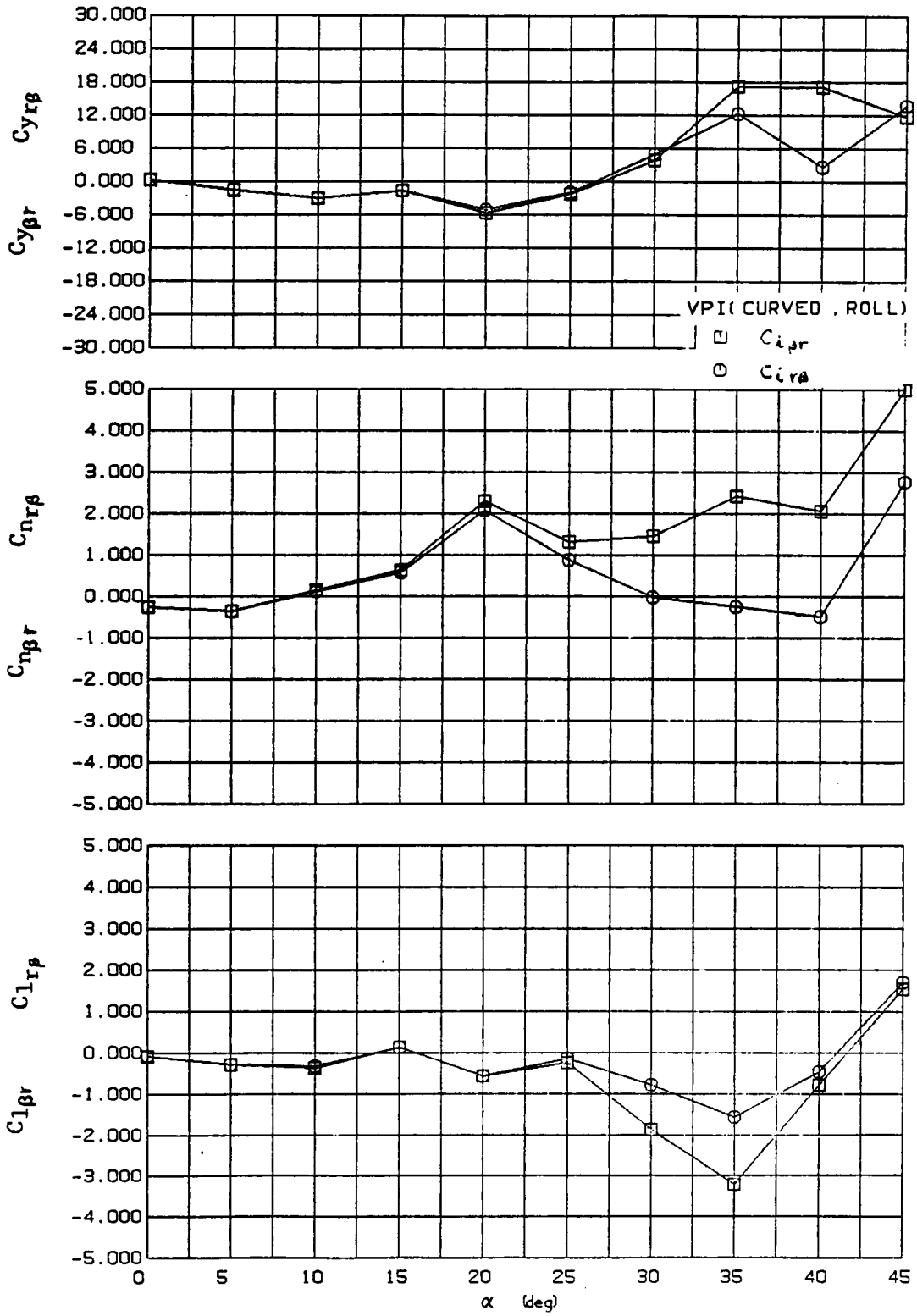

Figure 31. Comparison of Second Order Mixed Derivatives(2).

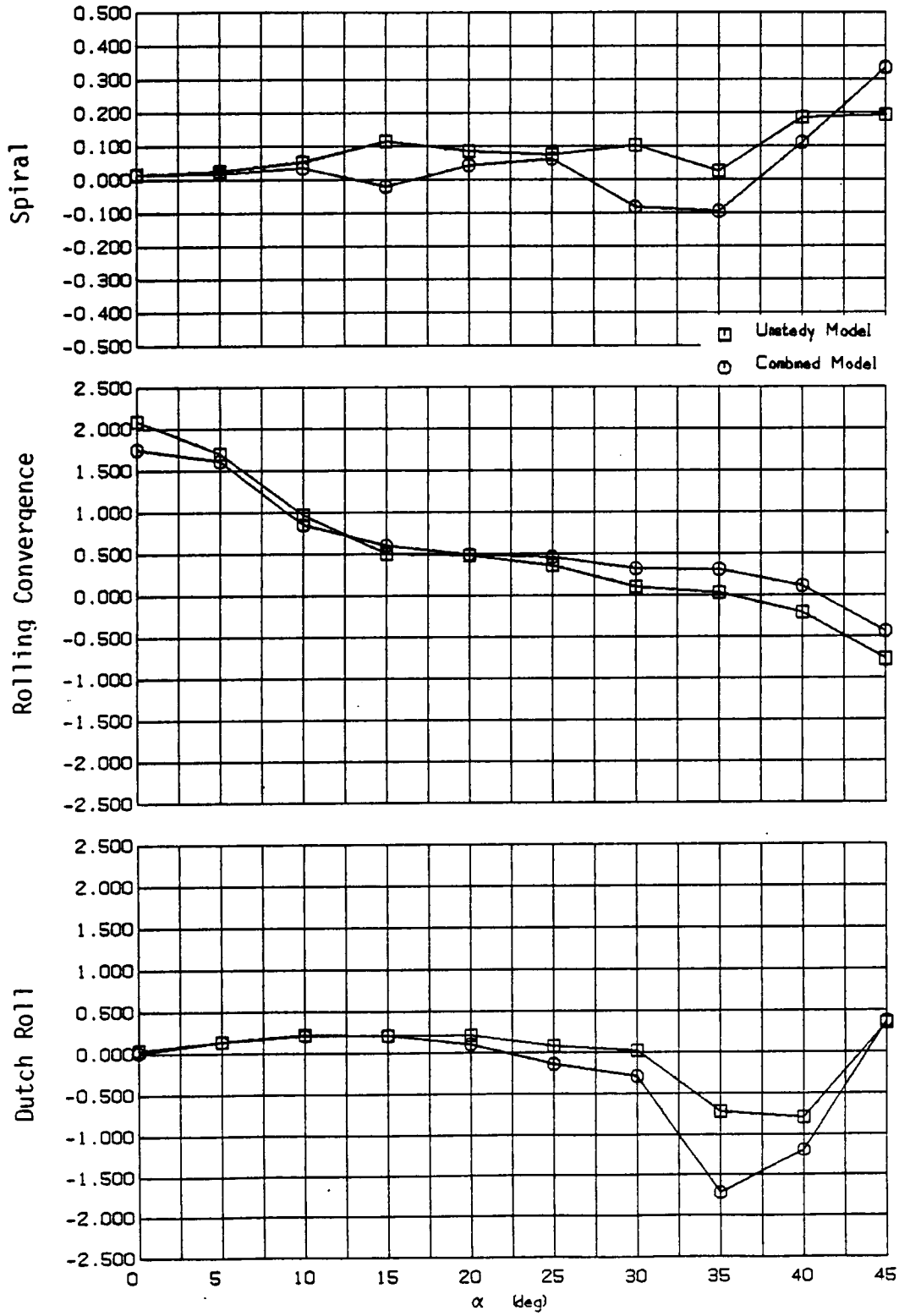

Figure 32. Comparison of Dynamic Stability Characteristics. ($1/t_{1/2}$)

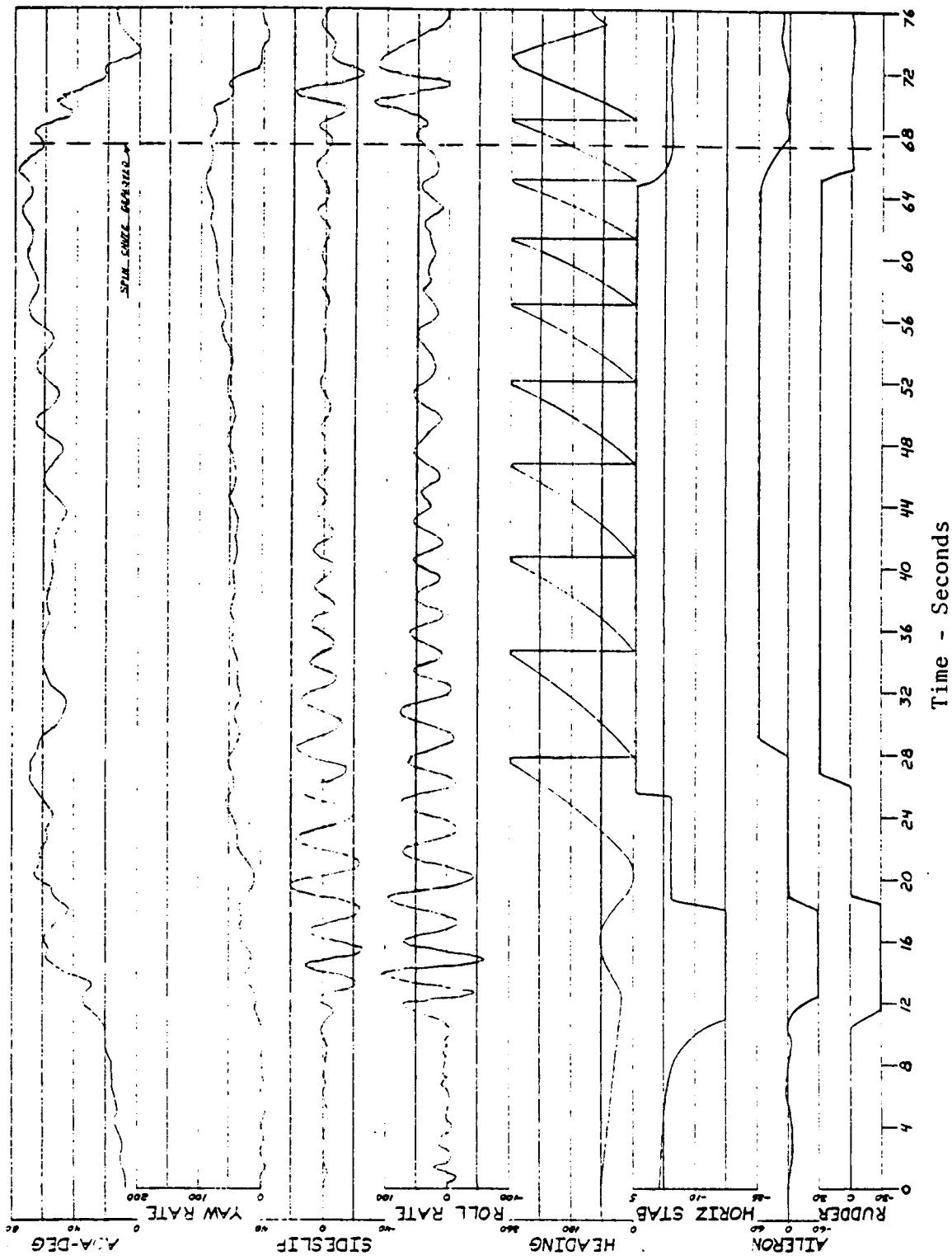

Figure 33. F-5E Spin Susceptibility Test (Erect Flat Spin).

APPENDIX

A-1 LINEAR DYNAMICAL SYSTEM

A-2 TRANSFORMATION AND NON-DIMENSIONAL MATRIX

A-3 PARAMETER SENSITIVITIES OF EIGENVALUES AND EIGENVECTORS

A-1 LINEAR DYNAMICAL SYSTEM

The linearized six general equations of motion plus the two perturbed kinematic relations without control input can be reduced to

$$[E]\,\dot{\vec{x}} = [Z]\,\vec{x} \tag{1}$$

where,

$$\vec{x} = \{\, u,\ w,\ q,\ \theta,\ V,\ p,\ r,\ \phi \,\}^T$$

$$\dot{\vec{x}} = \{\, \dot{u},\ \dot{w},\ \dot{q},\ \dot{\theta},\ \dot{V},\ \dot{p},\ \dot{r},\ \dot{\phi} \,\}^T$$

Matrix [E]

$$\begin{bmatrix}
m & 0 & 0 & 0 & -\frac{\partial X}{\partial \dot{v}} & 0 & 0 & 0 \\
0 & m-\frac{\partial Z}{\partial \dot{w}} & 0 & 0 & -\frac{\partial Z}{\partial \dot{v}} & 0 & 0 & 0 \\
0 & -\frac{\partial M}{\partial \dot{w}} & I_y & 0 & 0 & -I_{xy}-\frac{\partial M}{\partial \dot{p}} & -I_{yz}-\frac{\partial M}{\partial \dot{r}} & 0 \\
0 & 0 & 0 & 1 & 0 & 0 & 0 & 0 \\
0 & 0 & 0 & 0 & m-\frac{\partial Y}{\partial \dot{v}} & \frac{\partial Y}{\partial \dot{p}} & \frac{\partial Y}{\partial \dot{r}} & 0 \\
0 & 0 & -I_{xy}-\frac{\partial L}{\partial \dot{q}} & 0 & -\frac{\partial L}{\partial \dot{v}} & I_x-\frac{\partial L}{\partial \dot{p}} & -I_{xz}-\frac{\partial L}{\partial \dot{r}} & 0 \\
0 & 0 & -I_{yz}-\frac{\partial N}{\partial \dot{q}} & 0 & -\frac{\partial N}{\partial \dot{v}} & I_{xz}-\frac{\partial N}{\partial \dot{p}} & -I_z-\frac{\partial N}{\partial \dot{r}} & 0 \\
0 & 0 & 0 & 0 & 0 & 0 & 0 & 1
\end{bmatrix}$$

Matrix [Z]

$-mr+\frac{\partial Y}{\partial u}+\frac{\partial T}{\partial u}\sin\alpha\cos\varepsilon$	$mp+\frac{\partial Y}{\partial w}+\frac{\partial T}{\partial w}\sin\alpha\cos\varepsilon$	$\frac{\partial Y}{\partial q}$	$-mg\sin\theta\sin\phi$	$mr+\frac{\partial X}{\partial v}+\frac{\partial T}{\partial v}\cos\alpha\cos\varepsilon$	$\frac{\partial X}{\partial p}$	$mv+\frac{\partial X}{\partial r}$	0
$\frac{\partial L}{\partial u}$	$\frac{\partial L}{\partial w}$	$2I_{xz}q+L_{xz}p+(I_y-I_z)r+\frac{\partial L}{\partial q}$	0	$-mp+\frac{\partial Z}{\partial v}-\frac{\partial T}{\partial v}\sin\varepsilon$	$-mv+\frac{\partial Z}{\partial p}$	$\frac{\partial Z}{\partial r}$	$-mg\cos\theta\sin\phi$
$\frac{\partial N}{\partial u}$	$\frac{\partial N}{\partial w}$	$-2I_{xy}q-I_{xz}r+(I_z-I_y)p+\frac{\partial N}{\partial q}$	0	$\frac{\partial M}{\partial v}$	$-2I_{xz}p-I_{yz}q+(I_z-I_x)r+\frac{\partial M}{\partial p}$	$2I_{xz}r+I_{yz}q+(I_z-I_x)p+\frac{\partial M}{\partial r}$	0
0	0	$\sin\phi\tan\theta$	$\frac{q\sin\phi+r\cos\phi}{\cos^2\theta}$	0	0	$-\sin\phi$	$-q\sin\phi-r\cos\phi$
$\frac{\partial X}{\partial u}+\frac{\partial T}{\partial u}\cos\alpha\cos\varepsilon$	$-mq+\frac{\partial X}{\partial w}+\frac{\partial T}{\partial w}\cos\alpha\cos\varepsilon$	$-mw+\frac{\partial X}{\partial q}$	$-mg\cos\theta$	$\frac{\partial Y}{\partial v}+\frac{\partial T}{\partial v}\sin\alpha\cos\varepsilon$	$mw+\frac{\partial Y}{\partial p}$	$-mu+\frac{\partial Y}{\partial r}$	$mg\cos\theta\cos\phi$
$mq+\frac{\partial Z}{\partial u}-\frac{\partial T}{\partial u}\sin\varepsilon$	$\frac{\partial Z}{\partial w}-\frac{\partial T}{\partial w}\sin\varepsilon$	$mu+\frac{\partial Z}{\partial q}$	$-mg\sin\theta\cos\phi$	$\frac{\partial L}{\partial v}$	$I_{xz}q-I_{yz}r+\frac{\partial L}{\partial p}$	$-2I_{yz}r-I_{yz}p-(I_y-I_z)q+\frac{\partial L}{\partial r}$	0
$\frac{\partial M}{\partial u}$	$\frac{\partial M}{\partial w}$	$-I_{xz}p+I_{yz}r+\frac{\partial M}{\partial q}$	0	$\frac{\partial N}{\partial v}$	$2I_{xy}p+I_{yz}r+(I_x-I_y)q+\frac{\partial N}{\partial p}$	$I_{yz}p-I_{xz}q+\frac{\partial N}{\partial r}$	0
0	0	$\cos\phi$	0	0	1	$\cos\phi\tan\theta$	$\tan\theta(q\cos\phi-r\sin\phi)$

A-2 TRANSFORMATION AND NON-DIMENSIONAL MATRIX

The body axes system in Equation (1) can be converted to the conventional system with state variables $\vec{x}_1 = \{ V, \alpha, q, \theta, \beta, p, r, \phi \}^T$ such that

$$[T][E][T]^{-1} \dot{\vec{x}}_1 = [T][Z][T]^{-1} \vec{x}_1 \qquad (2.1)$$

or,

$$[E]_1 \dot{\vec{x}}_1 = [A]_1 \vec{x}_1 \qquad (2.2)$$

where,

Matrix [T]

$\frac{u}{v}$	$\frac{w}{v}$	0	0	$\frac{v}{v}$	0	0	0
$-\frac{\sin\alpha\cos\alpha}{u}$	$\frac{\cos^2\alpha}{u}$	0	1	0	0	0	0
0	0	1	0	0	0	0	0
0	0	0	1	0	0	0	0
$\frac{-u\tan\beta-w\tan\beta}{v^2}$	0	0	0	$\frac{\cos\beta}{v}$	0	0	0
0	0	0	0	0	1	0	0
0	0	0	0	0	0	1	0
0	0	0	0	0	0	0	1

Matrix $[T]^{-1} / V^2\cos\alpha$

$$
\begin{bmatrix}
\frac{\cos^2\alpha\cos\beta}{uV} & -\frac{w\cos\beta}{V^2} - \frac{vw\tan\beta}{V^3} & 0 & \frac{w\cos\beta}{V^4} + \frac{vw\tan\beta}{V^5} & -\frac{v\cos^2\alpha}{uV} & 0 & 0 & 0 \\
\frac{\sin\alpha\cos\alpha\cos\beta}{uV} & \frac{u\cos\beta}{V^2} + \frac{uv\tan\beta}{V^3} & 0 & -\frac{u\cos\beta}{V^3} - \frac{uv\tan\beta}{V^5} & -\frac{v\sin\alpha\cos\alpha}{uV} & 0 & 0 & 0 \\
0 & 0 & \frac{1}{V^2\cos\beta} & 0 & 0 & 0 & 0 & 0 \\
0 & 0 & 0 & \frac{1}{V^2\cos\beta} & 0 & 0 & 0 & 0 \\
\frac{w\sin\alpha\cos\alpha\tan\beta}{uV^3} + \frac{\cos^2\alpha\tan\beta}{V^4} & 0 & 0 & 0 & \frac{\cos\alpha\cos\beta}{V} + \frac{w\sin\alpha\cos\alpha}{uV} & 0 & 0 & 0 \\
0 & 0 & 0 & 0 & 0 & \frac{1}{V^2\cos\beta} & 0 & 0 \\
0 & 0 & 0 & 0 & 0 & 0 & \frac{1}{V^2\cos\beta} & 0 \\
0 & 0 & 0 & 0 & 0 & 0 & 0 & \frac{1}{V^2\cos\beta}
\end{bmatrix}
$$

The transformed system is nondimensionalized with state vector $\vec{x}_2 = \{ \hat{V}, \alpha, \hat{q}, \theta, \beta, \hat{p}, \hat{r}, \phi \}^T$ such that

$$[T]_1[E]_1[T]_1^{-1}\dot{\vec{x}}_2 = [T]_1[A]_1[T]_1^{-1}\vec{x}_2 \tag{3.1}$$

or,

$$[E]_2\dot{\vec{x}}_2 = [A]_2\vec{x}_2 \tag{3.2}$$

where,

$$[T]_1 = \text{diag}\{ 1/V, 1, c/(2V), 1, 1, b/(2V), b/(2V), 1 \}$$

$$[T]_1^{-1} = \text{diag}\{ V, 1, (2V)/c, 1, 1, (2V)/b, (2V)/b, 1 \}$$

A-3 PARAMETER SENSITIVITIES OF EIGENVALUES AND EIGENVECTORS

For a given homogeneous, linear, constant coefficient differential equation in matrix form such that

$$[E]\,\dot{\vec{a}} = [Z]\,\vec{a} \tag{1}$$

where [E] and [Z] are n×n matrices whose elements e_{ij} and z_{ij} are functions of various parameters (v, p, $\partial Y/\partial p$, $\partial Y/\partial \beta$ ... and etc.) and n-vector $\vec{a}$ represents state variables with which we are concerned.

Let,

$$\vec{a} = \vec{x}\, e^{\lambda t} \tag{2}$$

then

$$[Z]\,\vec{x} = \lambda\,[E]\,\vec{x} \tag{3}$$

similarly,

$$[Z]^T\vec{y} = \lambda^T[E]\,\vec{y} \tag{4}$$

where, λ is an eigenvalue and $\vec{x}$ is corresponding "right" eigenvector and $\vec{y}$ is "left" eigenvector.

Premultiplying Equation (3) by $\vec{y}_j^T$ and Equation (4) by $\vec{x}_i^T$ leads to

$$\vec{y}_j^T[Z]\,\vec{x}_i = \lambda\,\vec{y}_j^T[E]\,\vec{x}_i \tag{5}$$

$$\vec{x}_i^T [Z]^T \vec{y}_j = \lambda_j^T \vec{x}_i^T [E]^T \vec{y}_j \tag{6}$$

Transpose of Equation (6) gives

$$\vec{y}_j^T [Z] \vec{x}_i = \lambda_j \vec{y}_j^T [E] \vec{x}_i \tag{7}$$

Subtract Equation (6) from (5) gives

$$(\lambda_i - \lambda_j) \vec{y}_j^T [E] \vec{x}_i = 0 \tag{8}$$

For distinct eigenvalues, we have orthogonality relation from Equations (7) and (8)

$$\vec{y}_j^T [E] \vec{x}_i = \vec{y}_j^T [Z] \vec{x}_i = 0 , \qquad i \neq j \tag{9}$$

Normalize $\vec{x}_i$ first then normalize $\vec{y}_j$ such that

$$\vec{y}_j^T [E] \vec{x}_i = 1 , \qquad i = j \tag{10}$$

hence,

$$[Y]^T [E] [X] = I \tag{11}$$

and,

$$[Y]^T = [X]^T \{[E][X][X]^T\}^{-1} \tag{12}$$

where [X] and [Y] are matrices whose columns are the eigenvectors $\vec{x}$ and $\vec{y}$, respectively.

Derivative of an Eigenvalue

Rewrite Equation (7) such that

$$\vec{y}_i^T(\lambda_i[E] - [Z])\,\vec{x}_i = 0 \tag{13}$$

and taking the partial derivative with respect to the parameter α gives,

$$\frac{\partial \vec{y}_i}{\partial \alpha}(\lambda_i [E] - [Z])\,\vec{x}_i + \vec{y}_i^T(\lambda_i [E] - [Z])\frac{\partial \vec{x}_i}{\partial \alpha} + \vec{y}_i^T\left(\lambda_i \frac{\partial [E]}{\partial \alpha} + \frac{\partial \lambda_i}{\partial \alpha}[E] - \frac{\partial [Z]}{\partial \alpha}\right)\vec{x}_i = 0 \tag{14}$$

From Equations (3), (4), (9) and (10), Equation (14) can be reduced as follows.

$$\frac{\partial \lambda_i}{\partial \alpha} = \vec{y}_i^T\left(-\lambda_i \frac{\partial [E]}{\partial \alpha} + \frac{\partial [Z]}{\partial \alpha}\right)\vec{x}_i = 0 \tag{15}$$

Derivative of an Eigenvector

Beginning with Equation (3) and taking the partial derivative with respect to the parameter α gives

$$\left(\frac{\partial \lambda_i}{\partial \alpha} [E] + \lambda_i \frac{\partial [E]}{\partial \alpha} - \frac{\partial [Z]}{\partial \alpha} \right) \vec{x}_i + (\lambda_i [E] - [Z]) \frac{\partial \vec{x}_i}{\partial \alpha} = 0 \quad (16)$$

The derivative of an eigenvector may be written by a combination of the eigenvectors

$$\frac{\partial \vec{x}_i}{\partial \alpha} = k_{i1}\vec{x}_1 + k_{i2}\vec{x}_2 + \ldots\ldots\ldots k_{in}\vec{x}_n = \sum_{j=1}^{n} k_{ij}\, \vec{x}_j \quad (17)$$

where, k_{ij} are constants which can be determined.

Substituting Equation (17) into Equation (16) and premultiplying by $\vec{y}_1^T$ gives

$$\vec{y}_1^T \left(\frac{\partial \lambda_i}{\partial \alpha} [E] + \lambda_i \frac{\partial [E]}{\partial \alpha} - \frac{\partial [Z]}{\partial \alpha} \right) \vec{x}_i + \vec{y}_j^T (\lambda_i [E] - [Z]) \sum_{j=1}^{n} k_{ij} \vec{x}_j = 0 \quad (18)$$

Using Equations (9), (10) and (16) when j=1 leads to

$$\frac{\partial \lambda_i}{\partial \alpha} \delta_{ij} + \vec{y}_j^T \left(\lambda_i \frac{\partial [E]}{\partial \alpha} - \frac{\partial [Z]}{\partial \alpha} \right) \vec{x}_i + \vec{y}_j (\lambda_i [E] - \lambda_j [Z]) \sum_{j=1}^{n} k_{ij} \vec{x}_j = 0 \quad (19.1)$$

or,

$$\frac{\partial\lambda_i}{\partial\alpha}\,\delta_{ij} + \vec{y}_j^T\left(\lambda_i\frac{\partial[E]}{\partial\alpha} - \frac{\partial[Z]}{\partial\alpha}\right)\vec{x}_i + k_{ij}(\lambda_i - \lambda_j) = 0 \tag{19.2}$$

where, δ_{ij} is the kronecker delta.

For $i \neq j$, Equation (19) can be written

$$k_{ij} = -\frac{1}{(\lambda_i-\lambda_j)}\,\vec{y}_j^T\left(\lambda_i\frac{\partial[E]}{\partial\alpha} - \frac{\partial[Z]}{\partial\alpha}\right)\vec{x}_i \tag{20}$$

Let m denote the subscript of the element of $\vec{x}_i$ which has the largest modulus and which was normalized to 1 such that

$$x_i^m = 1 \tag{21.1}$$

$$\frac{\partial x_i^k}{\partial\alpha} = \sum_{j=1}^{n} k_{ij}\, x_j^m = 0 \tag{21.2}$$

then,

$$k_{ii} = -\sum_{\substack{j=1\\ j\neq i}}^{n} k_{ij}\, x_i^m \tag{22}$$

From Equations (17), (20), (21) and (22), we have the expression for the derivative of an eigenvector,

$$\frac{\partial \vec{x}_i}{\partial \alpha} = \sum_{\substack{j=1 \\ j \neq i}}^{n} \frac{1}{(\lambda_i - \lambda_j)} \vec{y}_j^T \left(\lambda_i \frac{\partial [E]}{\partial \alpha} - \frac{\partial [Z]}{\partial \alpha}\right) \vec{x}_i (\vec{x}_j - x_j^k \vec{x}_i) \qquad (23)$$

The vita has been removed from the scanned document